

Time-Resolved Structural Studies of the Low-Index Faces of Lead

by

John William Herman

Submitted in Partial Fulfillment
of the
Requirements for the Degree
Doctor of Philosophy

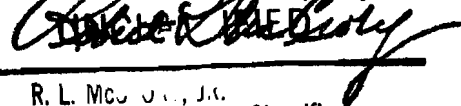
Faculty Advisor:
Professor Yongli Gao
Department of Physics and Astronomy
College of Arts and Science

Supervised by
Dr. Hani E. Elsayed-Ali
Laboratory for Laser Energetics
College of Engineering and Applied Science

University of Rochester
Rochester, NY

Reviewed for Classification 10/8/93

(Date)



1993

R. L. McCull, Jr.
Authorized Derivative Classifier

CURRICULUM VITAE

John W. Herman was born in Johnson City, NY on February 24, 1965. He attended State University of New York at Binghamton from 1983 to 1987, and graduated with a Bachelor of Science degree in Physics in 1987. Upon graduation he was the recipient of the George E. Moore Award for Academic Achievement in Physics and was inducted into Phi Beta Kappa. In September 1987 he began graduate study at the University of Rochester. From 1987 to 1988 he was a graduate teaching assistant. In 1989 he received the Master of Arts degree in Physics. In 1988 he began research at the Laboratory for Laser Energetics (LLE) on the time-resolved structure of metal surfaces. From 1990-1993 he was supported by an LLE Fellowship. His work was supervised by Professor Hani E. Elsayed-Ali. His faculty advisor was Professor Yongli Gao.

ACKNOWLEDGMENTS

It is a pleasure to thank my supervisor, Professor Hani Elsayed-Ali, for his guidance and support. He provided a very stimulating research atmosphere throughout my time at the Laboratory for Laser Energetics (LLE). In addition, I would like to thank Dr. William Donaldson and the other members of the Ultrafast Sciences Division at LLE, as well as Professor Edward Jacobsen, for many instances of helpful advice and encouragement. My faculty advisor, Professor Yongli Gao, has provided much guidance for which I am grateful. The help and friendship of Elizabeth Murphy, my coworker at LLE, has enhanced my graduate research career. Betty Cook has been a cheerful guide through the administrative details throughout my time at the University. My friends and fellow classmates provided a very enjoyable and supportive environment throughout my time here. I gratefully acknowledge the support of an LLE Fellowship which I received from 6/89 - 6/93. Finally, I wish to thank my family and my wife, Runa, for their patience, encouragement and love.

This work was supported by the US Department of Energy under Contract No. DE-FG02-88ER45376 and by the United States Air Force Office of Scientific Research under Contract No. AFOSR-87-0327. Additional support was provided by the Laser Fusion Feasibility Project at LLE, which is sponsored by the New York State Energy Research and Development Authority and the University of Rochester.

ABSTRACT

Time-resolved reflection high-energy electron diffraction has been developed to study the structure of surfaces. In this technique, an ultrafast laser pulse is split into two components. The first component interacts with the surface and serves as a transient heating source. The second component strikes the cathode of a photoactivated electron gun, photoelectrically producing pulses of electrons. The electron pulses are accelerated to energies on the order of 15 keV and are incident at a glancing angle to the studied surface, probing the first few atomic layers. The heating laser pulse passes through an optical delay line which provides the means by which the heating pulse and electron probe pulse are temporally synchronized on the surface. Analysis of the resulting time-resolved diffraction patterns provides information about the temperature and structure of the probed layer.

The technique of time-resolved reflection high-energy electron diffraction, with 200-ps resolution, is used to study the structural behavior of the low-index faces of Pb. The surfaces are subjected to heating and cooling rates on the order of 10^{11} K/s. A pronounced orientation-dependence of the structural dynamics is observed. The open Pb(110) surface is seen to reversibly disorder below the bulk melting temperature, $T_m = 600.7$ K. In contrast to Pb(110), the close-packed Pb(111) surface sustains superheating to $T_m + 120$ K. Pb(100), a surface with atomic packing intermediate to that of Pb(110) and Pb(111), shows evidence of residual order at temperatures above the bulk melting point.

Table of Contents

Chapter 1	Introduction	1
Chapter 2	Experimental and Theoretical Survey of Surface Melting	9
	2.1 Experimental Results	9
	2.2 Mean-Field Theory Treatment	15
	2.3 Molecular Dynamics Simulation	22
Chapter 3	Time-Resolved Reflection High-Energy Electron Diffraction (RHEED)	35
	3.1 Conventional RHEED	35
	3.2 Time-Resolved RHEED: Experimental Technique	47
	3.3 Time-Resolved RHEED as a Surface-Lattice Temperature Probe	52
Chapter 4	Time-Resolved Surface Disordering of Pb(110)	72
Chapter 5	Superheating of Pb(111)	84
Chapter 6	Time-Resolved Structural Study of Pb(100).....	107
Summary	116
Appendix A:	Determination of the Surface Debye Temperature Using RHEED.....	117
Appendix B:	Auger Electron Spectroscopy.....	126
Appendix C:	Regenerative Amplifier Laser System	135

List of Tables

<u>Table</u>	<u>Title</u>	<u>Page</u>
1	Adatom-vacancy formation energies, E_v , according to molecular dynamics simulation	25
2	Parameters for the time-resolved heating experiment	64
3	Maximum observed undercooling of melts of fcc metals	85
4	Parameters for the RHEED surface Debye temperature measurements	119
5	The Debye temperature for the low-index faces of Pb	124

List of Figures

<u>Figure</u>	<u>Title</u>	<u>Page</u>
1	The temperature dependence of the Gibbs free energy for melting. The discontinuity in the slope of the free energy at the melting temperature, T_m , reflects the heat of fusion and is indicative of a first-order phase transformation.	2
2	The tendency of a particular surface to form a disordered layer below T_m depends on the free energy difference between the ordered surface and the surface covered with a "quasiliquid" film.	4
3	Time-resolved reflection high-energy electron diffraction (RHEED). An ultrafast laser pulse serves as the transient heating source for the surface. An electron pulse with temporal width comparable to that of the heating laser pulse probes the first several atomic layers a fixed time relative to the arrival of the heating laser pulse. The diffraction pattern from the surface provides an ultrafast snapshot of the temperature and structure of the probed layer.	7
4	Schematic diagram of the technique of medium-energy ion scattering (MEIS). The ordered surface on the left	10

acts to shadow and block the proton beam, leading to a sharp energy peak of the back-scattered ions. A surface covered by a thin disordered layer is less effective in shadowing and blocking the proton beam and this leads to a greater back-scattered yield and a broadened energy peak. Reprinted with permission from Ref. 3 [B. Pluis, A. W. Denier van der Gon, J. F. van der Veen, and A. J. Riemersma, Surf. Sci. 239, 265 (1990)] .

- 5 MEIS data showing the number of disordered atoms per unit area versus surface orientation and temperature. Prominent disorder is seen for most crystalline orientations with the exception of the (111) and (100) faces. Reprinted with permission from Ref. 3 [B. Pluis, A. W. Denier van der Gon, J. F. van der Veen, and A. J. Riemersma, Surf. Sci. 239, 265 (1990)] . 12
- 6 Diagram of the surface packing of the three low-index faces of an fcc metal. The open (110) surface has the lowest degree of surface packing while the (111) surface is close-packed. 13
- 7 (a) Components of the free energy of the disordered layer on Pb(110) at $T/T_m = 0.99$. (b) Total free energy 19

- of disordered layer on Pb(110) at $T/T_m = 0.99$. The minimum in the free energy occurs at a disordered layer thickness of approximately 14 Å.
- 8 Free energy $F(l)$ of the disordered layer on Ge(111) at $T/T_m = 0.99$ in the layering model of Chernov and Mikheev (Ref. 23). The oscillatory character of $F(l)$ is due to the periodic density modulation in the disordered layer induced by the solid substrate. The disordered layer thickness does not diverge as T_m is approached. The minimum in the free energy occurs at $l_0 = 2\pi/k_l = 2.3$ Å. 21
- 9 Snapshots from a molecular dynamics simulation of Cu(110). The melting temperature of the model was 1240 ± 25 K. The black spheres represent surface atoms while the spheres labeled O represent adatoms. Note the increase in the number of adatoms with temperature leading to a disordered surface at $T_m - 40$ K. Reprinted with permission from Reference 37 [H. Hakkinen and M. Manninen, Phys. Rev. B **46**, 1725 (1992)]. 26
- 10 Atomic trajectory plots of the low-index faces of Cu near T_m . Cu(110) is seen to exhibit prominent disordering, while Cu(111) remains ordered. This 27

demonstrates the orientation dependence of surface melting. Reprinted with permission from Reference 37 [H. Hakkinen and M. Manninen, Phys. Rev. B 46, 1725 (1992)] .

- 11 Anharmonic and anisotropic vibrations of edge atoms on surface steps lead to the creation of adatoms. The ellipses on the surface atoms represent enhanced vibrational amplitudes. 30
- 12 Schematic diagram of reflection high-energy electron diffraction (RHEED). The electron beam is incident on the surface at an angle θ , probing the first several atomic layers. The RHEED pattern, which consists of a series of streaks that are oriented perpendicular to the plane of the surface, is detected on a phosphor screen. 36
- 13 The Ewald construction for the elastic diffraction of low energy electrons. The diameter of the sphere is $2\pi/\lambda$, where λ is the de Broglie wavelength of the incident electrons. Constructive interference occurs in directions where the Ewald sphere intersects a point of the reciprocal lattice, satisfying the Laue diffraction condition. 38
- 14 Ewald construction for the case of RHEED. The Laue condition is satisfied for the scattering vector k' . 39

- 15 Ewald construction for high energy electrons. In this case the radius of the Ewald sphere is much larger than dimensions in reciprocal space. As a consequence of this, RHEED essentially views cross-sections of reciprocal space. 41
- 16 Photograph of a RHEED pattern from Pb(111). The distance from the specular reflected beam and the shadow edge is used along with the sample-to-screen distance to determine the angle of incidence of the electron beam on the surface. 42
- 17 The inelastic mean-free-path of electrons in Pb. For an electron energy of 15 keV, typical in RHEED, the inelastic mean free path in Pb is approximately 90 Å. 44
- 18 A series of photographs of the RHEED pattern of Pb(110) taken at various azimuthal orientations. 45
- 19 Differential scattering cross section for various structural probes. X-ray scattering in solids has a low differential scattering cross section due to the weak interaction of photons with solids. The sensitivity of RHEED is comparable to that of low-energy electron diffraction (LEED) with the advantage that the scattering is significantly less isotropic. 46

- 20 Time-resolved reflection high-energy electron diffraction (RHEED). The laser heating pulse (pump) and the electron probe pulse are synchronized. An optical delay line sets the timing between the pump and the probe. 48
- 21 Schematic diagram of the photoactivated electron gun. The photocathode consists of a thin film ($\sim 200 \text{ \AA}$) of polycrystalline Au deposited on a sapphire substrate. 50
- 22 Schematic diagram of the ultrahigh vacuum chamber: (a) top view and (b) side view. 51
- 23 Auger spectrum of a Pb surface after Ar^+ sputtering. The Pb Auger peaks are labeled. The energy of the primary electron beam is 3 keV. 53
- 24 The process of laser-metal interaction. 54
- 25 RHEED streak intensity, normalized to that at 407 K, versus sample temperature for Pb(111). The orientation of the crystal was the same as that for the pulsed laser heating experiments. The solid line is an exponential fit to the data showing good agreement to the Debye-Waller attenuation of the diffraction intensity 58

with increasing temperature. These data are used to associate a given diffraction intensity with a surface temperature.

- 26 Line scans through the diffraction pattern for an unheated surface and a laser-heated surface. A shutter is placed in the path of the heating laser which allows every other heating pulse to interact with the sample. The computer sorts heated and unheated scans in separate memories and performs averages of these scans. The attenuation of the diffraction intensity due to laser heating is evident. 60
- 27 Time-resolved modulation of the RHEED streak intensity of Pb(111) subjected to ~ 200 ps (FWHM) laser pulses with peak intensity of $I_p \sim 3.0 \times 10^7$ W/cm². The diffraction intensity decreases rapidly upon the arrival of the laser pulse and subsequently increases as the surface cools by heat conduction into the bulk of the crystal. The data of Fig. 25 are used to convert the diffraction intensity modulation to a surface-temperature rise. 61
- 28 Surface-temperature rise induced on Pb(111). These data are the result of the conversion of the data of Fig. 27 to surface temperature through Fig. 25. The solid 63

line is a solution of the heat diffusion model for the parameters of the experiment.

- 29 Peak surface-temperature rise ΔT on Pb(110) subjected to various laser fluences. Experiments were carried out at the experimentally-determined peak of the surface-temperature rise, t_0 , and at $t_0 + 500$ ps. ΔT is seen to increase linearly with laser fluence in agreement to the heat diffusion model. 66
- 30 Surface-temperature rise induced on Pb(110) irradiated with $I_p \sim 3.5 \times 10^7$ W/cm², 170 ps (FWHM) laser pulses. The solid line is obtained from a heat diffusion model. The inset is an expanded view near the peak of the surface-temperature rise with the dashed line representing the temporal profile of the laser heating pulse. The effects of convolution are most prominent near the peak of the surface-temperature rise where the rate of change of temperature with time is greatest. 67
- 31 Ratio of the peak ΔT to the ΔT obtained by a temporal average about the surface-temperature peak with various electron pulse widths. These data were obtained by examining solutions to the heat diffusion model assuming laser heating pulses with width of 200 ps. For an electron pulse width comparable to the 69

laser pulse width, a 20% reduction in the observed ΔT relative to the peak ΔT is predicted.

- 32 Photographs of the RHEED pattern of Pb(110) taken at various temperatures approaching the bulk melting point. Above $T_m - 50$ K, the diffraction intensity vanishes indicating that the probed layer is disordered. 75
- 33 RHEED streak intensity from Pb(110) normalized to that at 487 K versus temperature. A curve fit is made to the data and is used with the heat diffusion model to obtain the predicted time-resolved modulation of the RHEED streak intensity in Fig. 34. Inset: The data is plotted on a semilogarithmic scale. The line fit includes data points up to that which maximizes the linear correlation coefficient. The data departs from exponential Debye-Waller behavior at $T \sim 520$ K. 76
- 34 Time-resolved RHEED streak intensity measurements on Pb(110). The pulse width of the laser is measured at full-width at half-maximum (FWHM). The corresponding surface temperature is obtained using the data of Fig. 33. (a) $I_p = 1.4 \times 10^7$ W/cm², 165 ps FWHM, (b) $I_p = 2.0 \times 10^7$ W/cm², 165 ps FWHM, (c) $I_p = 2.7 \times 10^7$ W/cm², 175 ps FWHM, (d) $I_p = 3.6$ 78

$\times 10^7 \text{ W/cm}^2$, 170 ps FWHM. In (c) and (d) the normalized streak intensity is seen to vanish for some time indicating that order is lost in the probed surface layer. The subsequent reappearance of the streak intensity indicates the reordering of the surface.

- | | | |
|----|--|----|
| 35 | Free energy of a spherical supercooled droplet versus radius. Plots are given for varying amounts of supercooling. | 86 |
| 36 | Critical radius for homogeneous nucleation of the supercooled liquid into a solid. The critical radius decreases with increasing supercooling. | 88 |
| 37 | Photographs of the RHEED pattern of Pb(111), a surface which does not exhibit surface melting. The RHEED pattern is clearly visible up to $T_m - 15 \text{ K}$. | 92 |
| 38 | RHEED streak intensity of Pb(111), normalized to that at 407 K, versus sample temperature. An exponential curve fit has been made to the data. Inset: The data plotted on a semilogarithmic scale showing Debye-Waller behavior up to $T_m - 15 \text{ K}$. | 93 |
| 39 | (a) Modulation of the normalized RHEED streak intensity for $I_p \sim 3.3 \times 10^7 \text{ W/cm}^2$ and varying sample | 94 |

bias temperatures, T_{bias} , performed at the time t_0 . (b) The streak intensity of (a) is converted to a peak surface-temperature rise, ΔT , using the data of Fig. 38. In addition, results from the heat diffusion model are plotted. The higher ΔT predicted by the model is most likely due to convolution effects which are most prominent at t_0 . For $T_{\text{bias}} \geq 530$ K, the peak surface temperature exceeds T_m .

- 40 Surface-temperature rise versus T_{bias} for $I_p \sim 3.3 \times 10^7$ W/cm² performed at t_0 and subsequent delay times. The general trend of increasing ΔT with T_{bias} is attributed to the change in optical and thermal properties of the sample in the considered temperature range. 96
- 41 RHEED streak intensity normalized to that at 586 K versus peak laser intensity, I_p . This data set was obtained at the time corresponding to the temporal minimum of the normalized streak intensity, t_0 . Inset: A plot of the data on a semilogarithmic scale showing deviation from Debye-Waller behavior at $I_p \sim 3.5 \times 10^7$ W/cm². The corresponding peak surface temperature is $\sim T_m + 120$ K. 97

- 42 RHEED streak intensity normalized to that at 586 K versus peak laser intensity, I_p . These sets were performed at times of $t_0 + 500$ ps and $t_0 + 4000$ ps. The insets are plotted on a semilogarithmic scale and show the break from Debye-Waller behavior at $I_p \sim 3-4 \times 10^7$ W/cm², consistent with what was observed at the time t_0 . 99
- 43 RHEED streak intensity normalized to that at 586 K versus peak laser intensity, I_p , for an electron beam angle of incidence of $\sim 1^\circ$ at the times t_0 and $t_0 + 4000$ -ps. Insets show the departure from Debye-Waller behavior at $I_p \sim 3-4 \times 10^7$ W/cm². 101
- 44 Time-resolved normalized RHEED streak intensity of Pb(111) irradiated with laser pulses of varying peak intensity. Set (a) is consistent with classical heat diffusion and corresponds to a peak surface temperature of $T_m + 110$ K. In sets (b)-(d), where $I_p \geq 3.5 \times 10^7$ W/cm², the surface begins to melt as is evident in the pronounced deviation from classical heat diffusion. 102
- 45 The time interval, τ , from t_0 to the time at which deviation from classical heat diffusion occurs, is 104

extracted from data sets as in Figs. 44b-c. The time τ is seen to decrease with increasing peak laser intensity.

- 46 RHEED streak intensity from Pb(100) normalized to that at 377 K versus temperature. The inset shows the data plotted on a semilogarithmic scale. The solid lines are polynomial fits to the data. The streak intensity is observed to deviate from Debye-Waller behavior for $T \geq 450$ K. 108
- 47 RHEED streak intensity versus peak laser intensity, I_p , on Pb(100) at the time t_0 . The sample was biased at 450 K. Inset: Peak surface-temperature rise, ΔT , versus I_p . The inset is a result of the conversion of the streak intensity modulation to a ΔT using the data of Fig. 46. This data is used to determine ΔT for data sets where T_{bias} is closer to T_m . 110
- 48 Normalized RHEED streak intensity versus peak laser intensity for bias temperatures successively closer to T_m . The streak intensity vanishes for I_p above a certain threshold which depends on T_{bias} . This threshold is used along with the data of Fig. 47 to determine the temperature at which order is lost in the probed layer. 111

- 49 Time-resolved normalized RHEED streak intensity on Pb(100) at different bias temperatures, T_{bias} , subjected to varying peak laser intensities, I_p . (a) $T_{\text{bias}} = 321$ K, $I_p = 4.4 \times 10^7$ W/cm². (b) $T_{\text{bias}} = 570$ K, $I_p = 2.3 \times 10^7$ W/cm². (c) $T_{\text{bias}} = 570$ K, $I_p = 3.4 \times 10^7$ W/cm². (d) $T_{\text{bias}} = 570$ K, $I_p = 5.1 \times 10^7$ W/cm². 113
- 50 Scattering geometry in the RHEED intensity measurements. The wavevector \bar{k}_0 corresponds to the incident electron beam, while \bar{k}'_0 and \bar{k}'_1 correspond to the specular and first-order peaks, respectively. $\Delta\bar{k}'_0$ and $\Delta\bar{k}'_1$ represent the momentum transfers to the specular and first-order diffraction peaks, respectively. (Courtesy of E. A. Murphy) 120
- 51 Logarithm of the normalized intensity of the (10) streak of Pb(111). The diffraction intensity decays according to the Debye-Waller effect. Also displayed in the plot is the predicted behavior of the streak intensity, assuming that the surface has a Debye temperature identical to that of the bulk. 122
- 52 Secondary electron spectrum. 127

53	The Auger effect.	128
54	Cross-sectional view of the cylindrical mirror analyzer.	130
55	Experimental configuration of the cylindrical mirror analyzer system. (From Omicron Vakuumphysik, Instruction manual for the CMA150.)	132
56	Auger spectrum of a contaminated Pb surface taken with a primary beam energy of 3 keV. Carbon and oxygen Auger peaks are clearly visible.	133
57	Schematic diagram of the regenerative amplifier laser system.	136
58	Build-up of the energy of the injected pulse in the regenerative amplifier cavity. The pulse is ejected from the cavity when the peak energy is reached	137

LIST OF ACRONYMS

AES	Auger electron spectroscopy
CMA	Cylindrical mirror analyzer
CW	Continuous wave
fcc	Face-centered cubic
FWHM	Full-width at half-maximum
LEED	Low-energy electron diffraction
MCP	Microchannel plate
MD	Molecular dynamics
MEIS	Medium-energy ion scattering
RHEED	Reflection high-energy electron diffraction
SHG	Second-harmonic generation
UHV	Ultrahigh vacuum
XPD	X-ray photoelectron diffraction
YAG	Yttrium aluminum garnet

CHAPTER 1: INTRODUCTION

Although the phenomenon of melting has been studied extensively for many years, a complete understanding of the process remains elusive. From a thermodynamic standpoint, the melting temperature, T_m , is defined to be the temperature at which the solid and liquid phases coexist in equilibrium. This occurs when the Gibbs free energy of the phases is equal. Furthermore, bulk melting is a first order phase transformation, distinguished by a discontinuous change in the entropy at T_m , leading to a latent heat (Fig. 1). Melting is also accompanied by abrupt changes in other material properties such as density, specific heat, electrical and thermal conductivity, elastic properties, and self-diffusion coefficient.¹ In spite of the differences between the two phases, they are alike in that they are both condensed phases. The challenge that has been facing physicists for many years is explaining how the transformation between these phases is initiated.

Two main viewpoints have been proposed to describe the process of melting.^{1,2} The first states that the melting transition is abrupt, requiring no process of nucleation and growth. According to this view, melting occurs homogeneously and rapidly, on a time scale comparable to the period of an atomic vibration. This behavior has not been experimentally observed and the second viewpoint of melting is generally accepted, which holds that melting is initiated through a nucleation and growth process. Melting is thought to be initiated at (i) internal surfaces, which consist of crystalline defects such as dislocations, voids, and grain boundaries, and (ii) free surfaces. Much experimental evidence has been amassed to support the nucleation and growth view.

The idea that melting is initiated at the surface of solids has intrigued researchers for many years. In the mid 1800's, Faraday performed experiments on ice in which he inferred the existence of a liquid film that forms in equilibrium on the surface.³

Gibbs Free Energy versus Temperature

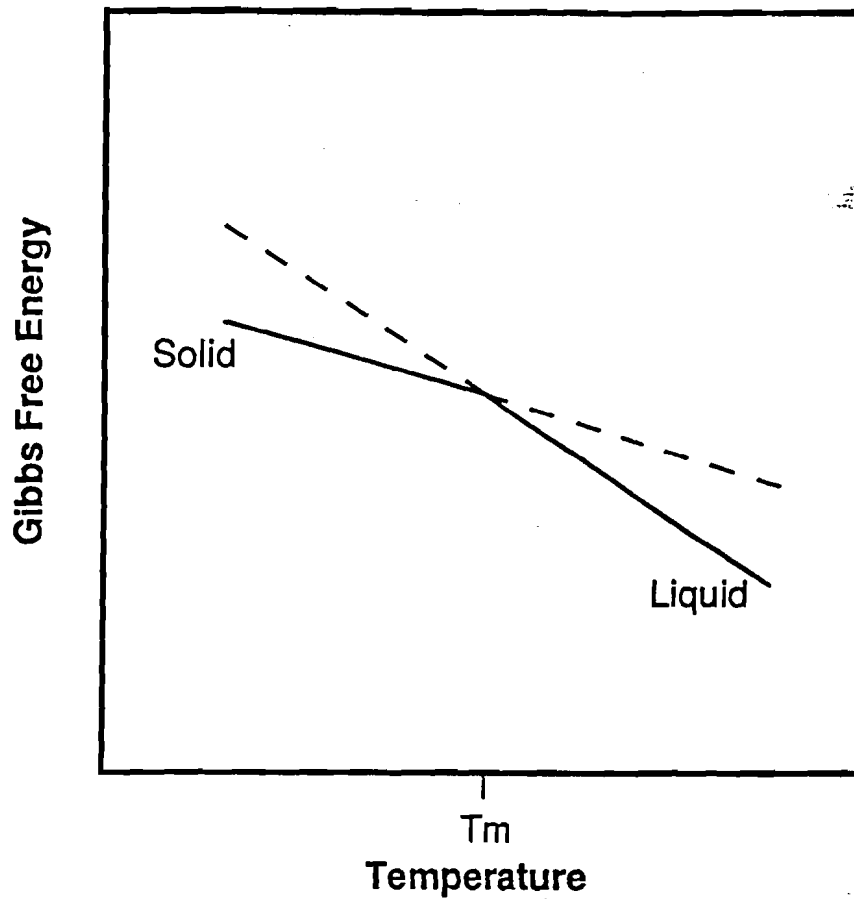


Figure 1. The temperature dependence of the Gibbs free energy for melting. The discontinuity in the slope of the free energy at the melting temperature, T_m , reflects the heat of fusion and is indicative of a first-order phase transformation.

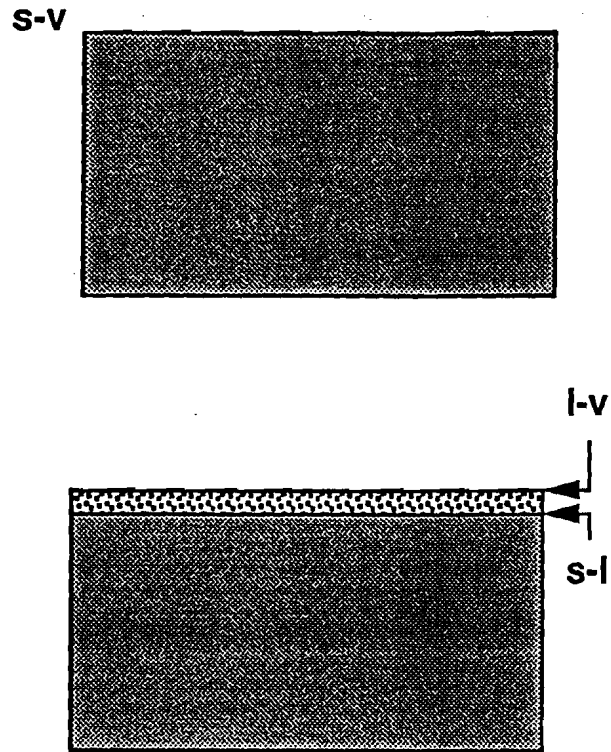
Faraday's notion that the surface of ice melts below the bulk melting temperature was not generally accepted at the time. However, subsequent work by Tammann⁴ and a reexamination of the phenomenon by Weyl⁵ reinvigorated investigations into surface-initiated melting, which is the formation of a thin, disordered "quasiliquid" layer on the surface of an otherwise ordered solid at temperatures *below* T_m . Faraday's assertion that a liquid layer is present on crystals of ice was confirmed many years later with modern surface science techniques.⁶ Since Faraday's initial work, much effort has gone into determining if surface melting is a general phenomenon.

Surface melting is frequently discussed in the context of a well known relation between the interfacial free energies of a dry surface and a surface covered with a disordered layer:²

$$\gamma_{sv} > \gamma_{sl} + \gamma_{lv}.$$

In this expression, γ_{sv} , γ_{sl} , and γ_{lv} are the interfacial free energies of the solid-vapor, solid-liquid, and liquid-vapor interfaces, respectively. A schematic drawing of a solid with a disordered surface film is given in Fig. 2. The above expression, which is valid for many surfaces above a certain temperature, implies that it is energetically favorable for the surface to form a thin, disordered film between the ordered solid and the vapor.

Many of the initial experiments on surface melting provided qualitative evidence for the existence of a disordered surface layer below T_m . In one of the first such studies, Stock examined the optical emissivity of Cu spheres near T_m .⁷ He observed that molten regions of the sphere had significantly greater emission than solid regions. The regions of low emissivity had values consistent with a solid phase and occurred at areas of the sphere where the crystalline packing density was largest. Conversely, the areas of the sphere with a lower degree of surface packing



$$\gamma_{sv} > \gamma_{sl} + \gamma_{lv}$$

Figure 2. The tendency of a particular surface to form a disordered layer below T_m depends on the free energy difference between the ordered surface and the surface covered with a "quasiliquid" film.

demonstrated high emissivity consistent with the liquid phase. This experiment provided the first connection between surface orientation and the tendency of a face to disorder below T_m .

The advent of modern surface science techniques insured that atomically clean single crystal surfaces could be prepared for quantitative studies of surface-initiated melting. A wide variety of methods have been used to study surface melting.⁸ Some of the techniques include low-energy electron diffraction (LEED), x-ray photoelectron diffraction (XPD), UV photoelectron spectroscopy, quasi-elastic atom scattering, calorimetry, ellipsometry, and neutron scattering. Surface melting appears to be a quite general phenomenon which has been observed to occur on many solids including metals, ice, and molecular crystals. The experiments characterize surface melting as a reversible process with the disordered layer thickness increasing with temperature and eventually diverging at T_m .

The surface melting of metals would provide an explanation for a long-standing problem in solid-state physics, namely the lack of parity between supercooling and superheating.² The supercooling of melts of metals has been observed for many years, while the superheating of metals has been rarely observed. The formation of a thin liquid-like layer on a metal surface at a temperature below T_m provides an ideal nucleation site for melting into the bulk as T_m is approached. This explains the difficulty of superheating metals.

All of the previous work examining surface melting has focussed on the determination of equilibrium properties such as the temperature at which the process begins or the number of disordered layers that exist on a given crystal surface at a given temperature. The work presented in this thesis examines surface melting from another perspective. It focuses on the time evolution of the process and how crystalline orientation influences the time-resolved dynamics of the disordering process. To

accomplish this we have developed time-resolved reflection high-energy electron diffraction, a novel pump-probe experiment where a short pulse of electrons interacts with the studied surface a set time after the arrival of a heating laser pulse.⁹ This is illustrated in Fig. 3. From a careful analysis of the diffracted electrons, we are able to observe the effects of fast transient events that take place at surfaces such as surface heating and melting.

The sample chosen for these studies was Pb. Pb was chosen for several reasons. Firstly, the vapor pressure of Pb at $T_m = 600.7$ K is very low ($\sim 5 \times 10^{-9}$ Torr), so melting under ultrahigh vacuum (UHV) conditions will proceed in a similar manner to melting in equilibrium with the vapor. Secondly, Pb has a relatively high absorption coefficient in the near-infrared portion of the spectrum allowing effective heating of the surface with the $\lambda = 1.06$ μm laser utilized in this work. Finally, the surface melting of Pb faces has been studied extensively using equilibrium surface science techniques and represents a prototypical system for the surface melting of metals.

The thesis is organized as follows. Chapter 2 will briefly survey the experimental and theoretical work on surface melting. In Chapter 3, the techniques of conventional and time-resolved reflection high-energy electron diffraction (RHEED) are described. In this chapter, the application of time-resolved RHEED as an ultrafast temperature probe is demonstrated. This establishes the viability of the technique as a probe of ultrafast processes at surfaces. Chapters 4-6 present the studies of the time-resolved structural behavior of the low-index faces of Pb. The results are discussed in the Summary. In addition, three appendices are included that describe (i) the determination of the surface Debye temperature, (ii) the technique of Auger electron spectroscopy, and (iii) the regenerative amplifier laser system used in the work.

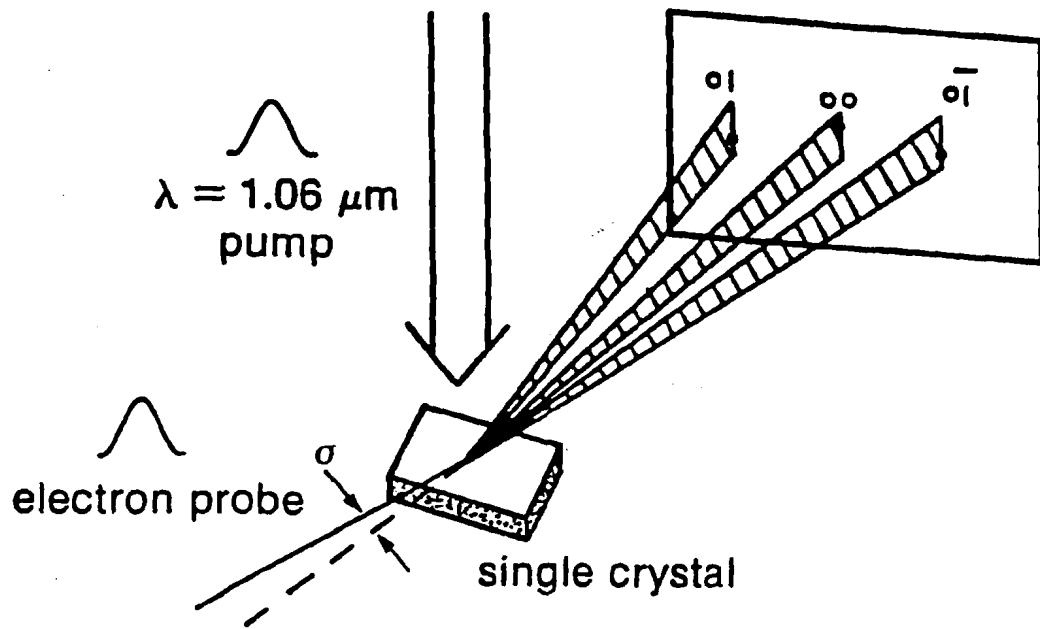


Figure 3. Time-resolved reflection high-energy electron diffraction (RHEED). An ultrafast laser pulse serves as the transient heating source for the surface. An electron pulse with temporal width comparable to that of the heating laser pulse probes the first several atomic layers a fixed time relative to the arrival of the heating laser pulse. The diffraction pattern from the surface provides an ultrafast snapshot of the temperature and structure of the probed layer.

REFERENCES

1. A. R. Ubbelohde, *The Molten State of Matter* (Wiley, New York, 1978).
2. D. P. Woodruff, *The Solid-Liquid Interface* (Cambridge University Press, Cambridge, 1973).
3. M. Faraday, Proc. R. Soc. London **10**, 440 (1860).
4. G. Tammann, Z. Phys. Chem. **72**, 609 (1910).
5. W. A. Weyl, J. Colloid Sci. **6**, 389 (1951).
6. See, for example, Y. Furukawa, M. Yamamoto, and T. Kuroda, J. Cryst. Growth **82**, 665 (1987).
7. K. D. Stock, Surf. Sci. **91**, 655 (1980).
8. See J. G. Dash, Contemporary Physics **30**, 89 (1989) for a review of surface melting and the techniques used to study it.
9. H. E. Elsayed-Ali and J. W. Herman, Rev. Sci. Instrum. **61**, 1636 (1990).

CHAPTER 2: EXPERIMENTAL AND THEORETICAL SURVEY OF SURFACE MELTING

2.1 EXPERIMENTAL RESULTS

Much of the early quantitative work on surface melting of metals was performed on Pb. One of the first conclusive experimental observations of surface melting was made on Pb(110) using medium-energy ion scattering (MEIS).¹ A diagram of the technique of MEIS is shown in Fig. 4. A 100 keV beam of protons is incident on a single crystal. The ordered array of atoms in the lattice act to shadow and block the incoming and the scattered protons. For an ordered surface, the ion beam cannot access deeper atomic layers due to the shadowing effect of the atoms of the surface. This leads to a sharp peak of elastically scattered protons. Conversely, a disordered surface has a decreased ability to shadow and block the protons of the probe beam. As a consequence, the scattered spectrum of ions exhibits a significantly broader peak which can be correlated to a disordered layer thickness.

Using this technique, a reversible order-disorder transformation was observed on Pb(110) with disorder beginning in the temperature range of 450 - 560 K, where T_m for Pb is 600.7 K.¹ The thickness, l , of the disordered layer, as determined from analysis of the energy spectra of scattered protons, increased logarithmically with temperature beginning at 560 K $\{l \sim \ln[T_m/(T_m - T)]\}$. At temperatures above $T_m - 0.3$ K, the disordered layer thickness was observed to increase according to a power law ($l \sim [T_m - T]^{-1/3}$).² Further studies using MEIS were performed to determine the role of the crystal surface orientation in the melting process and to test the prediction that close-packed crystal surfaces are less prone to exhibit surface melting than loosely packed, open surfaces.³ Pb surfaces were again studied and the majority of the

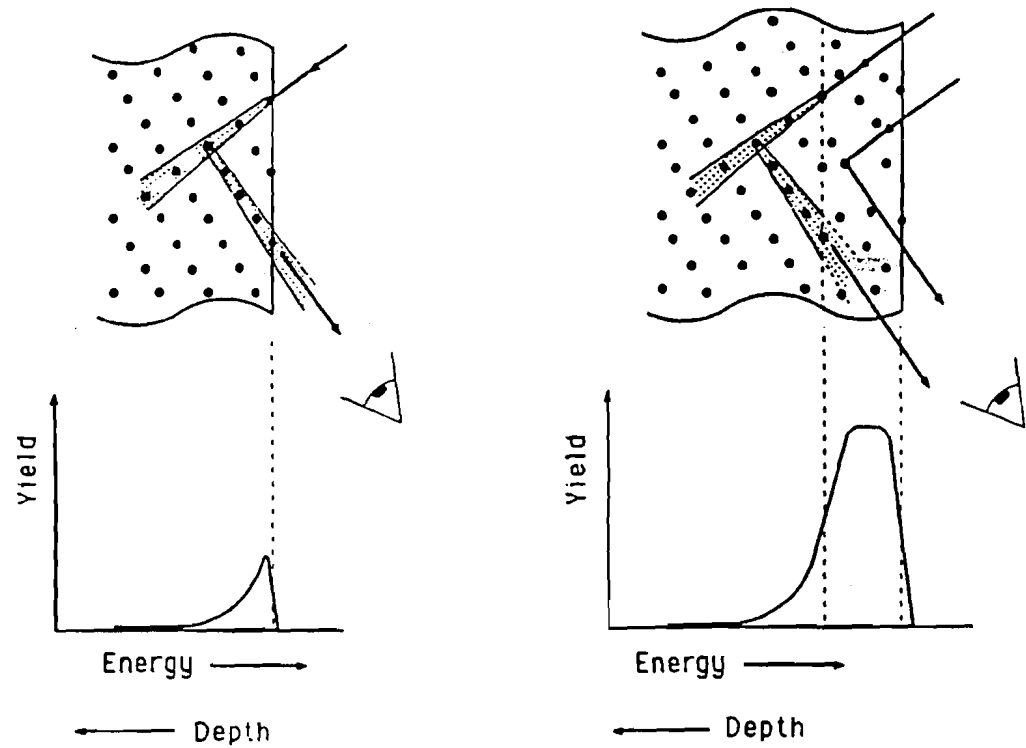


Figure 4. Schematic diagram of the technique of medium-energy ion scattering. The ordered surface on the left acts to shadow and block the proton beam, leading to a sharp energy peak of the back-scattered ions. A surface covered by a thin disordered layer is less effective in shadowing and blocking the proton beam and this leads to a greater back-scattered yield and a broadened energy peak. Reprinted with permission from Ref. 3 [B. Pluis, A. W. Denier van der Gon, J. F. van der Veen, and A. J. Riemersma, *Surf. Sci.* 239, 265 (1990)].

crystalline faces considered exhibited pronounced surface disordering with the exception of the vicinal surfaces within $\sim 17^\circ$ of the $\{111\}$ plane and $\sim 10^\circ$ of the $\{100\}$ plane. In contrast to this behavior, the close-packed Pb(111) surface was observed to remain ordered up to T_m . Many other high-index surfaces were observed to grow disordered surface layers in analogy to the (110) surface. The MEIS data giving the number of disordered atoms per unit area at temperatures near T_m versus surface orientation are shown in Fig. 5. These data are qualitatively consistent with predictions made from surface free energy measurements on Pb crystallites.⁴ These measurements, made using electron microscopy, displayed minima at the $\{111\}$ and $\{100\}$ orientations.⁴ The free energy data obtained from electron microscopy, however, predicted a significantly smaller zone around the $\{100\}$ plane where pronounced disorder is absent. In addition to the experiments on Pb, the importance of surface orientation was demonstrated with MEIS on Al(110) and Al(111) with Al(110) displaying surface melting and Al(111) remaining ordered.⁵ The packing density of face-centered-cubic crystals, shown in Fig. 6 for the low-index faces, seems to influence the structural stability of the surface with open surfaces exhibiting pronounced disordering below T_m and close-packed surfaces remaining ordered up to T_m .

Several other techniques were used to study the surface melting of Pb(110) and other fcc metal surfaces. These experiments supported the results obtained from MEIS. Some of these techniques include x-ray photoelectron diffraction (XPD),⁶ low-energy electron diffraction (LEED),⁷ x-ray scattering,⁸ UV photoelectron spectroscopy,⁹ and quasielastic atom scattering.¹⁰ The first two techniques, XPD and LEED, yielded temperatures for the onset of surface disorder on Pb(110) of 530 K⁶ and 543 K^{7a,b}, respectively, far below the bulk melting temperature of 600.7 K. XPD and LEED also

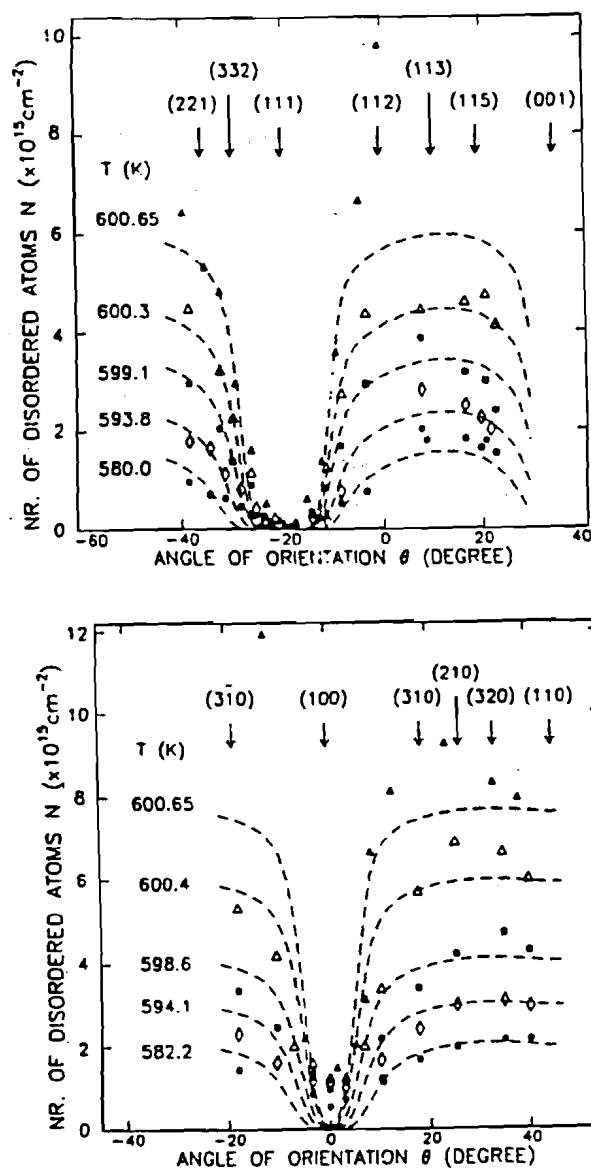


Figure 5. MEIS data showing the number of disordered atoms per unit area versus surface orientation and temperature. Prominent disorder is seen for most crystalline orientations with the exception of the (111) and (100) faces. Reprinted with permission from Ref. 3 [B. Pluis, A. W. Denier van der Gon, J. F. van der Veen, and A. J. Riemersma, *Surf. Sci.* 239, 265 (1990)].

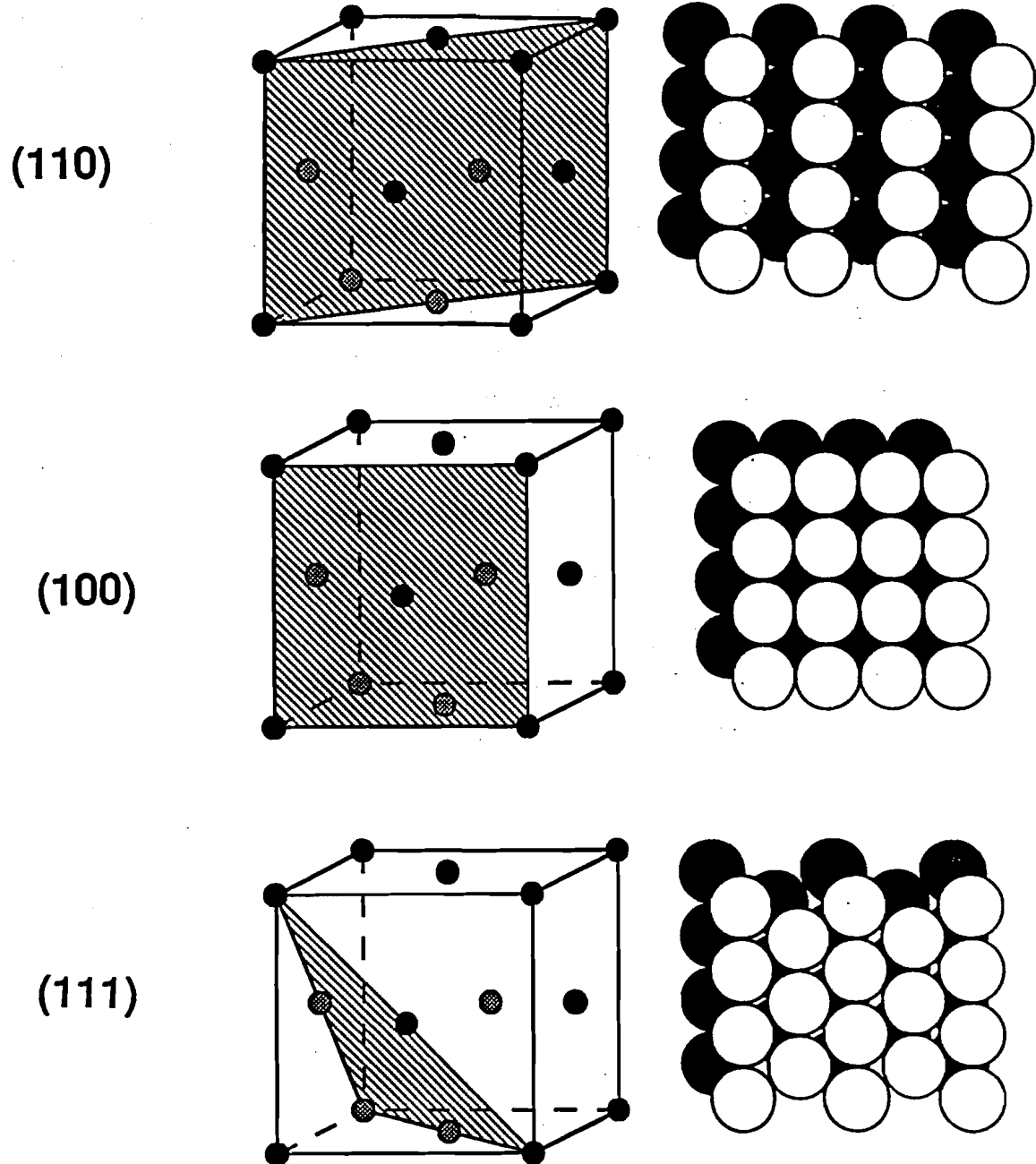


Figure 6. Diagram of the surface packing of the three low-index faces of an fcc metal. The open (110) surface has the lowest degree of surface packing while the (111) surface is close-packed.

revealed another interesting aspect of surface melting: the disordering observed on Pb(110) is anisotropic. The measured diffraction intensities vanished at different temperatures and rates for different probed azimuths of the crystal. The diffraction intensity of the $[1\bar{1}0]$ azimuth was observed to vanish at 580 K. In contrast to this, the diffraction intensity of the $[001]$ azimuth remained visible up to T_m . This was explained by the differing atomic spacing of the two orthogonal azimuths. The $[1\bar{1}0]$ azimuth has an atomic spacing that is nearly identical to that of the liquid. Apparently, for the $[1\bar{1}0]$ azimuth, the similarity in atomic spacing to the bulk liquid makes the transition from order to disorder energetically favorable at a lower temperature as compared with other azimuths. A subsequent study using MEIS confirmed the anisotropic disordering on Pb(110).¹¹ In addition, anisotropic disordering on Pb(100) was observed using XPD.¹² The anisotropic behavior of disordering is fundamentally related to the fact that the disordered layer is strongly influenced by the presence of the underlying ordered substrate. This has led several researchers to refer to the disordered surface layer as a *quasiliquid* layer.

A recent MEIS study on Pb(111) and vicinal surfaces revealed another interesting aspect of surface melting.¹³ These experiments indicated that vicinals with miscut angles $\theta < 2^\circ$ remain ordered up to T_m , while vicinals with $\theta > 13.9^\circ$ exhibited pronounced surface melting. Vicinals with $2^\circ < \theta < 13.9^\circ$ exhibited *surface-melting-induced faceting*, where the surface was observed to decompose into ordered, “dry” facets and “melted” facets. These facets coexist on the surface at temperatures near T_m . The MEIS experiments on Pb(111) and vicinal surfaces were performed at a temperature of $T_m - 0.05$ K. Surface-melting-induced faceting is thought to be responsible for the observed thermal step collapsing on Pb(111).¹⁴ In addition, the phenomenon of faceting has been observed to occur on a macroscopic level. Faceting of micron-sized Pb crystallites was observed using scanning electron microscopy.^{15,16}

A theoretical treatment based on a free energy analysis predicted the faceting behavior in these experiments.¹⁷

A further MEIS study was performed on Pb(100) and vicinal surfaces.¹⁸ The packing density of these surfaces is intermediate to that of Pb(110) and Pb(111). The experiments showed that a limited amount of disorder began to form on Pb(100) at $T > 500$ K with the degree of disorder on the considered vicinal surfaces increasing with increasing miscut angle. A logarithmic increase of the disordered layer thickness was observed on Pb(100) up to $T_m - 2$ K, where the thickness saturated at ~ 1.3 monolayers, measured up to $T_m - 0.05$ K. For the vicinal surfaces, the maximum amount of disorder was observed to increase from ~ 1.9 to ~ 3.5 monolayers for the 5° and 10° miscuts, respectively. This behavior, is known as *incomplete surface melting*, and is in contrast to the divergence of the disordered layer thickness on Pb(110). The disordered layer that forms is stable up to T_m . In addition, no faceting was observed in these experiments. Evidently, the formation of the disordered layer on Pb(100) energetically precludes a faceting transformation. The phenomenon of incomplete surface melting has also been observed on Ge(111)¹⁹ and the (100) face of the molecular crystal caprolactam.²⁰

2.2 MEAN-FIELD THEORY TREATMENT

The functional character of the growth laws for the disordered layer thickness have been predicted by several means.²¹ The most successful models have utilized a mean-field theory treatment.²² In these theories, the free energy is constructed in terms of a scalar order parameter. Using the phenomenological Landau theory for phase transformations, the free energy of a surface covered by a thin disordered layer is given by the following expression:²²

$$F(\ell) = (\gamma_{sl} + \gamma_{lv}) + \Gamma_{SR} + \Gamma_{LR} + \ell L_m \left(1 - \frac{T}{T_m}\right), \quad (2.2.1)$$

where ℓ is the thickness of the disordered layer; γ_{sl} and γ_{lv} are the interfacial free energies of the solid-liquid and liquid-vapor interfaces, respectively; Γ_{SR} and Γ_{LR} are the free energy contributions due to short-range and long-range forces, respectively; and L_m is the heat of fusion.

The terms of the free energy are interpreted as follows:

- $\gamma_{sl} + \gamma_{lv}$: Free energy corresponding to a surface covered by a disordered layer.

- $\Gamma_{SR} = \Delta\gamma \exp(-2\ell/\xi)$: ($\Delta\gamma = \gamma_{sv} - \gamma_{sl} - \gamma_{lv}$ is the free energy difference between a completely ordered surface and a surface covered with a disordered layer. The correlation length ξ is the distance in the bulk liquid where the order parameter decreases by a factor of e .) This term models the ordering in the disordered film due to the short-range screened Coulomb interaction between the ions in the film and the ordered substrate. For $\Delta\gamma > 0$ this term results in a *repulsive* force per unit area between the solid-liquid and liquid vapor interfaces, favoring melting into the bulk of the crystal. For $\Delta\gamma < 0$ this term results in an attractive force per unit area between the interfaces.

- $\Gamma_{LR} = W/\ell^2$, where W is a constant: This term is associated with the long-range van der Waals potential that is due to the incomplete screening of the Coulomb potential within the disordered layer. This long-range component plays an important role when the disordered layer is relatively thick ($\geq 20 \text{ \AA}$).

• $lL_m(1 - T/T_m)$: This term represents the increase in free energy associated with the existence of a disordered surface layer at a temperature *below* T_m . For $T < T_m$ this term is effectively an attractive force per unit area between the solid-liquid and liquid-vapor interfaces. The influence of this term decreases with temperature.

For small disordered layer thicknesses, the long-range contribution to the free energy, Γ_{LR} , can be neglected and the equilibrium disordered layer thickness, l_{eq} , is found by minimizing the free energy,

$$\frac{dF(l)}{dl} = 0 \quad (2.2.2)$$

When this is done, l_{eq} is found to be

$$l_{eq} = l_{eq}(T, \{hkl\}) = \frac{\xi}{2} \ln \left[\frac{2T_m \Delta\gamma}{\xi L_m (T_m - T)} \right], \quad (2.2.3)$$

where the functional dependence of the disordered layer thickness on the Miller indices $\{hkl\}$ of the considered crystalline surface is due to the orientation dependence of the interfacial free energy difference, $\Delta\gamma$. From Eq. 2.2.3, the well-known condition for surface melting is extracted:

$$\Delta\gamma > 0 \quad [\gamma_{sv} > \gamma_{sl} + \gamma_{lv}] \quad (2.2.4)$$

This expression states that above a certain temperature it becomes energetically favorable for the surface to form a disordered layer between the ordered bulk and the

vapor. In this model, a surface that has $\Delta\gamma < 0$ for all temperatures below T_m remains ordered and does not exhibit surface melting. A plot of the components of Eq. 2.2.1 is shown in Fig. 7 using the parameters of Pb(110). Surface disordering and logarithmic growth of the disordered layer thickness have been observed on Pb(110) and other high-index faces of Pb,^{1,3} and on Al(110).⁵ The close-packed Pb(111)³ and Al(111)⁵ surfaces were shown to demonstrate nonmelting and evidently have $\Delta\gamma < 0$ for all temperatures up to their respective bulk melting points. Finally, for surfaces that exhibit complete surface melting (i.e. the thickness of the disordered layer diverges as T_m is approached), at temperatures extremely close to T_m the long-range contribution to the free energy becomes significant and leads to a crossover in the functional dependence of the disordered layer thickness from logarithmic to a power law form, $l \sim (T_m - T)^{-1/3}$. The functional crossover has been observed on Pb(110) above $T_m - 0.3$ K.² In summary, Eq. 2.2.1 accurately describes the disordering of the fcc(110) surfaces that have been experimentally studied.

The free energy expression of Eq. 2.2.1, however, does not describe the finite, nondiverging melting behavior observed on Pb(100). A recent model has been developed that includes the effect of the solid substrate on the energetics of the disordered layer.²³ In this model, the ordered substrate induces a periodic density modulation in the disordered film in a direction parallel to the solid-disordered layer interface. The free energy function that describes the effect of layering is given by

$$F(\ell) = L_m \left(1 - \frac{T}{T_m}\right) \ell - \Delta\gamma - a \cos(k_l \ell) \cdot \exp\left(-\frac{\ell}{\xi}\right) + b \exp\left(-\frac{2\ell}{\xi}\right) + \Gamma_{LR} \quad (2.2.5)$$

Here, $\Delta\gamma = -a + b$, with a and b constants, and k_l is the magnitude of the wavevector corresponding to the first maximum in the structure factor of the bulk liquid. The other

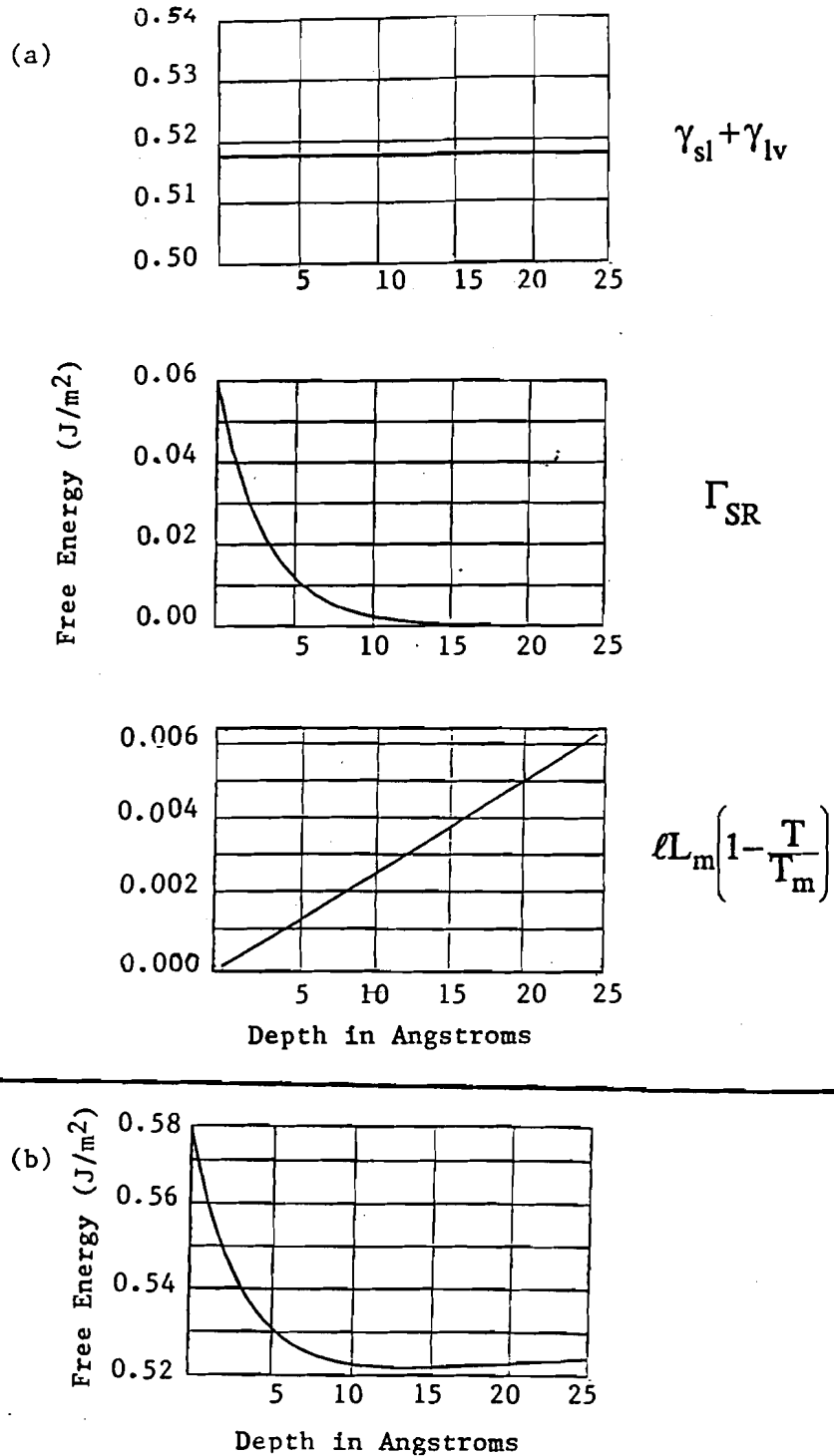


Figure 7. (a) Components of the free energy of the disordered layer on Pb(110) at $T/T_m = 0.99$. (b) Total free energy of disordered layer on Pb(110) at $T/T_m = 0.99$. The minimum in the free energy occurs at a disordered layer thickness of approximately 14 Å.

symbols are defined as in Eq. 2.2.1. For $a \ll b$, the expression reduces to Eq. 2.2.1 where the effect of layering in the disordered layer is not considered. The third term in Eq. 2.2.5 models the layering effect in the disordered layer. This term favors disordered film thicknesses that are an integral multiple of $2\pi/k_l$ ($2\pi/k_l$ for Pb is $\sim 2.86 \text{ \AA}$). The term is important when the interlayer spacing of the crystal is comparable to $2\pi/k_l$. The interlayer spacings for Pb(110), Pb(100), and Pb(111) are 1.75, 2.48, and 2.86 \AA , respectively. Therefore, the effect of layering is expected to be significant for Pb(100). Experimental evidence suggests that the magnitude of $\Delta\gamma$ for Pb(111) precludes even a layered melting transition.

The layering free energy is plotted in Fig. 8 for the parameters of Ge(111) at $T/T_m = 0.99$.¹⁹ The behavior of the free energy is oscillatory with minima occurring at $2n\pi/k_l$, where n is an integer. Near T_m , the global minimum of the free energy occurs at $2\pi/k_l$ and the system is stable with a disordered film of this thickness. Since all of the successive minima have a larger free energy, the disordered layer thickness remains constant and the layer does not act as a nucleation site for further melting. This is in contrast to the diverging disordered layer thickness on crystal faces such as Pb(110)¹⁻³ and Al(110)⁵. At higher temperatures, due to the decreasing influence of the first term in Eq. 2.2.5, the free energy minimum occurs at a larger disordered layer thickness that is a multiple of $2\pi/k_l$. Therefore, for surfaces such as Pb(100) and Ge(111) which exhibit incomplete surface melting, successive "layering transitions" may occur where the disordered layer thickness increases in discrete steps.

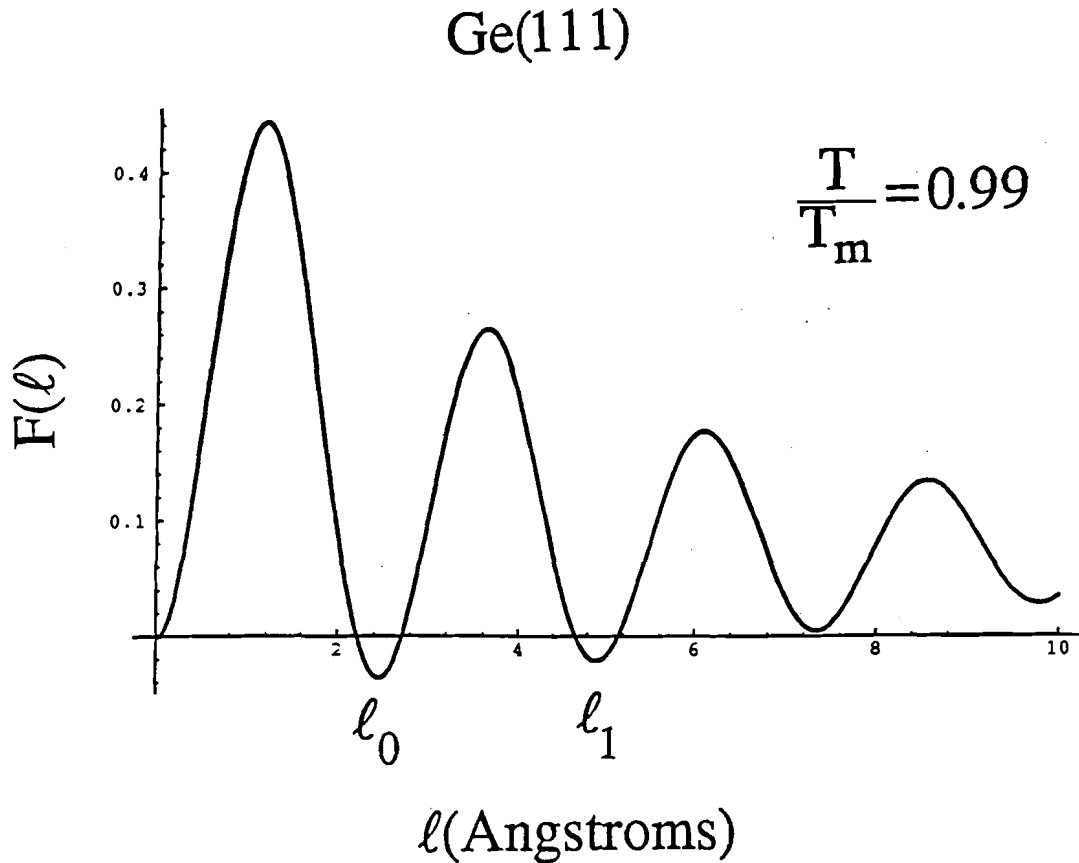


Figure 8. Free energy $F(l)$ of the disordered layer on Ge(111) at $T/T_m = 0.99$ in the layering model of Chernov and Mikheev (Ref. 23). The oscillatory character of $F(l)$ is due to the periodic density modulation in the disordered layer induced by the solid substrate. The disordered layer thickness does not diverge as T_m is approached. The minimum in the free energy occurs at $l_0 = 2\pi/k_1 = 2.3 \text{ \AA}$.

2.3 MOLECULAR DYNAMICS SIMULATION

Along with the experimental attention being given to surface melting, there have been many recent molecular dynamics (MD) studies examining the structural behavior of surfaces. Early pairwise Lennard-Jones potentials, while successfully modelling the behavior of noble-gas solids,²⁴ proved to be inadequate for the description of metals. The many-body nature of metallic bonding that is explicitly accounted for in more recent models accurately treats the distribution of electronic charge around the surface atoms. This charge distribution determines important surface properties such as anharmonicity, surface relaxation and surface reconstruction. These properties emphasize that the surface is not a simple termination of the bulk. The many-body potentials take the form:

$$V = \frac{1}{2} \sum_{\substack{i,j=1 \\ j \neq i}}^N \phi(r_{ij}) + \sum_{i=1}^N U(n_i), \quad (2.3.1)$$

where

$$n_i = \sum_{\substack{i,j=1 \\ j \neq i}}^N \rho(r_{ij}) \quad (2.3.2)$$

is a superposition of atomic charge densities and r_{ij} is the distance between atoms labelled i and j . The first term of Eq. 2.3.1 represents a sum over pairwise potentials, ϕ , while the second term models the many-body nature of the bonding. The parameters of the potentials are chosen to correctly predict many surface and bulk properties including lattice spacing, elastic constants, vibrational frequencies, surface reconstructions, thermal expansion, and the bulk melting temperature. Motion of the individual ions in a MD cell are followed by solving Newton's equation of motion for each atom of the MD lattice:

$$Ma(t) = - \sum_{\substack{i,j=1 \\ j \neq i}}^N \text{grad}[V(r_{ij})], \quad (2.3.3)$$

where M is the mass of the ion, a is the corresponding acceleration, and $V(r_{ij})$ is the effective many-body potential. Parameters that determine the degree of order of a crystal can be readily obtained from the results of the simulation. For example, in MD simulations of Au surfaces, the in-plane orientational order parameter was examined to judge the degree of order of a surface.²⁵ This parameter is a summation over nearest-neighbor pairs of a term that contains bond-angle information, providing a figure of merit for crystalline order. Further parameters that are examined in the surface melting simulations are (i) the surface self-diffusion coefficient, which reflects the ability of a surface atom to move through the disordered surface layer, (ii) the near-surface density profile, (iii) the average energy per atom, which is related to the surface atomic vibrational amplitude, and (iv) pair correlation functions, which indicate the probability of finding successive nearest neighbors at their respective lattice sites.

Using MD simulations, the surface melting behavior of several fcc metals have been modelled including Al²⁶⁻²⁸, Au^{25,29-32}, Cu³³⁻³⁸, Ni^{39,40}, and Pb⁴¹. The general trend suggests that the propensity of a surface to remain stable up to T_m is influenced by the surface packing density, in agreement with experimental studies. The studies that treated the open fcc(110) surfaces demonstrated the tendency of this surface to disorder below T_m .^{26,27,30,31,34-37,40} Some of these studies showed qualitative agreement to the logarithmic growth law that is evident from the experiments and predicted from the mean-field theory treatment.^{30,31,34} The disorder on the unreconstructed fcc(110) surface seems to be mediated by the formation of adatom-vacancy pairs.^{26,27,34-37,40} Indeed, studies that calculated the formation energy of

vacancies, E_v , on various crystalline faces determined that E_v for a (111) surface is larger than that for a (110) surface by as much as a factor of 4, showing the tendency of the open surface to form defects.²⁶ Table 1 gives the formation energies of adatom-vacancy pairs for a variety of fcc metal surfaces as determined by MD simulations. The stability of the fcc(111) surface relative to the open fcc(110) surface is evident. Fig. 9 shows snapshots of the ionic configuration from an MD simulation of Cu(110) performed at various temperatures.³⁷ The melting temperature from the model was determined to be 1240 ± 25 K. Adatom-vacancy formation is clearly evident becoming more prominent with increasing temperature. Next to the snapshots are corresponding plots of the trajectories of the near-surface atoms showing the increasing depth of the disorder with temperature. In the MD simulations that examined (111) surfaces, surface stability up to T_m was observed as well as superheating.^{29,31,37,38,41} The (100) surface has been modelled less extensively.^{32,37,39} One study that treated the low-index faces of Cu showed a weak disordering on Cu(100) just below T_m , behavior that is qualitatively intermediate to that observed on the (110) and (111) surfaces.³⁷ Trajectory plots of the three low-index faces of Cu are shown in Fig. 10.³⁷ The orientational dependence of surface melting is evident by the differing disordered layer thickness of the crystalline faces. These simulations are in qualitative agreement with experimental data. In this series of MD simulations, no latent heat was observed in the first three crystal layers.³⁷ This supports the view that surface melting is a continuous process with properties differing from bulk melting. In addition, the high-temperature structural behavior of vicinal surfaces of Au(100) was studied using the many-body “glue” potential.³² In both the studies of Cu(100)³⁷ and the vicinal surfaces of Au(100),³² structural modulation in the disordered film was evident.

Table 1. Adatom-vacancy formation energies, E_v , according to molecular dynamics simulation

Surface	E_v (eV)	Reference
Al(110)	0.3	26
Al(111)	1.3	26
Cu(110)	0.4, 0.35, 0.39	34, 35, 37
Cu(100)	0.86	37
Cu(111)	1.92	37
Ni(110)	1.0	40

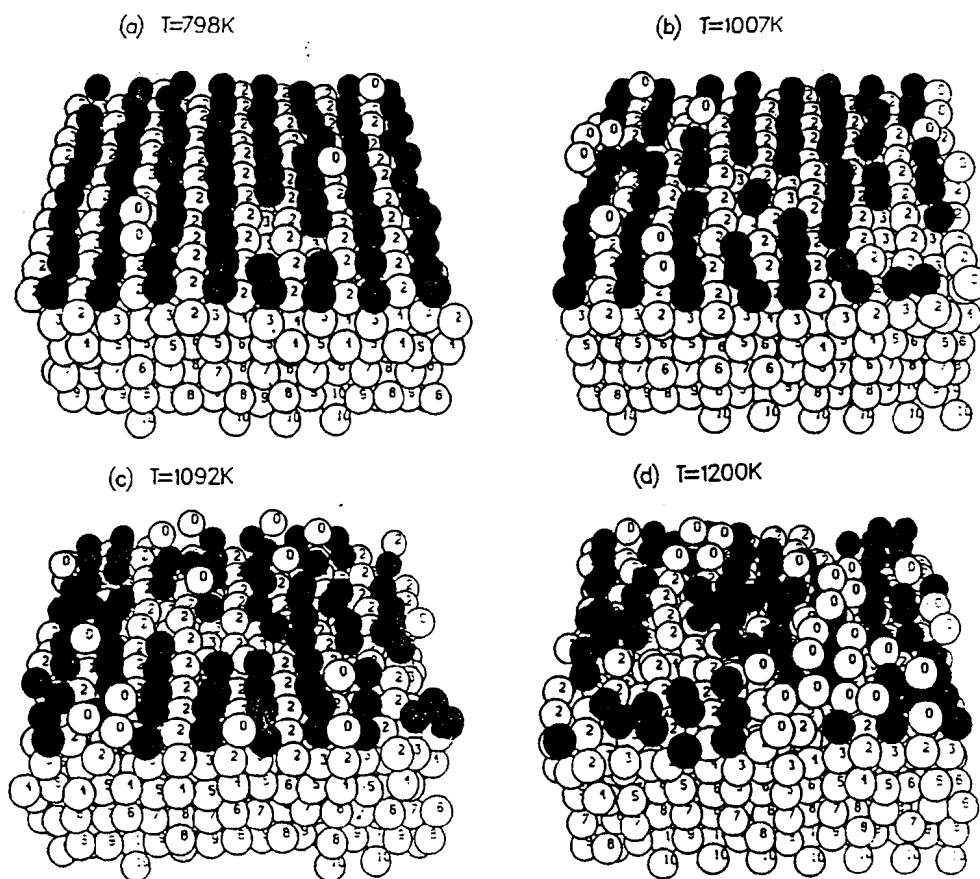


Figure 9. Snapshots from a molecular dynamics simulation of Cu(110). The melting temperature of the model was 1240 ± 25 K. The black spheres represent surface atoms while the spheres labelled 0 represent adatoms. Note the increase in the number of adatoms with temperature leading to a disordered surface at $T_m - 40$ K. Reprinted with permission from Reference 37 [H. Hakkinen and M. Manninen, Phys. Rev. B 46, 1725 (1992)].

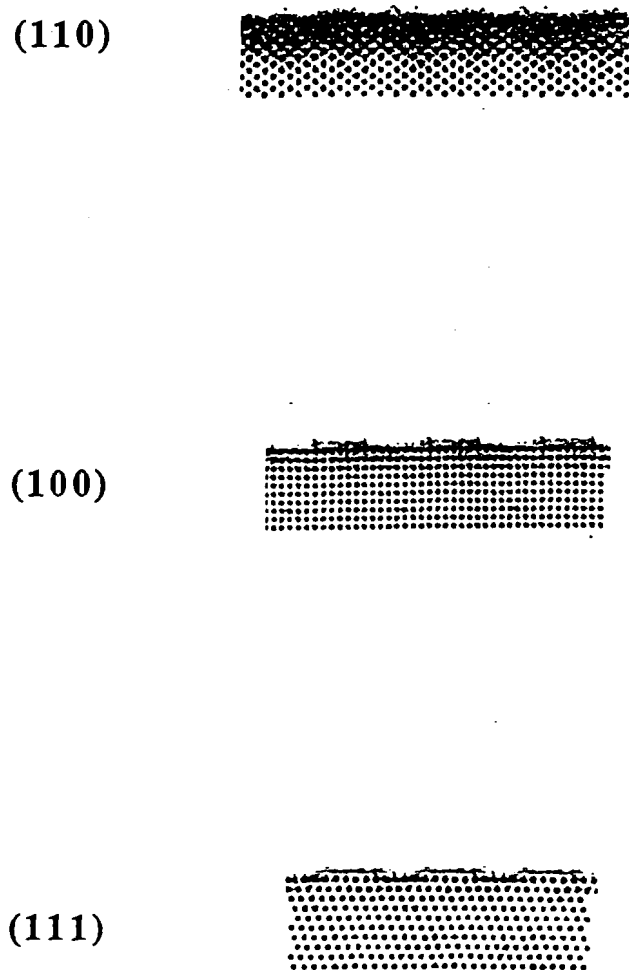


Figure 10. Atomic trajectory plots of the low-index faces of Cu near T_m . Cu(110) is seen to exhibit prominent disordering, while Cu(111) remains ordered. This demonstrates the orientation dependence of surface melting. Reprinted with permission from Reference 37 [H. Hakkinen and M. Manninen, Phys. Rev. B 46, 1725 (1992)].

Several fcc(110) surfaces exhibit surface reconstruction and this influences the mechanism of melting. A well-studied example of this is Au(110).³⁰ At low temperatures, Au(110) exhibits a (1×2) “missing row” reconstruction. The surface is described as “consisting of a series of slanted, narrow (111) microfacets”.³⁰ As the MD cell is heated, the reconstruction disappears at $T \sim 850$ K, where the bulk melting temperature of the simulation is $T_m = 1327$ K. Above 850 K, a disordered phase consisting of adatoms is present. At $T \sim 1000$ K the disordered adatom layer collapses into the second layer to form a dense disordered liquid-like layer with few adatoms present.

The phenomenon of surface-melting-induced faceting has also been observed in molecular dynamics simulations. Au(111) and vicinals⁴² and vicinals of Pb(111)⁴¹ have exhibited microscopic faceting. The study that examined Au(111) revealed that surface reconstruction plays an important role in faceting.⁴² At low temperatures, Au(111) has a $(23 \times 3^{1/2})$ reconstructed unit cell. In the simulations, the (534) vicinal of Au(111) was observed to facet near T_m as a result of this reconstruction. In contrast to this behavior, Pb(111), which does not reconstruct, is free of faceting near T_m .⁴¹

The experimental and simulation data on surface melting provide a picture of the process. The route to surface melting includes anharmonic surface vibrations, which are prominent on loosely-packed or high-index crystal faces. Large-amplitude atomic vibrations eventually lead to the breaking of nearest-neighbor bonds and the creation of adatoms. Surface roughening, the spontaneous formation of atomic steps on a surface at a temperature below T_m , has also been suggested as a precursor to surface melting.⁴³ Nucleation of disorder at defects such as surface steps most likely play an important role in the melting process. Surface roughening has been observed on various crystal surfaces.⁴⁴ The role of surface roughening in the surface melting transition is unclear, however. Pb(110), a surface which exhibits surface disordering,

has been observed with high-resolution LEED to exhibit a roughening transition at 415 ± 20 K.^{7c}

A step defect on a surface above the roughening transition temperature or simply on an imperfect crystal surface (caused by abrasive polishing or ion bombardment) may act as a nucleation site for disordering. Consider a step defect on a surface as shown in Fig. 11. The edge atoms on the step vibrate in an anharmonic and anisotropic fashion. The anharmonicity of edge atoms on steps is thought to exceed that of the atoms on the terrace. This behavior was proposed to explain the data obtained from an MEIS study of Au(110).⁴⁵ The enhanced vibrations of the edge atoms on a step lead to bond-breaking and the creation of adatoms which diffuse on the terraces.⁴⁶ The energy necessary to create an adatom from a surface step may be as much as a factor of two less than the energy necessary to form an adatom-vacancy pair on a flat surface.⁴⁶ Therefore, surface steps should act as sources of adatoms at high temperatures when anharmonic vibrations become prominent. If surface melting is indeed nucleated at defects on a rough surfaces, the disorder on the surface would be somewhat heterogeneous, reflecting the spatial distribution of steps on the surface. The nature of this disorder would differ from a surface covered with a homogeneous disordered layer. This difference could be detected by an experimental technique with sufficient depth resolution. MEIS has the potential for achieving the necessary depth resolution to examine the nucleation of surface disorder.¹⁸

In summary, the results of experiments and computer modeling suggest that the tendency of a surface to disorder below T_m depends on several factors. These include (i) the orientation-dependent surface-packing density, which influences the vibrational properties of surface atoms, (ii) the formation energy of surface defects such as adatoms and vacancies, and (iii) the ability of adatoms to diffuse on the surface.

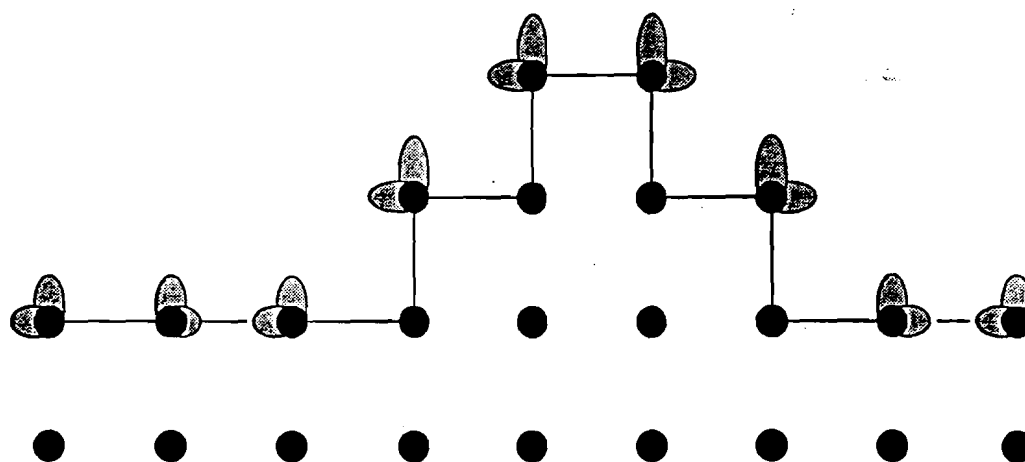


Figure 11. Anharmonic and anisotropic vibrations of edge atoms on surface steps lead to the creation of adatoms. The ellipses on the surface atoms represent enhanced vibrational amplitudes.

REFERENCES

1. J. W. M. Frenken and J. F. van der Veen, *Phys. Rev. Lett.* **54**, 134 (1985); J. W. M. Frenken, P. M. J. Maree, and J. F. van der Veen, *Phys. Rev. B* **34**, 7506 (1986).
2. B. Pluis, T. N. Taylor, D. Frenkel, and J. F. van der Veen, *Phys. Rev. B* **40**, 1353 (1989).
3. B. Pluis, A. W. Denier van der Gon, J. F. van der Veen, and A. J. Riemersma, *Surf. Sci.* **239**, 265 (1990).
4. J. C. Heyraud and J. J. Metois, *Surf. Sci.* **128**, 334 (1983).
5. A. W. van der Gon, R. J. Smith, J. M. Gay, D. J. O'Connor, and J. F. van der Veen, *Surf. Sci.* **227**, 143 (1990).
6. U. Breuer, O. Knauff, and H. P. Bonzel, *Phys. Rev. B* **41**, 10848 (1990); *J. Vac. Sci. Technol. A* **8**, 2489 (1990).
7. (a) K. C. Prince, U. Breuer, and H. P. Bonzel, *Phys. Rev. Lett.* **60**, 1146 (1988); (b) U. Breuer, H. P. Bonzel, K. C. Prince, and R. Lipowsky, *Surf. Sci.* **223**, 258 (1989); (c) H. -N. Yang, T. -M. Lu, and G. -C. Wang, *Phys. Rev. Lett.* **63**, 1621 (1989).
8. P. H. Fuoss, L. J. Norton, and S. Brennan, *Phys. Rev. Lett.* **60**, 2046 (1988); B. Pluis, J. M. Gay, J. W. M. Frenken, S. Gierlotka, J. F. van der Veen, J. E. MacDonald, A. A. Williams, N. Piggins, and J. Als-Nielsen, *Surf. Sci.* **222**, L845 (1989).
9. P. Thiry, F. Jezequel, and Y. Petroff, *J. Vac. Sci. Technol. A* **5**, 892 (1987).
10. J. W. M. Frenken, J. P. Toennies, and Ch. Woll, *Phys. Rev. Lett.* **60**, 1727 (1988).
11. A. W. Denier van der Gon, H. M. van Pinxteren, J. W. M. Frenken, and J. F. van der Veen, *Surf. Sci.* **244**, 259 (1991).

12. E. A. Murphy, H. E. Elsayed-Ali, K. T. Park, J. Cao, and Y. Gao, *Phys. Rev. B* **43**, 12615 (1991).
13. H. M. van Pinxteren and J. W. M. Frenken, *Europhys. Lett.* **21**, 43 (1993).
14. H. -N. Yang, T. -M. Lu, and G. -C. Wang, *Phys. Rev. Lett.* **62**, 2148 (1989).
15. J. C. Heyraud, J. J. Metois, and J. M. Bermond, *J. Cryst. Growth* **98**, 355 (1989).
16. A. Pavlovska, K. Faulian, and E. Bauer, *Surf. Sci.* **221**, 233 (1989).
17. P. Nozieres, *J. Phys. France* **50**, 2541 (1989).
18. H. M. van Pinxteren and J. W. M. Frenken, *Surf. Sci.* **275**, 383 (1992).
19. A. W. Denier van der Gon, J. M. Gay, J. W. M. Frenken, and J. F. van der Veen, *Surf. Sci.* **241**, 335 (1991).
20. S. Chandavarkar, R. M. Geertman, and W. H. de Jeu, *Phys. Rev. Lett.* **69**, 2384 (1992).
21. See, for example, Y. Teraoka, *Surf. Sci.* **281**, 317 (1993) or A. A. Korneev, O. V. Tapinskaya, V. N. Tronin, and V. I. Troain, *Mod. Phys. Lett. B* **5**, 1759 (1991).
22. B. Pluis, D. Frenkel, and J. F. van der Veen, *Surf. Sci.* **239**, 282 (1990).
23. A. A. Chernov and L. V. Mikheev, *Phys. Rev. Lett.* **60**, 2488 (1988); *Physica A* **157**, 1042 (1989).
24. R. M. J. Cotterill and L. B. Pedersen, *Solid State Comm.* **10**, 439 (1972); J. Q. Broughton and L. V. Woodcock, *J. Phys. C* **11**, 2743 (1978).
25. P. Carnevali, F. Ercolessi, and E. Tosatti, *Phys. Rev. B* **36**, 6701 (1987).
26. P. Stoltze, J. K. Nørskov, and U. Landman, *Phys. Rev. Lett.* **61**, 440 (1988); *Surf. Sci.* **220**, L693 (1989).
27. P. Stoltze, *J. Chem. Phys.* **92**, 6306 (1990).
28. J. Mei and J. W. Davenport, *Phys. Rev. B* **46**, 21 (1992).

29. P. Carnevali, F. Ercolessi, and E. Tosatti, *Surf. Sci.* **189/190**, 645 (1987).
30. F. Ercolessi, S. Iarlori, O. Tomagnini, E. Tosatti, and X. J. Chen, *Surf. Sci.* **251/252**, 645 (1991).
31. F. Ercolessi, O. Tomagnini, S. Iarlori, and E. Tosatti, NATO-Advanced Research Workshop *Manipulation of Atoms in High Fields and Temperatures: Applications*, NATO-ASI-E Series, Applied Sciences, edited by Vu Thien Binh, N. Garcia, and K. Dransfeld (Kluwer Academic, Dordrecht, Boston, 1992). The functional form of the many-body potential in Eqs. 2.3.1 and 2.3.2 is taken from this work, which utilizes the so-called "glue" potential.
32. G. Bilalbegovic, F. Ercolessi, and E. Tosatti, *Surf. Sci.* **280**, 335 (1993).
33. J. F. Lutsko, D. Wolf, S. R. Phillpot, and S. Yip, *Phys. Rev. B* **40**, 2841 (1989).
34. R. N. Barnett and U. Landman, *Phys. Rev. B* **44**, 3226 (1991).
35. P. D. Ditlevsen, P. Stoltze, and J. K. Nørskov, *Phys. Rev. B* **44**, 13002 (1991).
36. B. Loisel, J. Lapujoulade, and V. Pontikis, *Surf. Sci.* **256**, 242 (1991).
37. H. Hakkinen and M. Manninen, *Phys. Rev. B* **46**, 1725 (1992).
38. H. Hakkinen and U. Landman, *Phys. Rev. Lett.* **71**, 1023 (1993).
39. E. T. Chen, R. N. Barnett, and U. Landman, *Phys. Rev. B* **40**, 924 (1989).
40. *ibid*, *Phys. Rev. B* **41**, 439 (1990).
41. G. Bilalbegovic, F. Ercolessi, and E. Tosatti, *Europhys. Lett.* **17**, 333 (1992).
42. G. Bilalbegovic, F. Ercolessi, and E. Tosatti, *Surf. Sci. Lett.* **258**, L676 (1991); *Europhys. Lett.* **18**, 163 (1992).
43. J. F. van der Veen and J. W. M. Frenken, *Surf. Sci.* **252/252**, 1 (1991).
44. For a review of surface roughening, see E. H. Conrad, *Prog. Surf. Sci.* **39**, 65 (1992).

45. A. Hoss, M.Nold, P. von Blanckenhagen, and O. Meyer, *Phys. Rev. B* **45**, 8714 (1992).
46. D. Gorse and J. Lapujoulade, *Surf. Sci.* **162**, 847 (1985).

CHAPTER 3: TIME-RESOLVED REFLECTION HIGH-ENERGY ELECTRON DIFFRACTION (RHEED)*

3.1 CONVENTIONAL RHEED

The principle technique used in the work presented here is reflection high-energy electron diffraction (RHEED). RHEED has been in use since 1928 when Sh. Nishikawa and S. Kikuchi used it to examine the structure of surfaces.^{1,2} Since that time, RHEED has been widely used as a probe of crystal structure and growth. RHEED relies upon the wave nature of the electron and the fact that electrons interact strongly with solids. A schematic diagram of RHEED is shown in Fig. 12. Electrons are produced, usually from thermionic emission from a hot filament, then collimated and accelerated to energies in the 10 - 100 keV range. These energies correspond to de Broglie wavelengths of $\lambda \sim 0.12 - 0.04 \text{ \AA}$, ideal for probing the structure of crystal lattices. In RHEED, the electron beam interacts with the surface at a glancing angle typically in the range of $1^\circ - 3^\circ$, measured relative to the plane of the surface. The resulting diffraction pattern is detected on a phosphor screen located normal to the direction of the electron beam.

The structure of the RHEED pattern can be understood by the von Laue condition for constructive interference:

$$k' - k = K, \quad (3.1.1)$$

where k' is the scattering wavevector, k is the wavevector of the incident electron beam, and K is a reciprocal lattice vector. The Ewald construction is a geometrical tool frequently used to describe RHEED and other types of diffraction.^{2,3} In this construction, a sphere of radius $|k| = 2\pi/\lambda$ is drawn in reciprocal space, where λ is the de Broglie wavelength of the electrons. Constructive interference will only occur in

* H. E. Elsayed-Ali and J. W. Herman, Rev. Sci. Instrum. 61, 1636 (1990); Appl. Phys. Lett. 57, 1508 (1990).

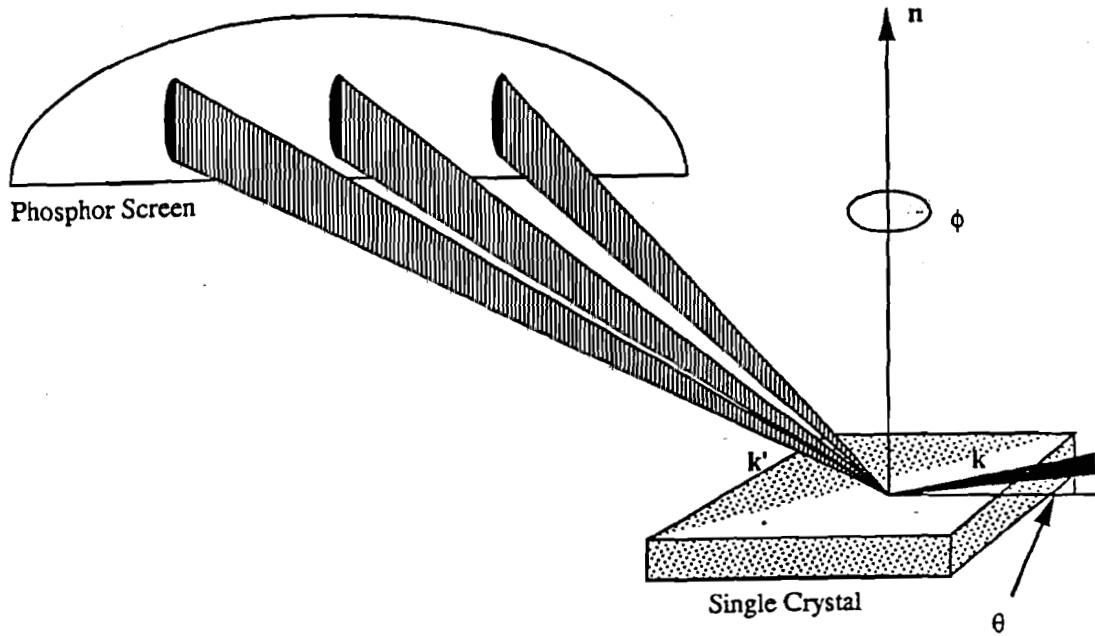


Figure 12. Schematic diagram of reflection high-energy electron diffraction (RHEED). The electron beam is incident on the surface at an angle θ , probing the first several atomic layers. The RHEED pattern, which consists of a series of streaks that are oriented perpendicular to the plane of the surface, is detected on a phosphor screen.

directions k' that satisfy the von Laue condition (3.1.1). For elastic scattering of the electrons, $|k'| = |k|$. This implies that possible scattering vectors must lie on the surface of the Ewald sphere in reciprocal space, where the von Laue condition is satisfied.

The Ewald construction is illustrated in Fig. 13 for low energy electrons. For low energy electrons, $|k|$ is on the order of reciprocal lattice dimensions. This is the case for low-energy electron diffraction (LEED). For two-dimensional systems such as crystal surfaces, reciprocal lattice *rods* result from the fact that multiple reciprocal lattice vectors satisfy the diffraction condition. These rods originate at points in reciprocal space and are directed normal to the surface. Geometrically, the von Laue condition and the condition for elastic scattering lead to constructive interference in the directions defined by the intersection of the Ewald sphere and the reciprocal lattice rods, since this corresponds to a wavevector difference that is a reciprocal lattice vector.

For typical RHEED energies of 10 - 100 keV, $|k|$ (the radius of the Ewald sphere) ranges from 50 - 160 \AA^{-1} . The lattice spacing for a metal such as Pb is $a = 4.95 \text{\AA}$; dimensions in reciprocal space are therefore on the order of $2\pi/a \sim 1.27 \text{\AA}^{-1}$. Thus, the radius of the Ewald sphere in the case of RHEED is typically much larger than the reciprocal lattice spacing. Therefore, with RHEED, a slice of reciprocal space is probed resulting in a set of diffraction spots or streaks in directions corresponding to constructive interference. This is illustrated in Fig. 14. For a single crystal with superior long-range order, the reciprocal lattice rods are effectively delta functions.⁴ Therefore, the intersection of the Ewald sphere and the reciprocal lattice rods results in a RHEED pattern consisting of spots. Diffraction from a non-ideal surface, however, results in broadened reciprocal lattice rods, leading to diffraction streaks instead of spots.⁴ For a flat single crystal, the RHEED pattern typically consists of a set of parallel streaks or elongated spots, oriented perpendicular to the surface of the sample.

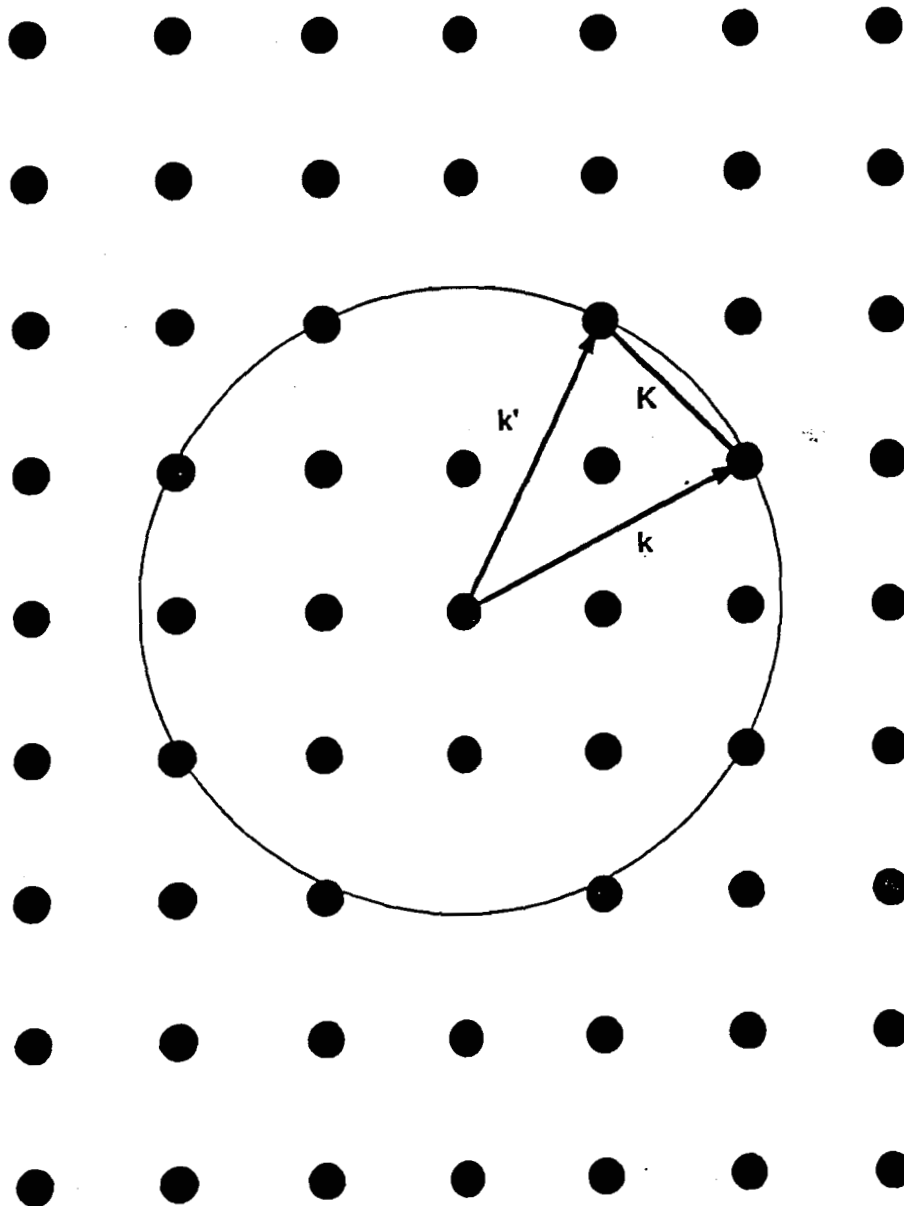
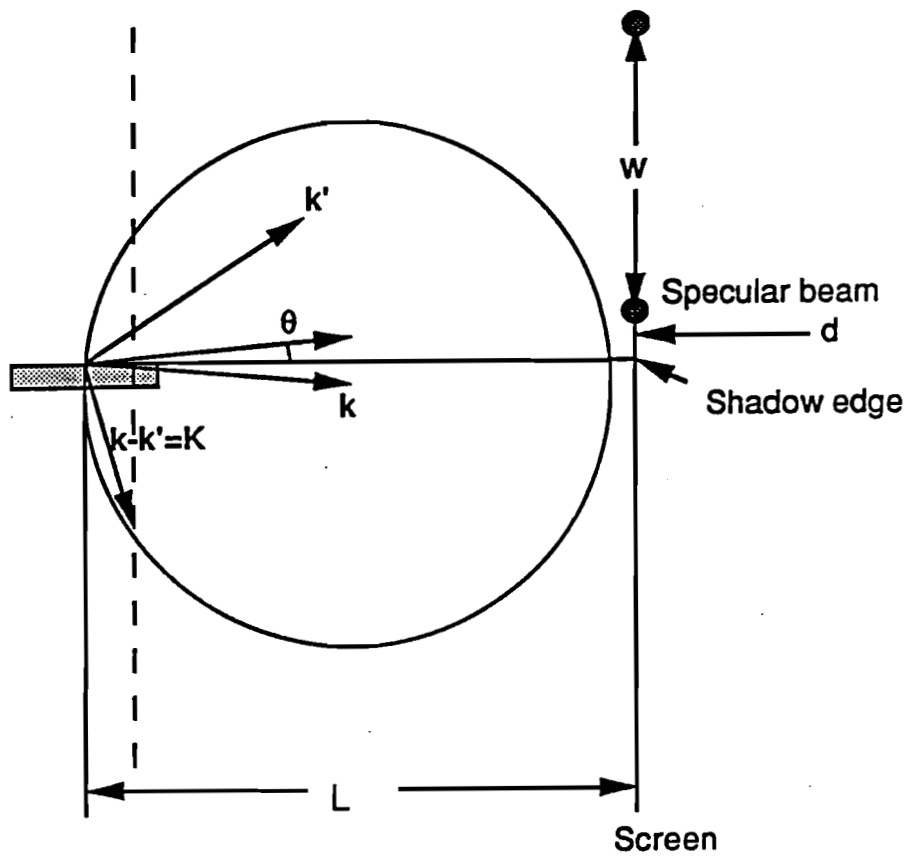


Figure 13. The Ewald construction for the elastic diffraction of low energy electrons. The diameter of the sphere is $2\pi/\lambda$, where λ is the de Broglie wavelength of the incident electrons. Constructive interference occurs in directions where the Ewald sphere intersects a point of the reciprocal lattice, satisfying the Laue diffraction condition.



$$\theta = \arctan(d/L)$$

$$w/L \sim a^*/|k|$$

Figure 14. Ewald construction for the case of RHEED. The Laue condition is satisfied for the scattering vector k' .

From the RHEED pattern, the streak spacing gives information on the reciprocal lattice spacing and hence the direct lattice spacing for the probed azimuth of the crystal. Using the streak spacing w on the detector screen, the sample-to-screen distance L , and the magnitude of the incident electron wavevector, the reciprocal lattice spacing a^* of the probed azimuth is determined (Fig. 15):

$$a^* = \frac{w|k|}{L} = \frac{2\pi w}{\lambda L} \quad (3.1.2)$$

In addition, the intensity of the RHEED streaks is related to the temperature of the surface through the Debye-Waller effect which results in a decreased number of elastically scattered electrons with increasing temperature. This will be discussed in more detail in the following section and in Appendix A.

The probed depth of the electron beam in the RHEED geometry is given by

$$d_p = d \sin \theta, \quad (3.1.3)$$

where θ is the angle of incidence of the electron beam on the sample. The angle of incidence is determined from the sample-to-screen distance and the distance from the specular reflected beam to the shadow edge of the RHEED pattern at the phosphor screen as shown in Fig. 16. The depth d is the inelastic mean free path of the electrons at the considered energy. The inelastic mean free path is given by the following empirical expression:⁵

$$d = \frac{538}{E^2} + 0.41\sqrt{\alpha E}, \quad (3.1.4)$$

where E is the energy of the electrons and α is the average crystal plane spacing of the solid.

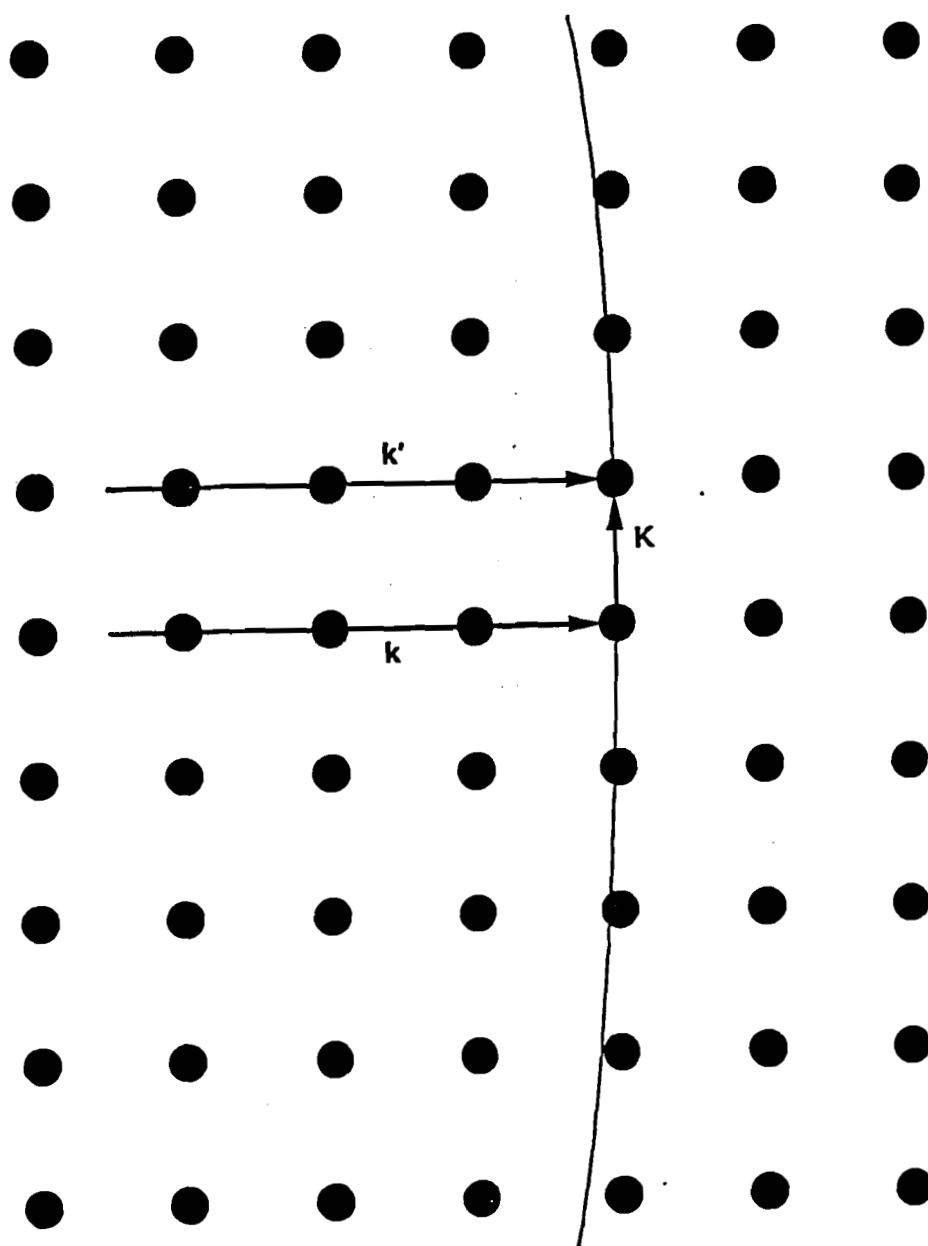


Figure 15. Ewald construction for high energy electrons. In this case the radius of the Ewald sphere is much larger than dimensions in reciprocal space. As a consequence of this, RHEED essentially views cross-sections of reciprocal space.



$$\theta = \tan^{-1} \left(\frac{d}{L} \right)$$

Where **d = distance from the specular spot to the shadow edge**
L = sample-to-screen distance

Figure 16. Photograph of a RHEED pattern from Pb(111). The distance from the specular reflected beam and the shadow edge is used along with the sample-to-screen distance to determine the angle of incidence of the electron beam on the surface.

The parameter α is given by the relation

$$\alpha = \left(\frac{W}{\rho} \right)^{1/3}, \quad (3.1.5)$$

where W is the atomic weight and ρ is the density of the solid. For Pb, $\alpha = 3.11 \text{ \AA}$. A plot of the electron inelastic mean free path in Pb is given in Fig. 17. The resulting probed depth, d_p , in the RHEED geometry is typically in the range of 1 - 10 \AA . Since the RHEED streaks represent only one section of the reciprocal lattice of the crystal, it is necessary to obtain RHEED patterns at several azimuthal angles to obtain a complete characterization of the surface structure. An example of this characterization is shown in Fig. 18 for Pb(110), where photographs of RHEED patterns were taken at various azimuthal positions of the crystal.

As a surface structural probe, RHEED has many advantages over other types of probes.² The strong forward scattering of electrons in RHEED makes detection more straightforward as compared with the relatively isotropic scattering of x-rays. In addition, the differential scattering cross sections of RHEED are approximately 10^8 higher than those of x-ray diffraction, reflecting the much stronger interaction of electrons with solids. A diagram of the differential scattering cross sections for various probes is given in Fig. 19. Detection in LEED, another popular surface probe, also tends to be more involved than in RHEED due to the larger solid angle into which the diffracted electrons are scattered, and the need for retarding grids in proximity to the phosphor screen to stop inelastically scattered electrons. The sensitivity of RHEED is comparable to that of LEED with the advantage that the probed depth can be varied by changing the angle of incidence of the electron beam on the surface rather than changing

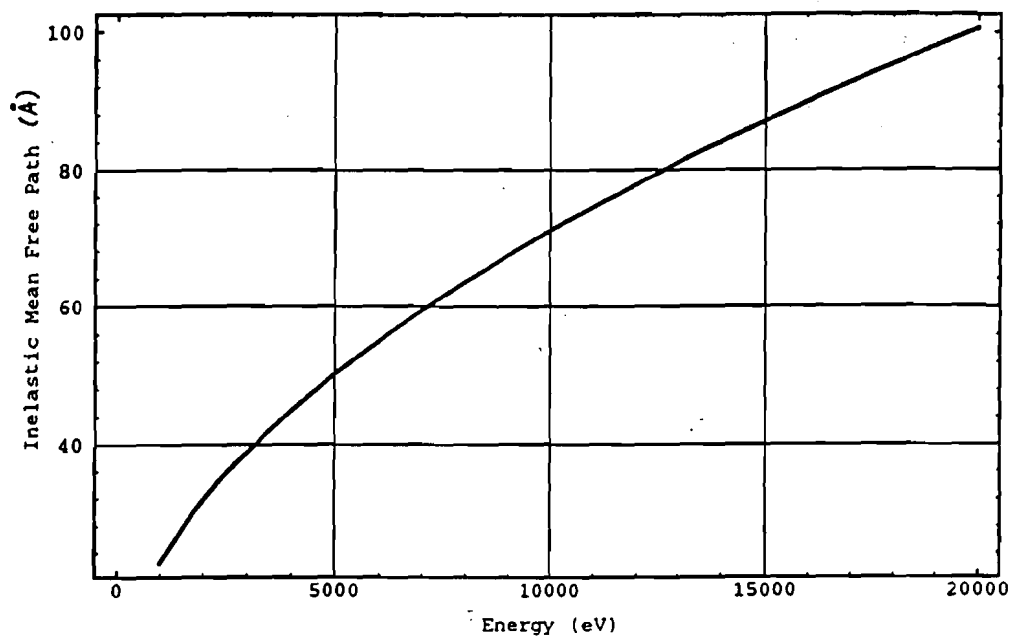


Figure 17. The inelastic mean free path of electrons in Pb. For an electron energy of 15 keV, typical in RHEED, the inelastic mean free path in Pb is approximately 90 Å.

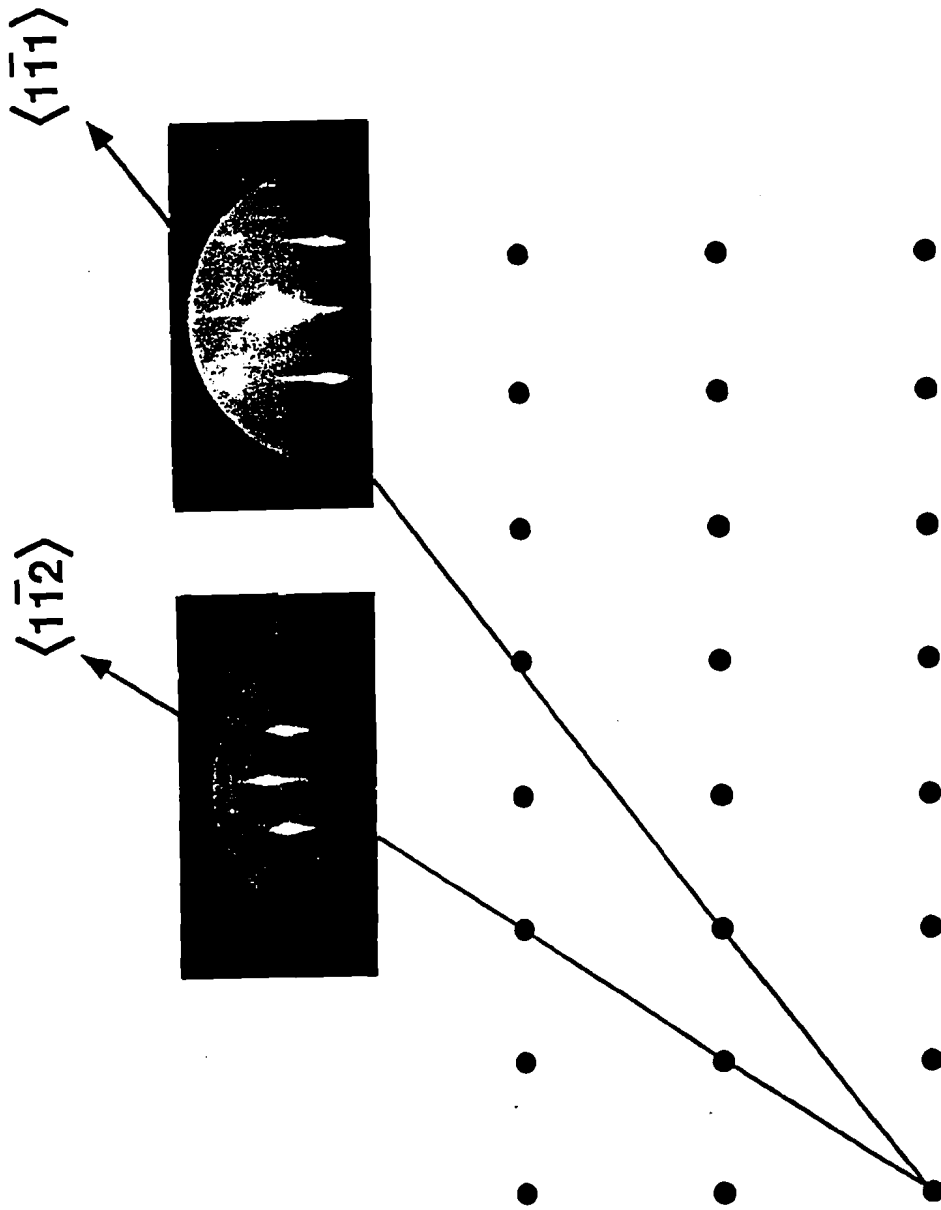


Figure 18. A series of photographs of the RHEED pattern of Pb(110) taken at various azimuthal orientations.

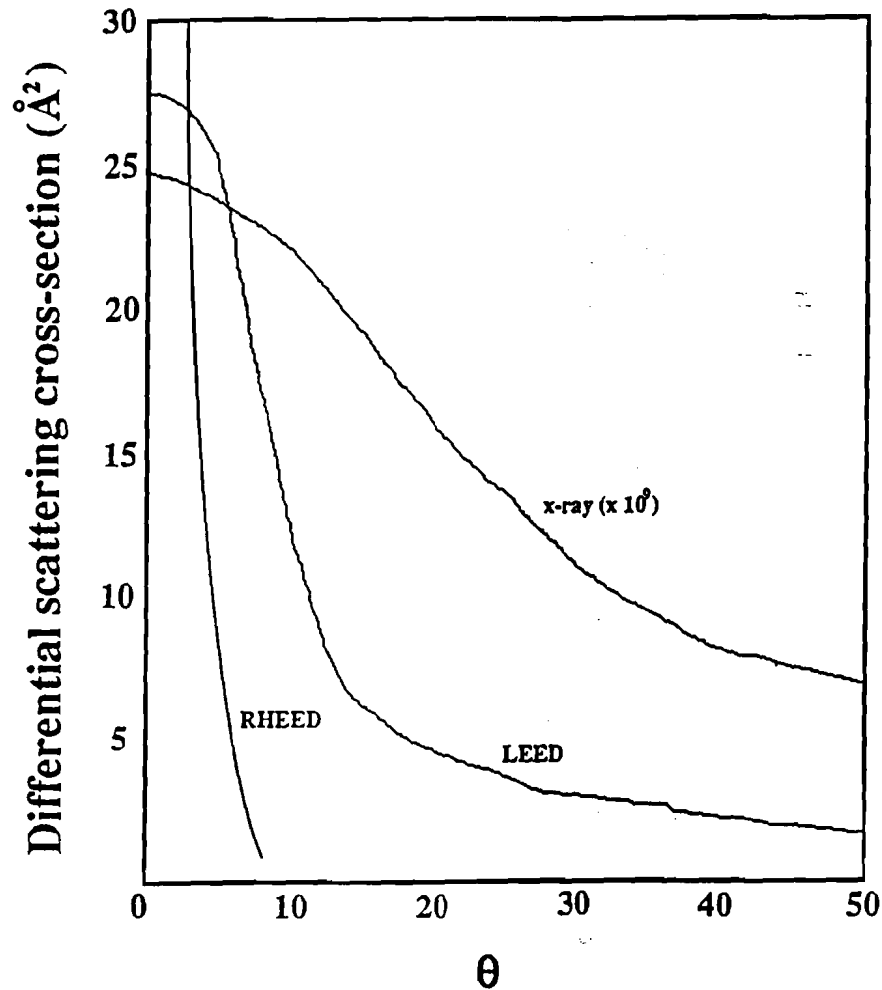
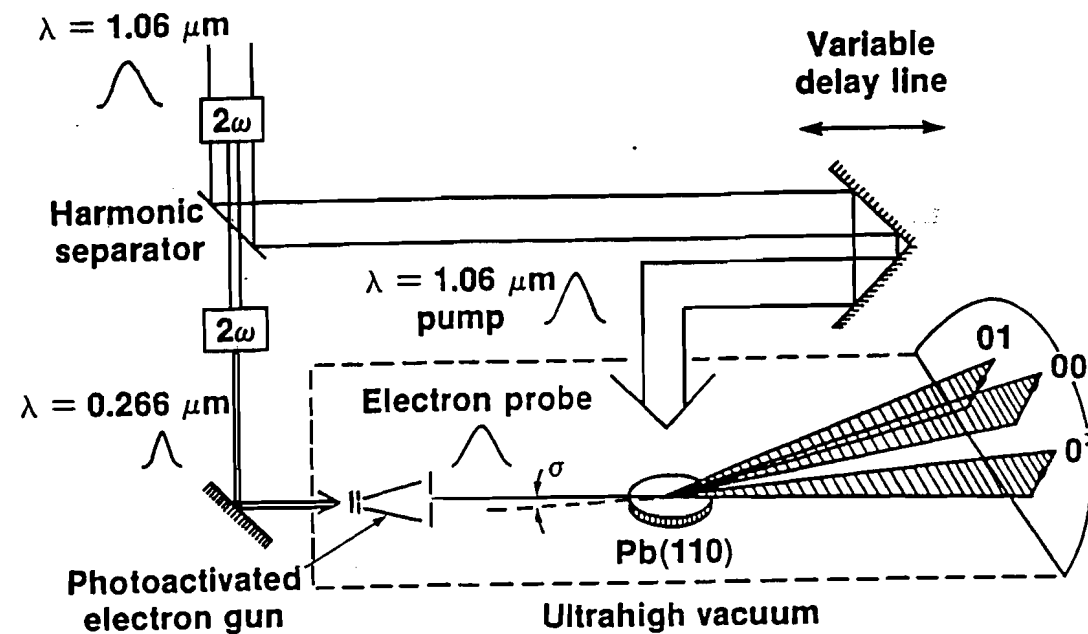


Figure 19 Differential scattering cross section for various structural probes. X-ray scattering in solids has a low differential scattering cross section due to the weak interaction of photons with solids. The sensitivity of RHEED is comparable to that of low-energy electron diffraction (LEED) with the advantage that the scattering is significantly less isotropic.

the primary electron energy, as is the case with LEED. Finally, for the production of short electron pulses necessary for ultrafast time-resolution, the high electric fields associated with a RHEED system are much more effective in compensating for space-charge effects. Space-charge effects, which result from the mutual repulsion of electrons, tend to temporally broaden the pulse of electrons.

3.2 TIME-RESOLVED RHEED: EXPERIMENTAL TECHNIQUE

To the present, the experimental and theoretical work on surface melting has provided much static, equilibrium information on the process. In the work presented here, time-resolved RHEED is used to study the *dynamic* structural behavior of surfaces. The technique of time-resolved RHEED will be briefly described in this section. A more detailed description may be found elsewhere.⁶ A diagram of the experimental set-up is given in Fig. 20. The output of a CW-pumped Nd:YAG regenerative amplifier laser ($\lambda = 1.06 \mu\text{m}$, pulse width $\tau_p \sim 200 \text{ ps}$ FWHM) is split into two beams. The first beam is amplified in a double-pass Nd:YAG amplifier and serves as the transient heating source. The heating pulse passes through an optical delay line and strikes the surface of the studied sample at near-normal incidence. The second beam is frequency quadrupled and strikes the cathode of a photoactivated electron gun, photoelectrically producing pulses of electrons. The electrons are accelerated to energies in the 15 - 20 keV range and probe the surface at a set delay time relative to the arrival of the heating laser pulse. The electron beam interacts with the studied crystal in the glancing incidence RHEED geometry, probing the first several atomic layers. The electron pulses produce diffraction patterns that are ultrafast, time-resolved "snapshots" of the surface temperature and structure. The optical delay line provides the means by which the laser heating pulse and the electron probe pulse are



Z853

Figure 20. Time-resolved reflection high-energy electron diffraction (RHEED). The laser heating pulse (pump) and the electron probe pulse are synchronized. An optical delay line sets the timing between the pump and the probe.

temporally synchronized on the surface. Since the heating laser pulse and the electron probe pulse originate from the same source, the system is inherently free from the timing jitter that is associated with electronically synchronized experiments.

Each electron pulse typically contains 10^5 - 10^6 electrons. The electron pulse temporally broadens with increasing incident UV intensity, due to space-charge effects from increased electron production.⁶ A trade-off exists between a large electron signal and temporally broadened electron pulses. Since the time resolution of the experiment is determined by the electron pulse width, it is desirable to maintain this temporal width as short as is experimentally feasible. Typically, the electron pulse width is comparable to the pulse width of the fundamental laser.

A schematic of the photoactivated electron gun is shown in Fig. 21. The photocathode consists of a thin film of polycrystalline Au that is deposited on a sapphire substrate. The film thickness is typically 200 Å. The work function of Au is 4.68 eV, approximately the energy of the ultraviolet photons used to strike the photocathode. A 500 μm extraction pinhole is located about one millimeter above the photocathode. The potential difference between the photocathode electrode and the pinhole provides a strong electric field which serves to extract the electrons and reduce space-charge broadening of the electron pulse. The resulting extracted electrons are collimated to a size of ~ 300 μm by a focusing electrode. Two orthogonal sets of deflection plates serve to direct the electron beam to the sample.

The sample and the electron gun are located in an ultrahigh vacuum chamber with a base pressure in the low 10^{-10} range. A schematic diagram of the vacuum chamber is shown in Fig. 22. The chamber is equipped with a 5-axis sample manipulator, an ion sputter gun for surface cleaning, and an Auger electron spectrometer for the detection of surface contaminants. The Pb samples used in this

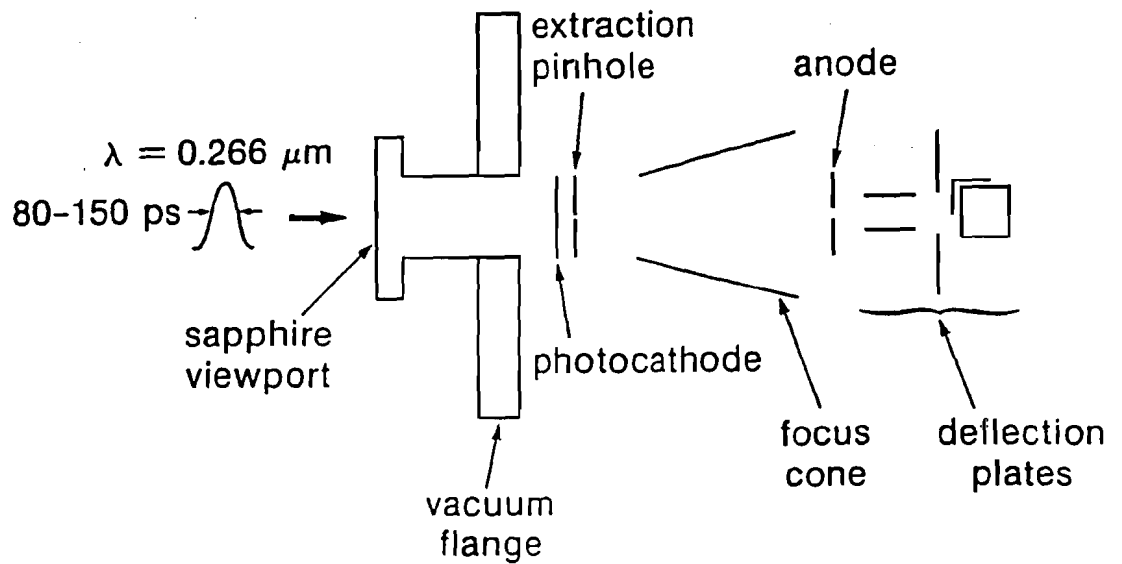


Figure 21. Schematic diagram of the photoactivated electron gun. The photocathode consists of a thin film ($\sim 200 \text{ \AA}$) of polycrystalline Au deposited on a sapphire substrate.

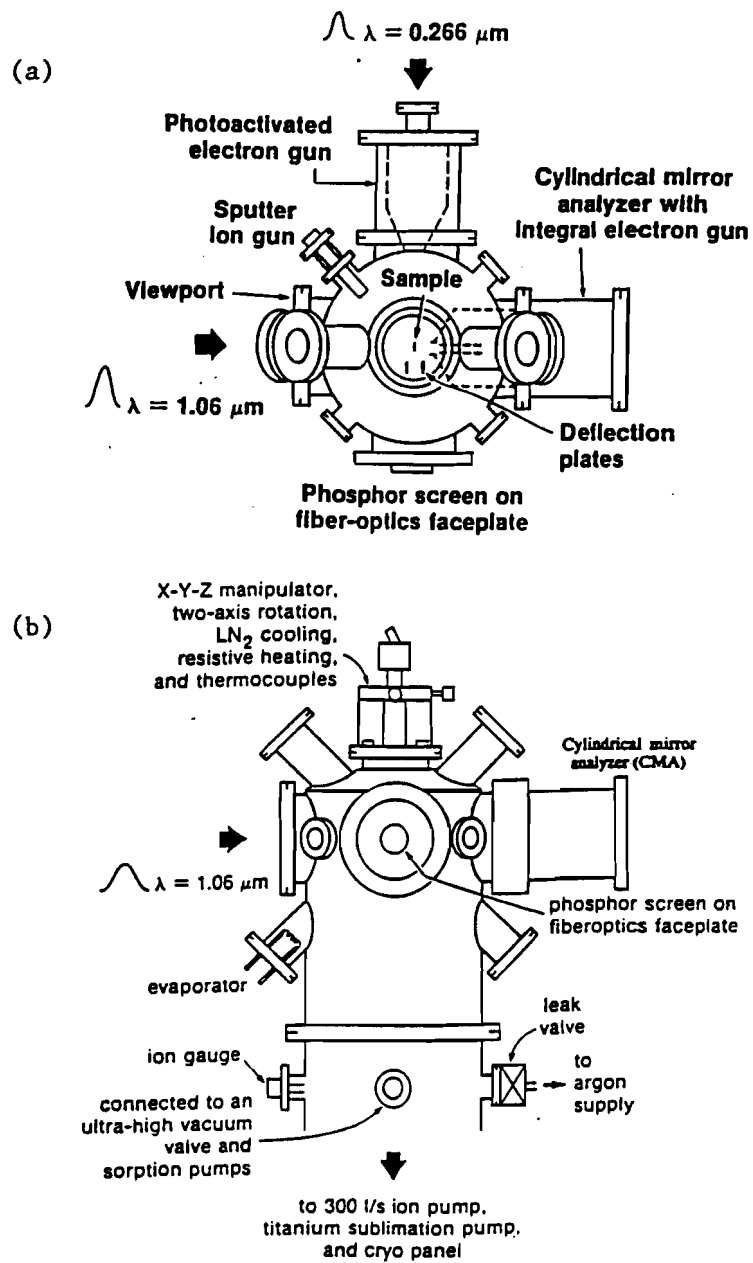


Figure 22. Schematic diagram of the ultrahigh vacuum chamber: (a) top view and (b) side view.

study were cut from a single crystal rod aligned to within 0.75° of the appropriate orientation using Laue back reflection. The surfaces were mechanically polished prior to chemical etching in a solution of 80% glacial acetic acid and 20% hydrogen peroxide (30% in water). The samples were clipped to a resistively heated stage with a Mo base. A thermocouple was placed between a retaining clip and the surface of the sample. The thermocouple was calibrated to the freezing and boiling points of water and to the melting point of Pb.

The samples were cleaned before each experiment with cycles of Ar^+ bombardment followed by annealing. The cleanliness of the surfaces was checked by Auger electron spectroscopy (AES) with a cylindrical mirror analyzer. A description of AES is given in Appendix B. An Auger spectrum of the clean Pb surface is shown in Fig. 23. Auger spectra were taken at an elevated temperature to insure that no high-temperature surface impurity segregation was occurring. Such impurity segregation at the surface could lead to a lowering of the bulk melting temperature, which is not related to the phenomenon of surface melting.

3.3 TIME-RESOLVED RHEED AS A SURFACE-LATTICE TEMPERATURE PROBE⁷

The transformation of incident laser energy to thermal energy of a metal is a multistep process. The steps involved in this process are illustrated in Fig. 24. The first event to occur is the interaction of the valence electrons of the metal with the electric field of the laser, which oscillates with a frequency on the order of 10^{14} Hz. The valence electrons respond much more readily than the lattice atoms since the mass of a lattice atom exceeds the mass of an electron by a factor of $\sim 10^5$. Valence electrons that oscillate in the electric field of the incident laser may reradiate the light and emit

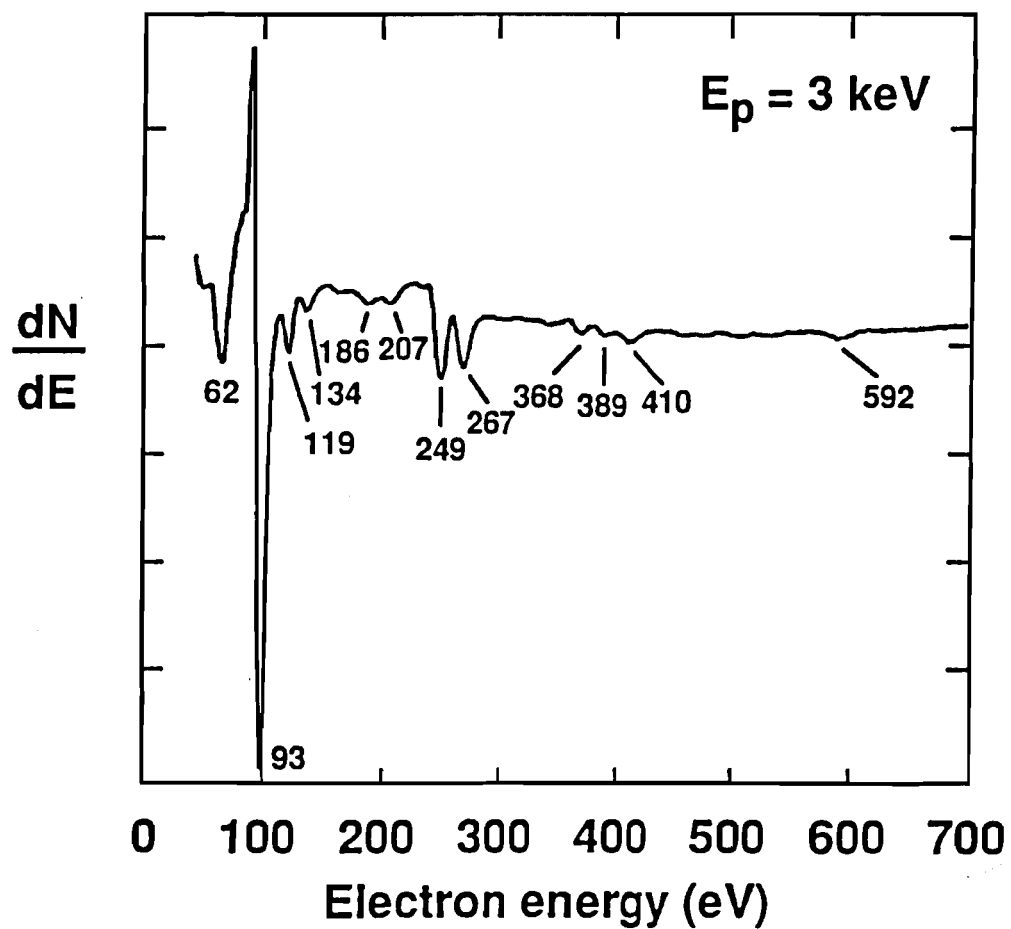


Figure 23. Auger spectrum of a Pb surface after Ar^+ sputtering. The Pb Auger peaks are labeled. The energy of the primary electron beam is 3 keV.

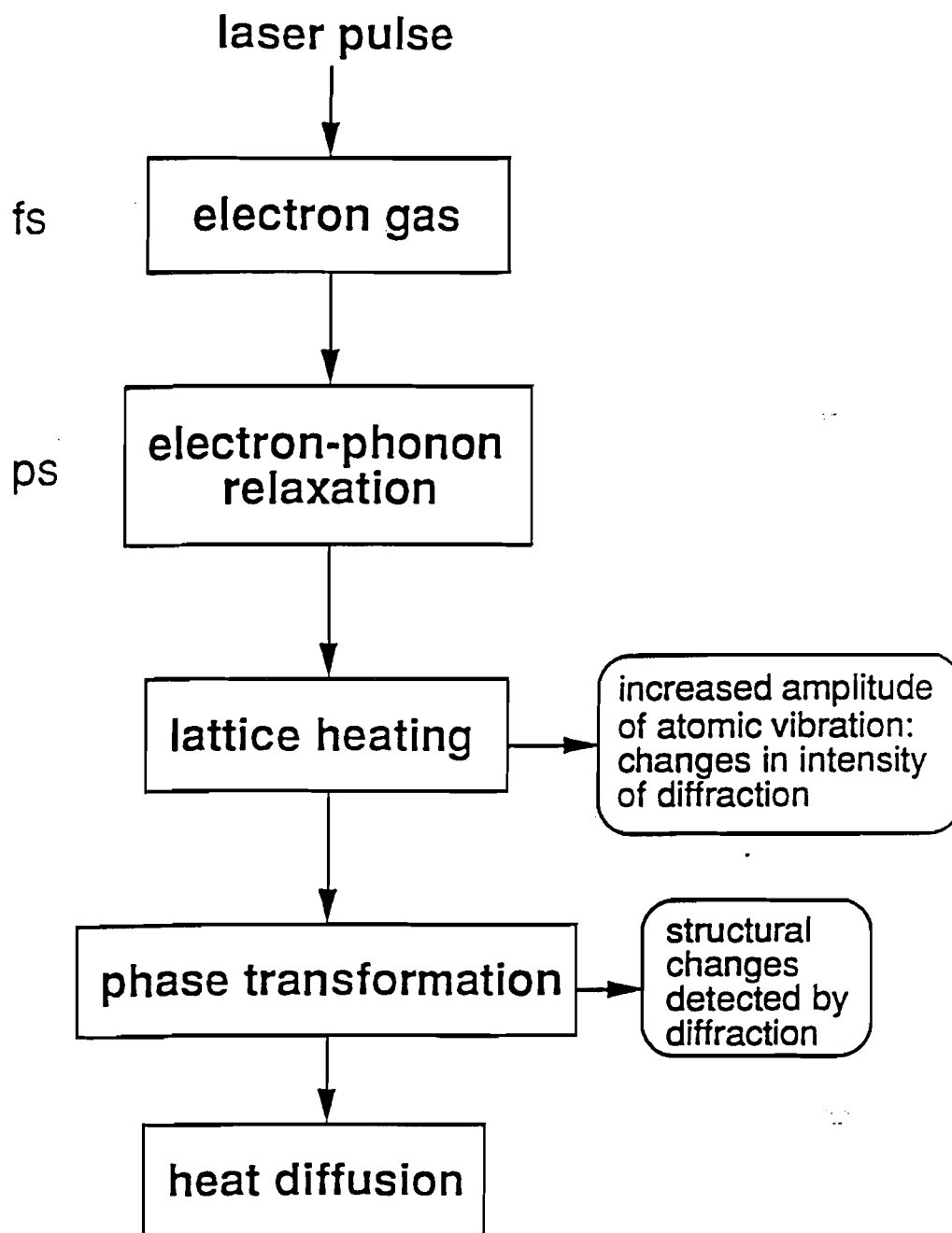


Figure 24. The process of laser-metal interaction.

photons of the same wavelength as the incoming radiation. This results in reflectivity losses. The interaction of the absorbed incoming radiation with the valence electrons results in a hot electron gas that thermalizes with itself on a time scale on the order of 500 fs.⁸ For a period of time subsequent to the electron-electron thermalization, a transient nonequilibrium situation exists whereby a hot electron gas coexists with a cold lattice. This is manifested as a change in the optical properties of the solid. The hot electron gas equilibrates with the lattice on a time scale of a few picoseconds in metals, resulting in the production of phonons.⁹⁻¹¹ Subsequent to the hot electron thermalization with the lattice, heat diffusion occurs.

Several experimental methods have been used to time-resolve the laser-induced temperature rise on surfaces. Some of these include (i) optical techniques such as transient reflectivity and transmissivity,¹² surface second-harmonic generation,¹³ and Raman scattering,¹⁴ (ii) x-ray diffraction,¹⁵ and (iii) photoconductivity measurements.¹⁶ The majority of these probes suffer from the fact that they are not sensitive to the first several atomic layers. This is evident from the optical experiments where the sensitivity is limited by the skin depth of the probe beam, which can be as much as 150 Å. As probes of surface temperature, Raman scattering and x-ray diffraction have the disadvantage that they relate changes in optical and elastic properties to the surface-temperature rise. Therefore, the accuracy of these surface-temperature measurements is limited by the considerable uncertainties in the temperature dependence of these material properties. As compared with the above-mentioned techniques, electron diffraction has the advantages of surface sensitivity and direct temperature measurement. In electron diffraction, the diffraction intensity depends on the atomic mean-square vibrational amplitude, which is the relevant quantity in the definition of temperature. Thus, examining the time evolution of the diffraction intensity from a surface yields information on the surface temperature. Previously,

electron diffraction measurements were performed on free-standing thin films of Au in which the laser-induced temperature rise was deduced.¹⁷

In electron or x-ray diffraction, the Debye-Waller effect describes the reduction in elastic diffraction intensity with increasing lattice temperature.¹⁸ Qualitatively, the reduction in diffraction intensity with temperature results from the increased vibrational amplitude of atoms. As the temperature of a material is raised, the probability of inelastic electron scattering increases due to the increased phonon population. The inelastically scattered electrons contribute to the background of the diffraction pattern. The following expression quantifies this idea:

$$I = I_0 \exp(-WT), \quad (3.3.1)$$

where I is the diffraction intensity at a temperature T , I_0 is the diffraction intensity from the crystal at $T = 0$ K, and $-WT$ is the known as the Debye-Waller factor.

The Debye-Waller relation (3.3.1) assumes a crystal that is cubic and monatomic and does not account for the effects of dynamical scattering on the diffraction intensity.¹⁹ Such effects result from multiple scattering of the electrons in the crystal. In addition, the above relation assumes that the atomic vibrations can be treated according to the harmonic approximation. Anharmonic terms in the crystal potential become apparent at high temperatures and at surfaces, where atoms experience an enhanced vibrational amplitude as a result of asymmetric bonding. When Eq. (3.3.1) is used in conjunction with diffraction measurements from surfaces, an effective surface Debye temperature is obtained which is significantly lower than the bulk value.²⁰ This is due to the enhanced vibrational amplitude of surface atoms. A description of how RHEED is used to determine the Debye temperature of surfaces is given in Appendix A.

By utilizing the Debye-Waller effect, time-resolved RHEED was used as an ultrafast surface-temperature probe.⁷ The first step in this experiment involved performing a measurement of the RHEED streak intensity versus sample temperature. Static RHEED measurements are an important component of the experiment as they yield equilibrium surface structural information and also serve as a means to convert the time-resolved diffraction intensity to a surface-temperature rise. In this mode of operation, a Hg lamp, or the frequency-quadrupled output of the regenerative amplifier operating at 1 kHz repetition rate, is used to excite the cathode of the photoactivated electron gun, producing a steady electron beam. The diffracted electrons from the surface are detected by a microchannel plate (MCP) detector proximity focused to a phosphor screen. The resulting image is lens-coupled to a linear array camera for intensity analysis. The linear array camera is positioned so as to obtain a line scan through the center of the considered RHEED streak and perpendicular to it. For all of the experiments here, the intensity of the (10) diffraction streak was measured. This measurement, shown for Pb(111) is given in Fig. 25.²¹ The results of this measurement are used as a calibration for the time-resolved data, providing a correlation between a given RHEED streak intensity and surface temperature. The data exhibit the exponential Debye-Waller decay of the streak intensity.

We next performed time-resolved heating experiments in which the normalized RHEED streak intensity was obtained for given delay times between the laser heating pulse and the electron probe pulse. For the time-resolved experiments, the system is operated at a repetition rate of 8-15 Hz with the laser providing a maximum energy of 15-20 mJ per pulse to the surface of the sample. A more detailed description of the regenerative amplifier laser system is given in Appendix C. For the collection of the time-resolved data, a shot-to-shot normalization scheme is employed to compensate for

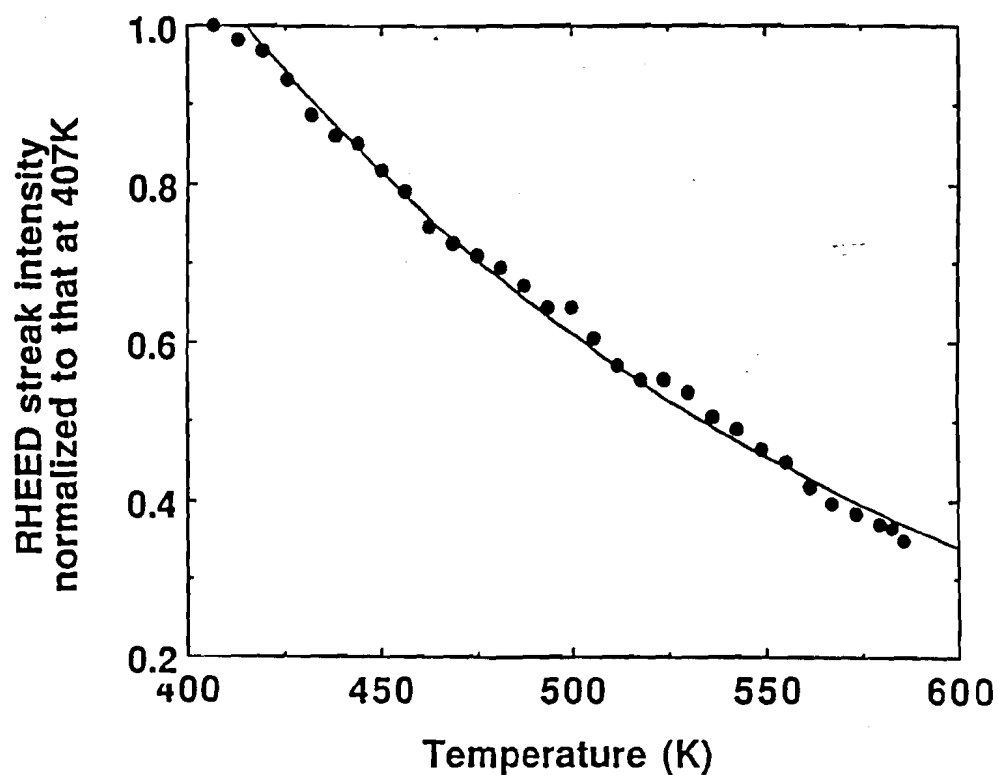


Figure 25. RHEED streak intensity, normalized to that at 407 K, versus sample temperature for Pb(111). The orientation of the crystal was the same as that for the pulsed laser heating experiments. The solid line is an exponential fit to the data showing good agreement to the Debye-Waller attenuation of the diffraction intensity with increasing temperature. These data are used to associate a given diffraction intensity with a surface temperature.

fluctuations in the heating laser beam. A mechanical shutter is inserted in the path of the heating laser which allows every other pulse (at 8 Hz repetition rate) or every other two pulses (at 15 Hz repetition rate) to interact with the sample. For a given heating laser fluence and delay time between the laser heating pulse and the electron probe pulse, scans are obtained with and without laser heating. The diffraction patterns corresponding to these two states are detected by an optical multichannel analyzer and averaged in two separate memories of the computer. This is illustrated in Fig. 26. The RHEED streak intensity analysis consists of obtaining the ratio of the background-subtracted peaks of the unheated and the heated scans for the considered delay positions. Fig. 27 shows the transient modulation of the streak intensity with time. In the example shown, the sample was biased at a temperature of 495 K and subjected to laser pulses with a peak intensity of $2.8 \times 10^7 \text{ W/cm}^2$. The time-resolved streak intensity is observed to rapidly decrease with the arrival of the heating laser pulse. Subsequent to this fast decay in streak intensity, a rapid increase is observed which is a result of the rapid cooling of the surface due to heat conduction to the bulk of the crystal. Coupling the fact that the electrons typically probe a depth of $< 5 \text{ \AA}$ with the much larger absorption depth of the laser into the sample (140 \AA for Pb at $\lambda = 1.06 \text{ \mu m}$), we conclude that, upon laser heating, the layer that the electrons probe is isothermal to a first approximation.

The modulation of the streak intensity due to pulsed laser heating is related to a surface-temperature rise using the results of the static equilibrium RHEED measurement of Fig. 25. This conversion is valid if (i) the time scale of the measurement is longer than that necessary for equilibrium to be established between the electrons and the lattice, (In metals, this typically occurs within a few picoseconds, a time scale much shorter than the 200 ps resolution of the experiments presented here.) (ii) no surface

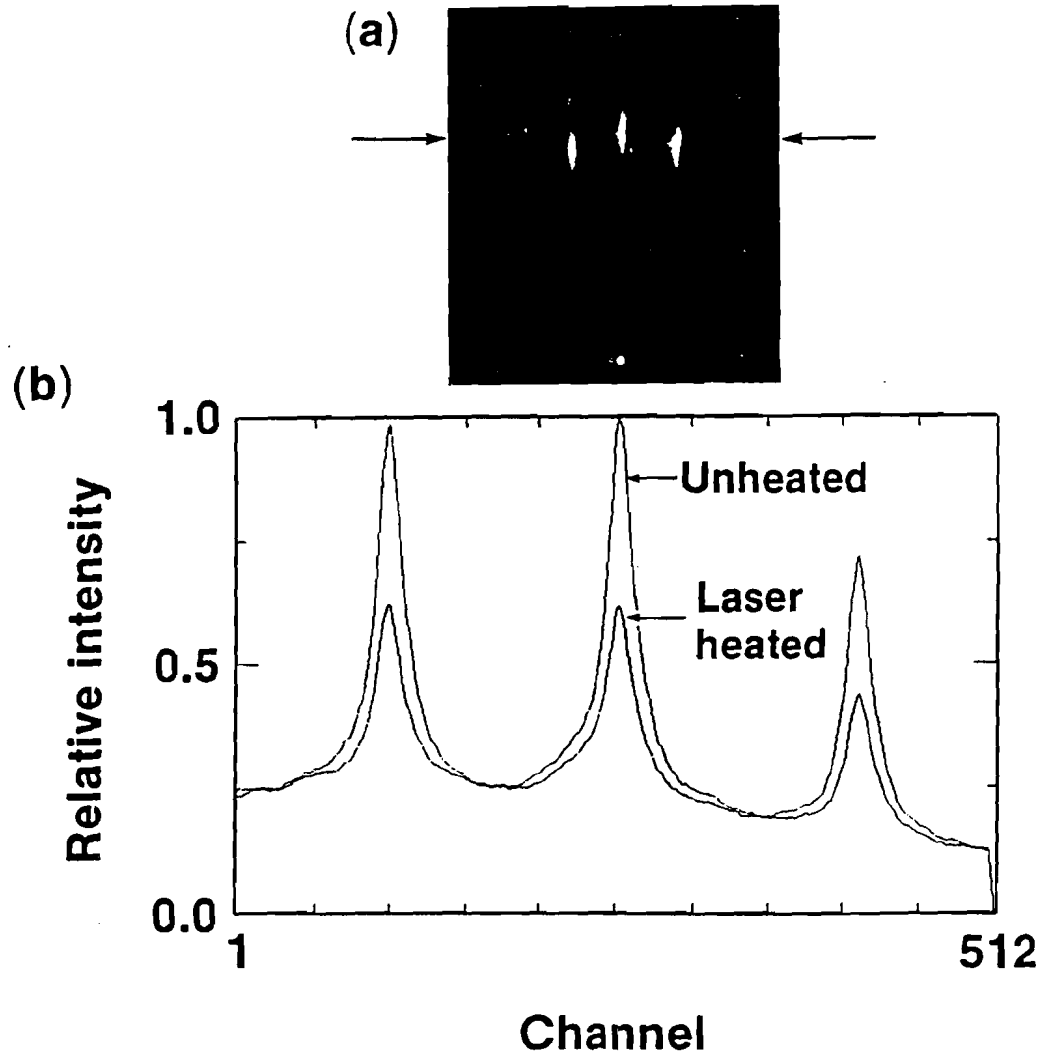


Figure 26. Line scans through the diffraction pattern for an unheated surface and a laser-heated surface. A shutter is placed in the path of the heating laser which allows every other heating pulse to interact with the sample. The computer sorts heated and unheated scans in separate memories and performs averages of these scans. The attenuation of the diffraction intensity due to laser heating is evident.

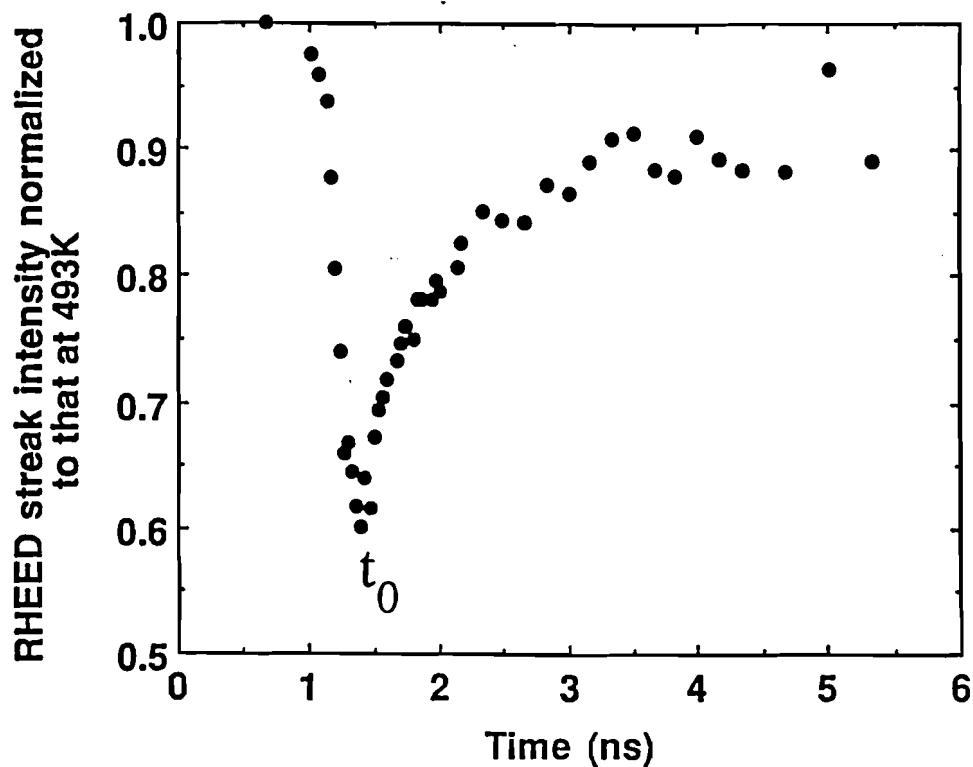


Figure 27. Time-resolved modulation of the RHEED streak intensity of Pb(111) subjected to ~ 200 ps (FWHM) laser pulses with peak intensity of $I_p \sim 3.0 \times 10^7$ W/cm². The diffraction intensity decreases rapidly upon the arrival of the laser pulse and subsequently increases as the surface cools by heat conduction into the bulk of the crystal. The data of Fig. 25 are used to convert the diffraction intensity modulation to a surface-temperature rise.

phase transformation occurs, and (iii) no accumulated surface modifications occur with laser heating. These conditions are fulfilled for these experiments.

The experimentally determined surface-temperature rise is compared with the solid line in Fig. 28, obtained from a one-dimensional heat diffusion model:

$$C \frac{dT(z,t)}{dt} = K \frac{d^2T(z,t)}{dz^2} + I_p (1-R) \alpha e^{-\alpha z} f(t) \quad (3.3.2)$$

where $T(z,t)$ is the temperature at a distance z normal to the sample surface ($z = 0$), t is time, $f(t)$ is the temporal profile of the laser pulse which is assumed to be Gaussian, and the other model parameters are listed in Table 2. The following further simplifying assumptions were made in solving the heat diffusion model: (i) the thermal constants of the metal were assumed to be independent of temperature and (ii) the peak laser intensity, I_p , was taken as constant. The second assumption is approximated experimentally by spatially expanding the heating laser beam on the sample.

The peak laser intensity is determined by the following relation:

$$I_p = \frac{P\rho}{f\tau A} \gamma, \quad (3.3.3)$$

where P is the average power of the heating laser beam, ρ is the ratio of the beam energy that passes through a rectangular slit placed at the target-equivalent-plane, γ is a factor of order unity that accounts for the Gaussian temporal profile of the laser pulse and the loss of beam energy through the vacuum chamber window, f is the repetition rate of the laser, τ is the temporal width of the laser pulse as determined by an autocorrelation of the beam, and A is the area of the slit. The dimensions of the slit approximate the area that is probed on the surface by the electron beam.

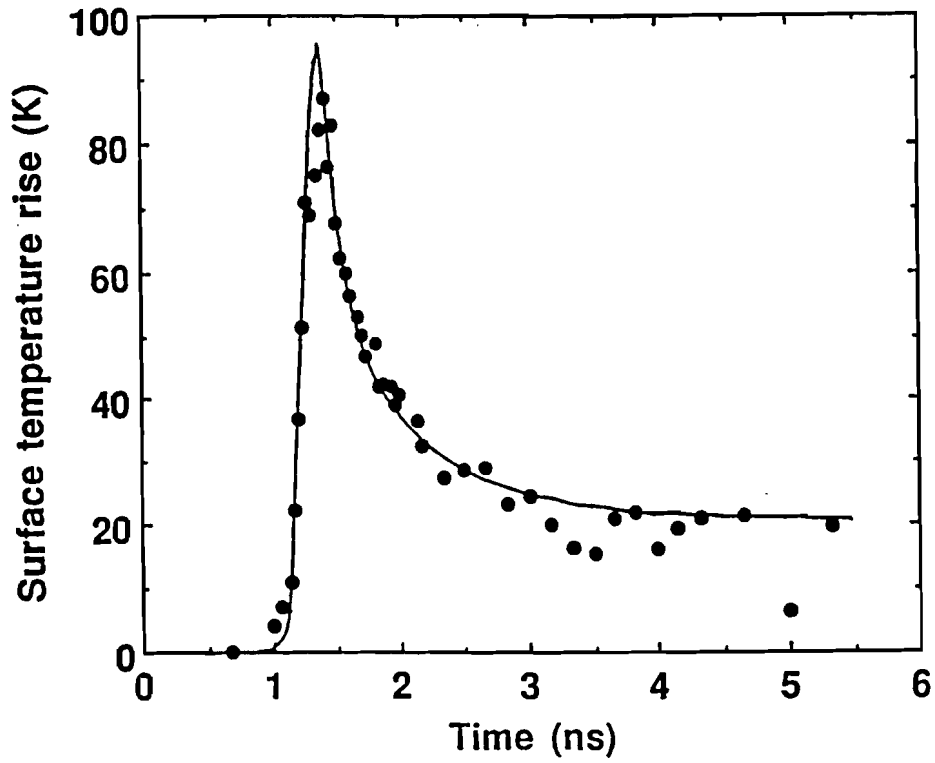


Figure 28. Surface-temperature rise induced on Pb(111). These data are the result of the conversion of the data of Fig. 27 to surface temperature through Fig. 25. The solid line is a solution of the heat diffusion model for the parameters of the experiment.

Table 2 Parameters for time-resolved heating experiment

C	Heat capacity per unit volume ⁽¹⁾	$1.58 \times 10^6 \text{ J/m}^3\text{K}$
K	Thermal conductivity ⁽¹⁾	32.2 W/mK
α	Absorption coefficient ⁽²⁾	$7.06 \times 10^7 \text{ m}^{-1}$
I_p	Peak laser intensity	$3.0 \times 10^7 \text{ W/cm}^2$
R	Reflectivity at $\lambda = 1.06 \text{ }\mu\text{m}$ and $T = 493 \text{ K}$	0.79

⁽¹⁾Thermophysical Properties of Matter, edited by Y. S. Toukougian (Plenum, New York, 1970), Vols. 1 and 4.

⁽²⁾From $\alpha = 4\pi k/\lambda$, where k is the imaginary part of the complex index of refraction. The values of k were obtained from an interpolation of the data in A. I. Golovashkin and G. P. Moltulevich, Zh. Eksp. Teor. Fiz. 53, 1526 (1967) [Sov. Phys. JETP 26, 881 (1968)].

Further experiments were performed to compare the time-resolved results to that predicted from the one-dimensional heat diffusion model. In Fig. 29 Pb(110) was subjected to varying laser fluences at the time t_0 , corresponding to the minimum of the time-resolved RHEED streak intensity (see Fig. 27), and the time $t_0 + 500$ ps. The resulting diffraction intensity modulations were converted to a surface-temperature rise, ΔT , using a static RHEED intensity calibration similar to Fig. 25. The solid lines were obtained from a solution of the heat diffusion model. It is seen that the experimental surface-temperature rise reflects the linear increase with peak laser intensity that is predicted from Eq. 3.3.3.

Our time-resolved measurements are the result of the convolution of the electron probe pulse with the temporal profile of the surface temperature. This convolution is the result of the finite width of the electron probe pulse, and tends to be most prominent near the time t_0 , where the rate of change of temperature with time is greatest. Convolution effects tend to displace and depress the experimentally-determined peak surface-temperature rise by averaging the surface temperature over the temporal duration of the probe pulse. This is evident in Fig. 30 where the time-resolved surface-temperature rise on Pb(110) is plotted. In the inset, the data is plotted on a smaller time scale and the effects of convolution are evident.

In order to estimate the effect of convolution on the time-resolved surface-temperature measurements, solutions to the heat diffusion model were examined. The ratio $\Delta T_{\text{peak}}/\Delta T_{\text{avg}}$ was obtained from the results of the heat diffusion model. Here, ΔT_{peak} is the peak surface-temperature rise and ΔT_{avg} is the temperature rise averaged over a given electron pulse width, τ_{electron} . The ratio $\Delta T_{\text{peak}}/\Delta T_{\text{avg}}$ is plotted in Fig. 31 for various model parameters. Taking $\tau_{\text{electron}} \approx \tau_{\text{laser}}$ (a reasonable assumption if the UV intensity incident on the photocathode of the electron gun is not excessive) a

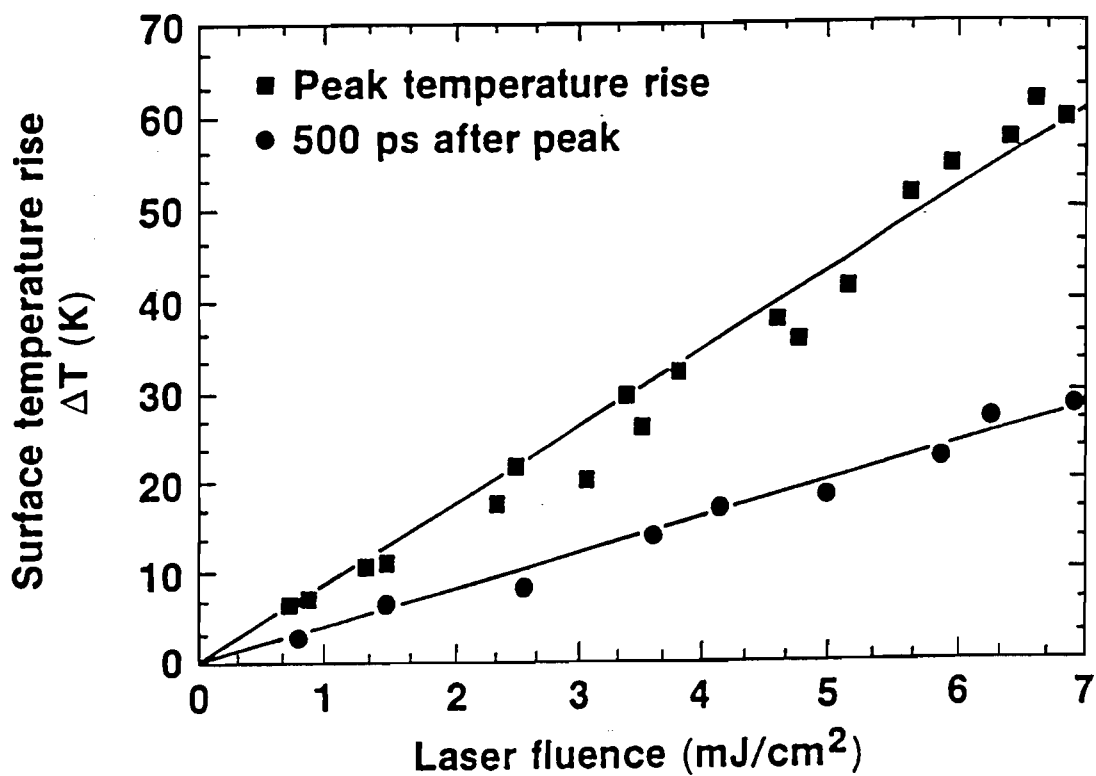


Figure 29. Peak surface-temperature rise ΔT on Pb(110) subjected to various laser fluences. Experiments were carried out at the experimentally-determined peak of the surface-temperature rise, t_0 , and at $t_0 + 500$ ps. ΔT is seen to increase linearly with laser fluence in agreement to the heat diffusion model.

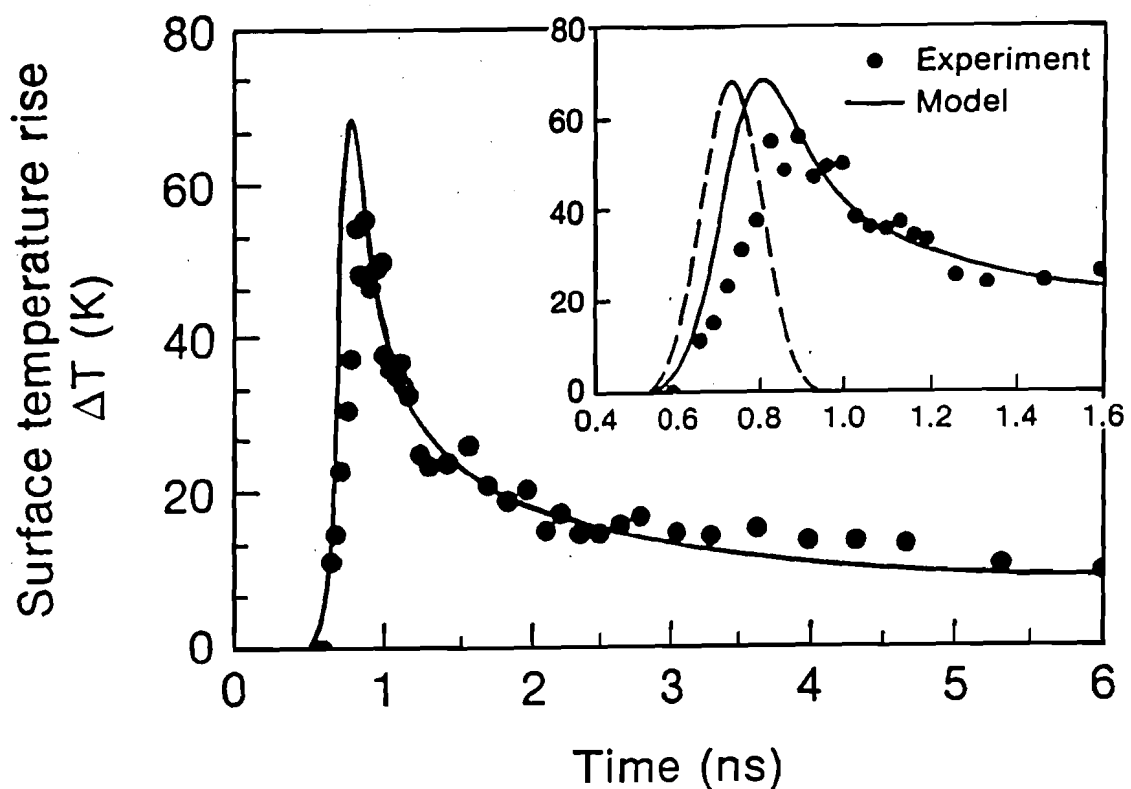


Figure 30. Surface-temperature rise induced on Pb(110) irradiated with $I_p \sim 3.5 \times 10^7$ W/cm², 170 ps (FWHM) laser pulses. The solid line is obtained from a heat diffusion model. The inset is an expanded view near the peak of the surface-temperature rise with the dashed line representing the temporal profile of the laser heating pulse. The effects of convolution are most prominent near the peak of the surface-temperature rise where the rate of change of temperature with time is greatest.

depression of up to 20% in the measured ΔT relative to the peak value predicted from the heat diffusion model is obtained.

Other sources of error in the time-resolved temperature measurement include the nonuniformity of laser heating, the accuracy of the static calibration, and laser stability. Shot-to-shot fluctuations of the laser are compensated for by our shuttered data acquisition technique and the long-term stability of the laser is monitored throughout the experiments and kept to within 10% of the desired value. The absolute timing between the electron probe pulse and the laser heating pulse was not experimentally determined. The temporal position of the experimental temperature profile relative to the results from the model was set by minimizing the mean-square difference between the experimental results and the heat diffusion model subsequent to the maximum surface-temperature rise, where convolution effects are not expected to be significant.

Considering the above factors, we observe general agreement between our time-resolved surface-temperature measurements and that predicted from a one-dimensional heat diffusion model. We conclude from these experiments that time-resolved RHEED is a viable probe of transient events at surfaces. These experiments serve as a motivation for the next set of experiments that explore the time-resolved structural behavior of surfaces.

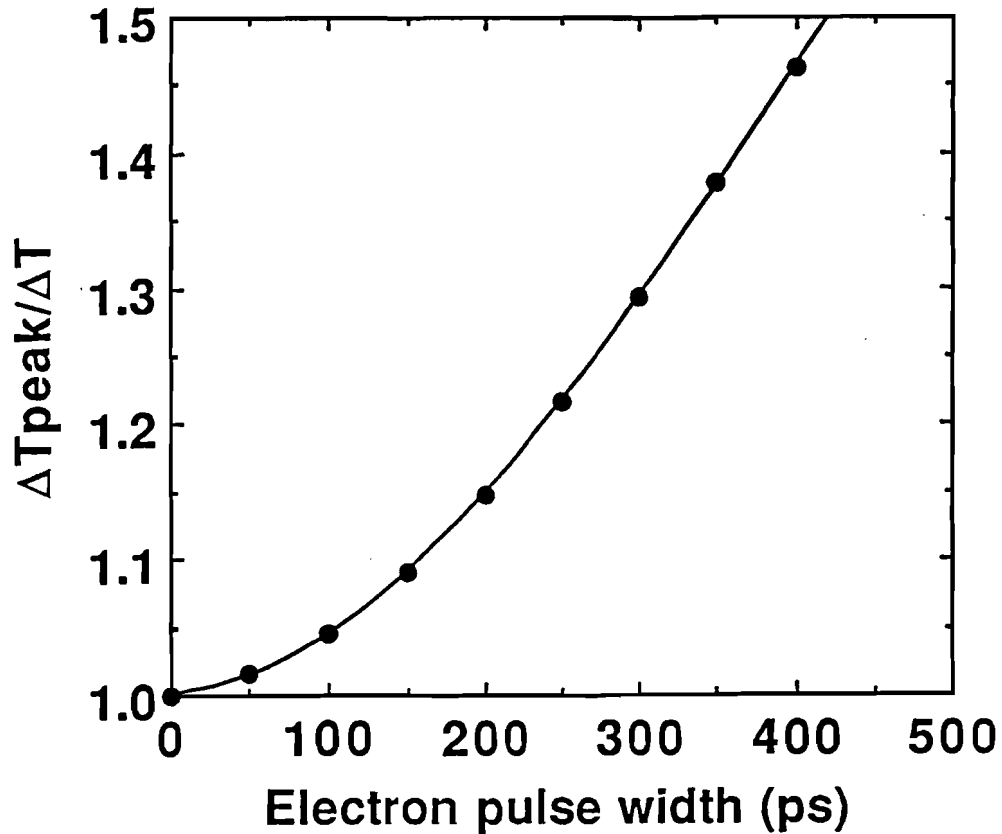


Figure 31. Ratio of the peak ΔT to the ΔT obtained by a temporal average about the surface-temperature peak with various electron pulse widths. These data were obtained by examining solutions to the heat diffusion model assuming laser heating pulses with width of 200 ps. For an electron pulse width comparable to the laser pulse width, a 20% reduction in the observed ΔT relative to the peak ΔT is predicted.

REFERENCES

1. Sh. Nishikawa and S. Kikuchi, Proc. Imp. Acad. Japan **4**, 475 (1928).
2. For a general review of RHEED, see E. Bauer, *Techniques of Metals Research*, Vol. II, Part 2, edited by R. F. Bunshah (Interscience, New York, 1969).
3. J. E. Mahan, K. M. Geib, G. Y. Robinson, and R. G. Long, J. Vac. Sci. Technol. **A 8**, 3692 (1990).
4. M. G. Lagally and D. E. Savage, MRS Bulletin **18**, 24 (1993).
5. M. P. Seah and W. A. Dench, Surface and Interface Analysis **1**, 2 (1979).
6. H. E. Elsayed-Ali and J. W. Herman, Rev. Sci. Instrum. **61**, 1636 (1990).
7. H. E. Elsayed-Ali and J. W. Herman, Appl. Phys. Lett. **57**, 1508 (1990).
8. W. S. Fann, R. Storz, H. W. K. Tom, and J. Bokar, Phys. Rev. Lett. **68**, 2834 (1992).
9. H. E. Elsayed-Ali, T. B. Norris, M. A. Pessot, and G. A. Mourou, Phys. Rev. Lett. **58**, 1212 (1987).
10. R. W. Schoenlien, W. Z. Zin, J. G. Fujimoto, and G. L. Eesley, Phys. Rev. Lett. **58**, 1680 (1987).
11. S. D. Brorson, J. G. Fujimoto, and E. P. Ippen, Phys. Rev. Lett. **59**, 1962 (1987).
12. C. A. Paddock and G. L. Eesley, Appl. Phys. Lett. **60**, 285 (1986).
13. J. M. Hicks, L. E. Urbach, E. W. Plummer, and H. Dai, Phys. Rev. Lett. **61**, 2588 (1988).
14. D. von der Linde and G. Wartmann, Appl. Phys. Lett. **41**, 700 (1982).
15. B. C. Larson, C. W. White, T. S. Noggle, and D. M. Mills, Phys. Rev. Lett. **48**, 337 (1982).
16. P. S. Peercy in *Laser Surface Treatment of Metals*, edited by C. W. Draper and P. Mazzoldi (Martinus Nijhoff, Dordrecht, 1986), p. 611.

17. H. -C. Chen, G. A. Mourou, and R. S. Knox in *Beam-Solid Interactions: Physical Phenomena*, edited by J. A. Knapp, P. Bargesen, and R. A. Zuhr (Materials Research Society, Pittsburgh, PA, 1990), Vol. 157, pp. 437-442.
18. P. Debye, *Ann. Phys.* **43**, 49 (1913); I. Waller, *Z. Phys.* **17**, 398 (1923); *Ann. Phys.* **79**, 261 (1926).
19. W. Glaeser and H. Niedrig, *J. Appl. Phys.* **37**, 4303 (1966); W. W. Albrecht and H. Niedrig, *J. Appl. Phys.* **39**, 3166 (1968).
20. R. M. Goodman, H. H. Farrell, and G. A. Somorjai, *J. Chem. Phys.* **48**, 1046 (1968).
21. J. W. Herman and H. E. Elsayed-Ali, *Phys. Rev. Lett.* **69**, 1228 (1992).

CHAPTER 4: TIME-RESOLVED SURFACE DISORDERING OF Pb(110)*

4.1 INTRODUCTION

In the studies presented here, we investigate the structural behavior of the three low-index faces of Pb using time-resolved RHEED. This work is aimed at determining how the crystal surface influences the temporal dynamics of the melting process. In the past, a number of time-resolved probes have been developed to examine the structure of materials. Some of these include surface second-harmonic generation (SHG),¹ x-ray diffraction,² conductance measurements,³⁻⁴ and transmission electron diffraction.⁵

Second-harmonic generation from materials with inversion symmetry is generally forbidden in the electric dipole approximation.⁶ This symmetry, however, is broken at the surface of a solid and SHG can occur there. The use of surface SHG as a probe of the first several atomic layers is limited, however. It has recently been shown that the expression for the surface SHG intensity in a homogeneous medium cannot be decoupled from a bulk contribution in experimental situations.⁷ In addition, due to the low signal intensity in SHG measurements, it is desirable that the second-harmonic signal be enhanced by an interband transition of comparable energy. This constraint limits the applicability of surface SHG to a few materials.

X-ray diffraction has been used as a time-resolved probe by utilizing x-ray pulses from a synchrotron source.² X-ray pulses of 150 ps duration were used to study the laser-induced temperature distribution, interfacial overheating, undercooling, and crystal regrowth on Si.² Lattice temperatures of the 2 nm probed depth were obtained by relating the thermal expansion-induced strain of the heated surface region, as determined from Bragg profile measurements, to a temperature rise by using the thermal expansion coefficients and elastic constants of Si. A difficulty with this method

* J. W. Herman and H. E. Elsayed-Ali, Phys. Rev. Lett. 68, 2952 (1992).

as a time-resolved structural probe is the uncertainty in the temperature dependence of the thermal expansion coefficients and elastic constants of the studied crystal. Errors in these parameters can lead to significant uncertainties in the measured surface temperature.

It is well known that the conductivity, σ , of a material is dependent upon its phase. Upon melting, the change in the conductivity is typically quite small for metals; however, this change can be as large as a factor of 30 for semiconductors such as Si. This property has been used to study the temporal dynamics of the solid-liquid interface induced by fast laser melting. The velocity of the solid-liquid interface during 30 ns pulsed laser melting of Al was determined by observing the transient conductance of the laser melted metal.³ In addition, supercooling and the nucleation of crystal growth of Si subsequent to laser melting was observed.⁴ The technique of transient conductance is better suited to the study of semiconductors due to the inherently greater change in conductance upon melting. In addition, care must be taken with the interpretation of the experimental results as the transient conductance signal is a complex average of the conductances of the phases present at a given time.

Electron diffraction represents a more direct way of studying time-resolved surface structural phenomena. Electron diffraction combines surface sensitivity with the potential for ultrafast temporal resolution. Furthermore, electrons interact with matter much more strongly than photons. Electron energy and angle of incidence are readily adjusted to alter the depth considered. This is true to a much lesser extent with photon probes where the primary limitation is the skin depth of the light in the studied material. Prior to the work presented here, time-resolved transmission electron diffraction was used to study the structural behavior of thin Al films irradiated with ultrafast laser pulses.⁵ The structure of the thin films was monitored throughout the

pulsed heating process. As a probe of transient events at surfaces, time-resolved RHEED is a logical extension of the previous work.

4.2 ULTRAFAST DISORDERING OF Pb(110)⁸

The first surface considered was Pb(110). Pb(110) has been shown to readily disorder below T_m .⁹ As an initial step to characterize the temperature-dependent structure of Pb(110), measurements of the RHEED streak intensity versus temperature were performed. The energy of the electrons was 18.2 keV and the beam was incident along the $\langle 1\bar{1}2 \rangle$ azimuth at an angle of $\sim 2^\circ$, resulting in a probed depth of approximately 2 monolayers. Photographs were taken of the RHEED pattern as the temperature of the sample was raised. A series of these photographs is shown in Fig. 32. The attenuation of the RHEED streak intensity with temperature is evident. At a temperature of $T \sim 547$ K, over 50 K below T_m , the RHEED streak intensity is observed to vanish into the inelastic background of the diffraction pattern. This lack of elastic diffraction intensity is an indication that the probed surface layer is disordered.

Results of a quantitative measurement are given in Fig. 33, where the RHEED streak intensity was monitored using a linear array camera. The inset is a plot of the data on a semilogarithmic scale. The intensity is seen to decay exponentially from the lowest considered temperature, 487 K, up to a temperature of ~ 520 K. This portion of the data is consistent with the Debye-Waller effect which predicts an exponential decay of elastic diffraction intensity with temperature. Above 520 K ($\sim T_m - 80$ K), the intensity is seen to deviate from Debye-Waller behavior. This deviation is initially due to the anharmonic surface vibrations on Pb(110) that have been deduced from measurements of the surface expansion.¹⁰ At higher temperatures, the deviation is attributed to surface disordering. Above $T_d \sim 540$ K, the RHEED signal decayed into the background of inelastically scattered electrons indicating that the probed surface

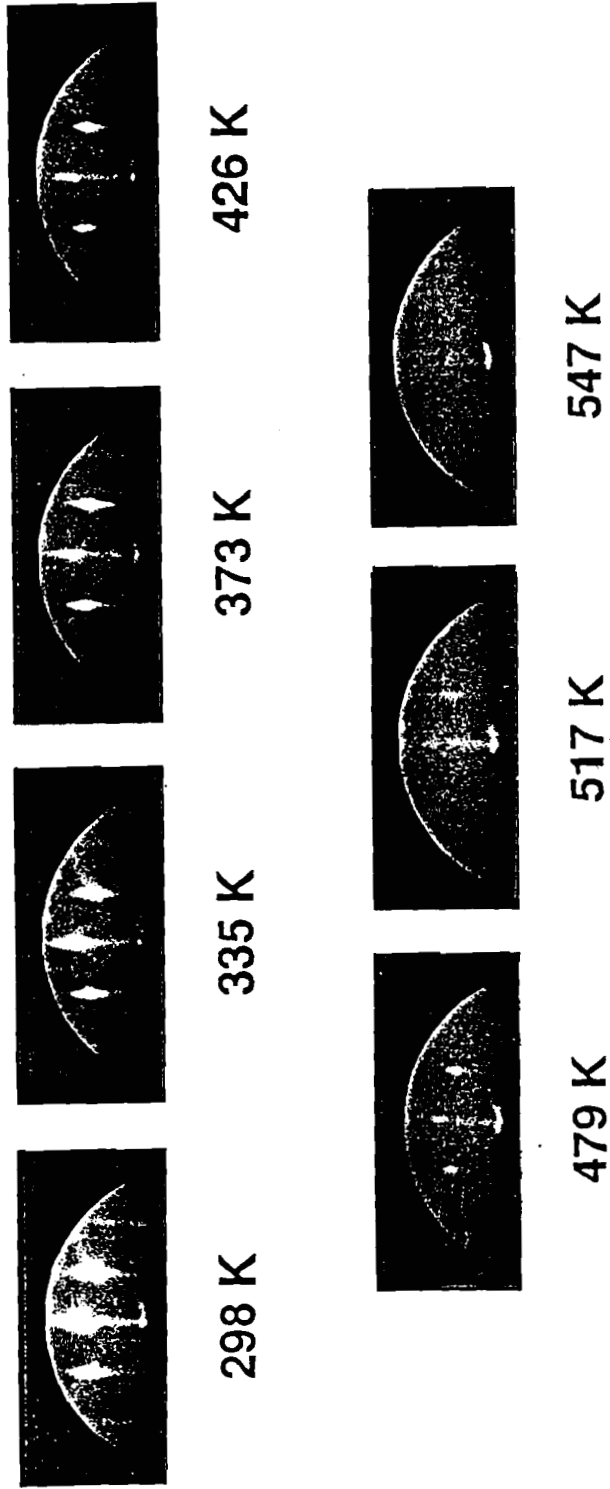


Figure 32. Photographs of the RHEED pattern of Pb(110) taken at various temperatures approaching the bulk melting point. Above $T_m - 50$ K, the diffraction intensity vanishes indicating that the probed layer is disordered.

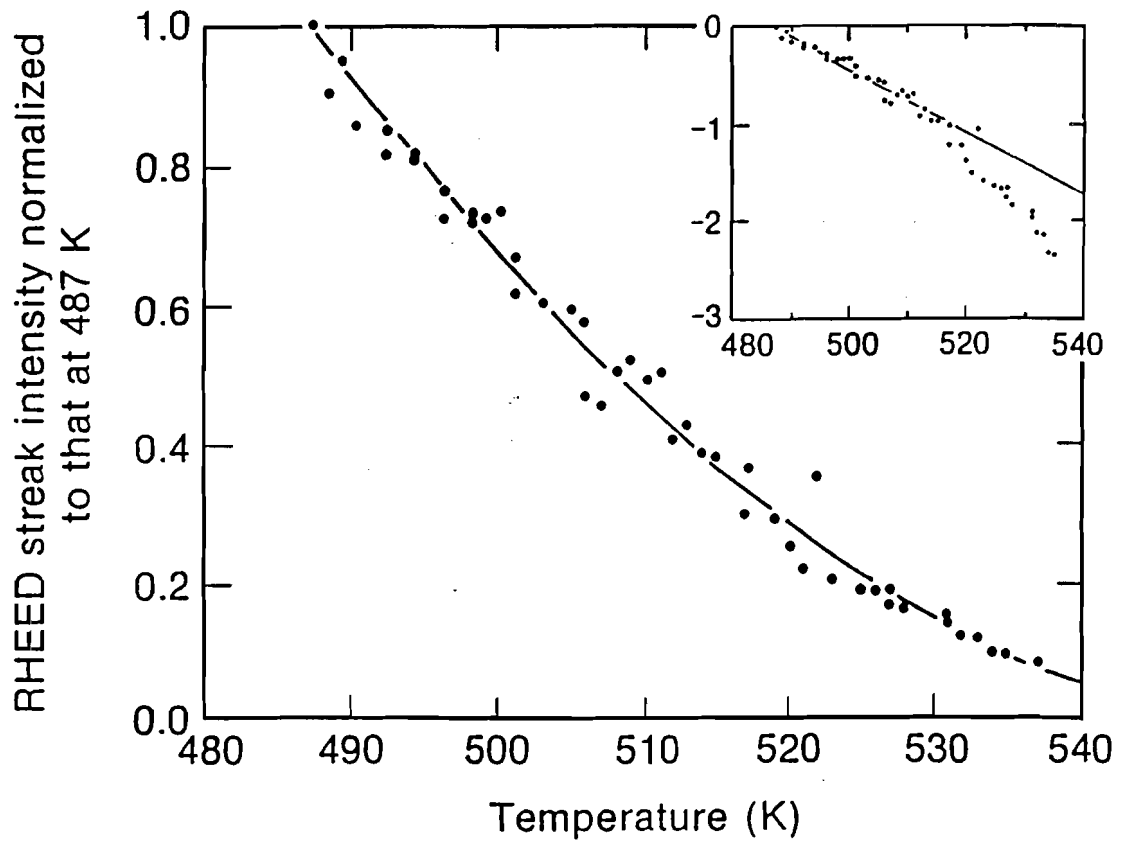


Figure. 33. RHEED streak intensity from Pb(110) normalized to that at 487 K versus temperature. A curve fit is made to the data and is used with the heat diffusion model to obtain the predicted time-resolved modulation of the RHEED streak intensity in Fig. 34. Inset: The data is plotted on a semilogarithmic scale. The line fit includes data points up to that which maximizes the linear correlation coefficient. The data departs from exponential Debye-Waller behavior at $T \sim 520$ K.

layer is disordered. The disordering temperature for the probed surface layer is therefore defined to be $T_d \sim 540$ K. This behavior is qualitatively similar to that observed by Yang and coworkers on Pb(110) with high-resolution LEED.¹¹ In that experiment, the intensity of the (00) beam at the in-phase condition departed from a Debye-Waller attenuation at ~ 520 K.

Time-resolved structural measurements were performed on Pb(110). In these experiments, the RHEED streak intensity, normalized to that at the sample bias temperature of 487 K, was obtained for given delay times between the arrival of the laser heating pulse and the electron probe pulse. Results are given in Fig. 34, where the solid lines represent the conversion of the temperature obtained from a one-dimensional heat diffusion model (Eq. 3.3.3) to a normalized diffraction intensity using the static calibration of Fig. 33. The following values were used for the model: $C = 1.58 \times 10^6$ J/m³K is the heat capacity per unit volume,¹² $K = 32.2$ W/mK is the thermal conductivity,¹² $R = 0.81$ is the reflectivity,¹³ $\alpha = 7.06 \times 10^7$ m⁻¹ is the absorption coefficient,¹³ and the peak laser intensity, I_p , for each of the sets is given in the caption of Fig. 34.

The error bars in Fig. 34 reflect the uncertainty of the RHEED streak intensity and are primarily due to MCP noise. Other sources of error in the time-resolved experiments include the spatial nonuniformity of the laser heating, which was measured to be $\pm 12\%$ across the width of the sample, and the stability of the laser. The spatial nonuniformity of the heating beam was measured by observing the transmission through a 500 μ m pinhole passed through the beam at the target-equivalent-plane. The long-term laser stability was monitored throughout the experiment. The temporal position of the model with respect to the experimental data was set by minimizing the mean-square difference between model and experimental data for the times between 1-2

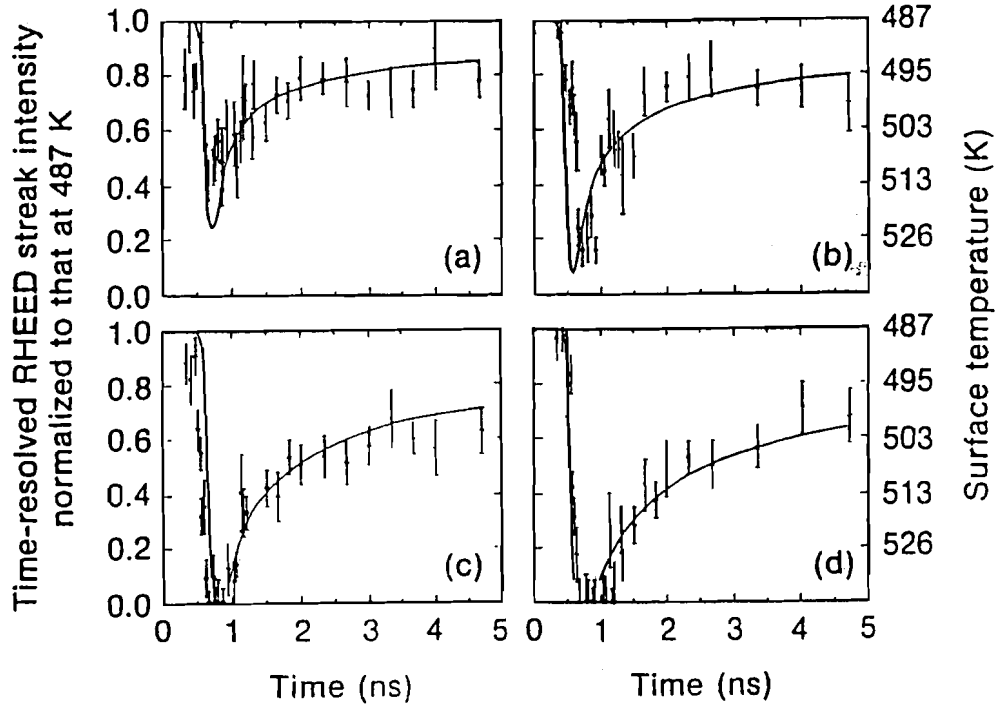


Figure 34. Time-resolved RHEED streak intensity measurements on Pb(110). The pulse width of the laser is measured at full-width at half-maximum (FWHM). The corresponding surface temperature is obtained using the data of Fig. 33. (a) $I_p = 1.4 \times 10^7$ W/cm², 165 ps FWHM, (b) $I_p = 2.0 \times 10^7$ W/cm², 165 ps FWHM, (c) $I_p = 2.7 \times 10^7$ W/cm², 175 ps FWHM, (d) $I_p = 3.6 \times 10^7$ W/cm², 170 ps FWHM. In (c) and (d) the normalized streak intensity is seen to vanish for some time indicating that order is lost in the probed surface layer. The subsequent reappearance of the streak intensity indicates the reordering of the surface.

ns in Fig. 34a-c and between 1.3 and 3.3 ns for Fig. 34d. In these time intervals, convolution effects are not expected to be significant.

In Figs. 34a and 34b, I_p is low enough to lead to simple heating rather than surface disordering. The surface temperature was raised from 487 K to observed peak surface temperatures of ~ 515 K and ~ 530 K in Figs. 34a and 34b, respectively. This is in reasonable agreement to the values of 523 K and 537 K predicted by the heat diffusion model. In Figs. 34c and 34d, the peak laser intensity was increased to facilitate surface heating to temperatures above T_d . In these sets, the heat diffusion model predicted peak surface temperatures of 558 K ($T_d + 18$ K) and 581 K ($T_d + 41$ K), respectively. In both cases, the normalized RHEED streak intensity is observed to vanish for some time indicating that the probed surface layer is disordered. The time duration over which the diffraction intensity vanishes increases from ~ 200 ps for a peak predicted temperature of $T_d + 18$ K (Fig. 34c) to ~ 500 ps for a peak predicted temperature of $T_d + 81$ K (Fig. 34d). We conclude that, with the heating rate of 10^{11} K/s available from pulsed laser heating, surface disordering cannot be bypassed. Furthermore, from the time-resolved data we see that the temperature at which the surface disorders is not significantly altered from that which was measured statically.

Subsequent to disordering, the surface recrystallizes and cools as the heat is conducted to the bulk of the sample. This is evident from the recovery of the diffraction intensity. In Fig. 34c and 34d, the results of the experiment were in accord with the model in the times where the normalized RHEED streak intensity is nonvanishing, indicating agreement with the results from heat diffusion both prior and subsequent to surface disordering. This is an indication that the nucleation and growth of the disordered layer, as well as the regrowth of crystalline order, occur on a time scale less than the 180 ps pulse width of the electron probe.

The conclusion that surface disordering is a reversible process is based on static experiments where the disordered layer thickness is shown to be a distinct function of temperature, a quality that distinguishes surface disordering from bulk melting. The reversibility of surface disordering has not been previously tested for extremely high heating and cooling rates. The time-resolved results in Fig. 34 that show the recovering elastic diffraction intensity subsequent to surface disordering indicate that surface disordering is reversible even at extremely high heating and cooling rates.

The observations of the fast regrowth of crystalline order on the time scale of this experiment are consistent with the time scales for atomic rearrangement on Pb(110) that have been deduced from measurements of surface self-diffusion using He-scattering.¹⁴ The results of the He-scattering experiment were described well by the following expression for the temperature-dependent mobility of surface atoms on Pb(110):¹⁴

$$D_s(T) = D_0 \exp\left(\frac{-Q_s}{k_B T}\right), \quad (4.2.1)$$

where $D_0 = 26 \text{ cm}^2/\text{s}$, the activation energy of diffusion is $Q_s = 0.65 \text{ eV}$, k_B is Boltzmann's constant, and T is temperature. The study concluded that for $T \geq 550 \text{ K}$, more than 50 K *below* T_m , the mobility of surface atoms exceeds that of the bulk liquid. The above expression yields a value of $\sim 0.23 \text{ \AA}^2/\text{ps}$ at $T_d \sim 540 \text{ K}$, comparable to the self-diffusion coefficient of liquid Pb close to T_m ($0.22 \text{ \AA}^2/\text{ps}$). At a temperature of T_d , over the 180 ps time scale of our electron probe, the disordered atoms diffuse over an area of $\sim 40 \text{ \AA}^2$. This area is sufficient to include all adjacent lattice sites that are potentially unoccupied. Therefore, over the time duration of the

electron probe, atoms in the disordered layer have sufficient mobility to travel to adjacent lattice sites.

The time-resolved measurements on Pb(110) lead us to conclude that for heating and cooling rates on the order of 10^{11} K/s, (i) surface disordering could not be bypassed, therefore precluding the existence of a nucleation barrier to disordering for these conditions, (ii) the temperature at which the surface disorders is not altered significantly from that measured statically, (iii) the nucleation and growth of surface disorder occurs on a time scale less than 180 ps even for relatively small departures over T_d , and (iv) surface disordering is reversible upon cooling, even at the high rates achieved with pulsed laser heating. The disordering of the Pb(110) surface has recently been studied using a many-body molecular dynamics potential. Reversible disordering was observed in the simulations for cooling rates comparable to those obtained in the present experiments.¹⁵

REFERENCES

1. C. V. Shank, R. Yen, and C. Hirlimann, *Phys. Rev. Lett.* **51**, 900 (1983).
2. B. C. Larson, J. Z. Tischler, and D. M. Mills, *J. Mater. Res.* **1**, 144 (1986).
3. J. Y. Tsao, S. T. Picraux, P. S. Peercy, and M. O. Thompson, *Appl. Phys. Lett.* **48**, 278 (1986).
4. G. J. Galvin, M. O. Thompson, J. W. Mayer, R. B. Hammond, N. Paulter, and P. S. Peercy, *Phys. Rev. Lett.* **48**, 33 (1982).
5. S. Williamson, G. Mourou, and J. C. M. Li, *Phys. Rev. Lett.* **52**, 2364 (1984).
6. A. Yariv, *Optical Electronics*, (Holt, Rinehart, and Winston, New York, 1985), pp. 227-246.
7. J. E. Sipe, V. Mizrahi, and G. I. Stegeman, *Phys. Rev. B* **35**, 9091 (1987).
8. J. W. Herman and H. E. Elsayed-Ali, *Phys. Rev. Lett.* **68**, 2952 (1992).
9. See, for example, J. F. van der Veen, B. Pluis, and A. W. Denier van der Gon in *Chemistry and Physics of Solid Surfaces VII*, edited by R. Vanselow and R. F. Howe (Springer, Berlin, 1988).
10. J. W. M. Frenken, F. Huussen, and J. F. van der Veen, *Phys. Rev. Lett.* **58**, 401 (1987).
11. H. -N. Yang, T. -M. Lu, and G. -C. Wang, *Phys. Rev. Lett.* **63**, 1621 (1989).
12. *Thermophysical Properties of Matter*, edited by Y. S. Toukourkian (Plenum, New York, 1970), Vols. 1 and 4.
13. From $R = [(n - 1)^2 + k^2]/[(n + 1)^2 + k^2]$ and $\alpha = 4\pi k/\lambda$, where n and k are the real and imaginary parts of the complex index of refraction. The values of n and k are obtained from an interpolation of the data in A. I. Golovashkin and G. P. Motulevich, *Zh. Eksp. Teor. Fiz.* **53**, 1526 (1967) [*Sov. Phys. JETP* **26**, 881 (1968)].

14. J. W. M. Frenken, J. P. Toennies, and Ch. Woll, *Phys. Rev. Lett.* **60**, 1727 (1988).
15. C. K. Ong (private communication).

CHAPTER 5: SUPERHEATING OF Pb(111)*

5.1 Supercooling versus Superheating

For many years, condensed matter physicists have puzzled over the experimental fact that while the supercooling of liquids is commonly observed, the superheating of solids is rarely observed.¹ The maximum observed supercooling of the melts of selected metals is given in Table 3. From Table 3, it is evident that supercooling temperatures of several hundred degrees are common. Supercooling is attributed to a nucleation barrier to solidification that is a result of the competition between the decrease in free energy upon solidification and the increase in free energy associated with the existence of a solid-liquid interface. This is expressed in the following expression for the free energy, Γ , of a solid droplet which has formed in a supercooled melt:¹

$$\Gamma = -\frac{4}{3}\pi r^3 L \frac{\Delta T}{T_m} + 4\pi r^2 \gamma_{sl} \quad (5.1.1)$$

Here, r is the radius of the droplet, assumed to be spherical, L is the heat of fusion, ΔT is the amount of supercooling, and γ_{sl} is the solid-liquid interfacial free energy. The first term in Eq. 5.1.1 represents the decrease in free energy associated with the solidification of the droplet. This term is proportional to the volume of the droplet. The second term represents the increase of free energy associated with the creation of a solid-liquid interface. The second term is proportional to the surface area of the droplet. The resultant free energy Γ is plotted in Fig. 35 for several supercooling temperatures using the parameters of Pb as an example. It is seen that for droplets with r less than a critical radius r_0 , there exists a nucleation barrier to solidification. For $r < r_0$, the

* J. W. Herman and H. E. Elsayed-Ali, Phys. Rev. Lett. 69, 1228 (1992).

Table 3: Maximum Observed Undercooling of Melts of fcc Metals*

<u>METAL</u>	<u>T_m (K)</u>	<u>ΔT (K)</u>
Al	931.7	130
Ni	1725	319
Cu	1356	236
Pd	1828	332
Ag	1233.7	227
Pt	2043	370
Au	1336	230
Pb	600.7	80

*From D. Turnbull, J. Appl. Phys. 21, 1022 (1950).

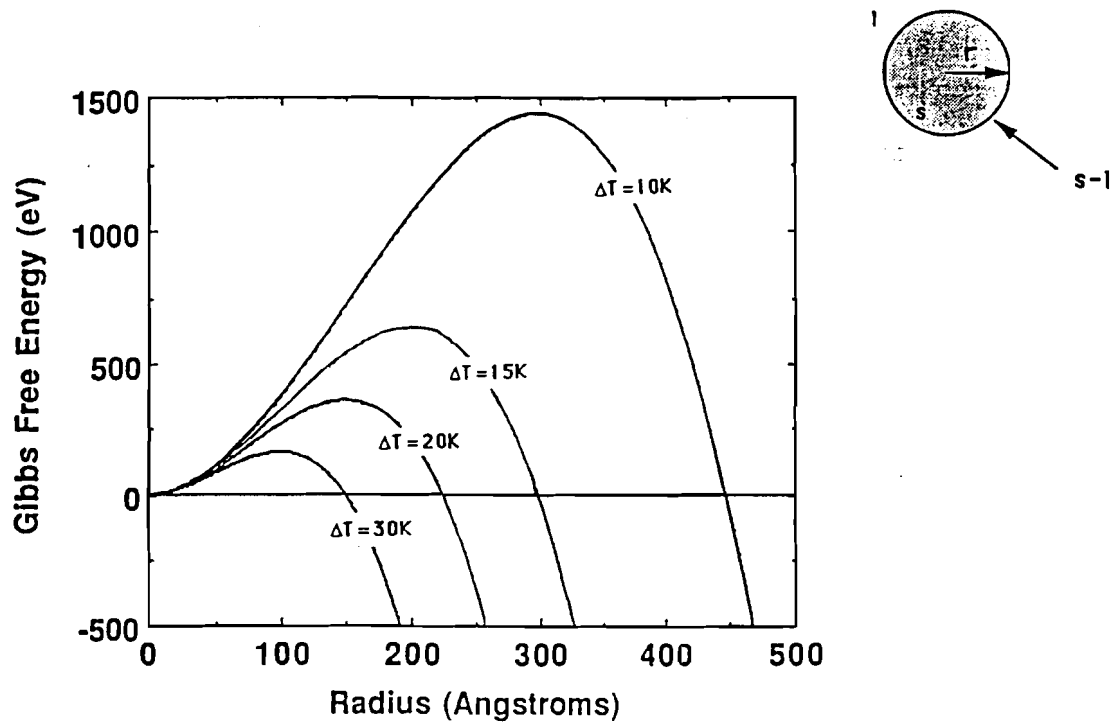


Figure 35. Free energy of a spherical supercooled droplet versus radius. Plots are given for varying amounts of supercooling.

droplet dissolves into the liquid and the system remains supercooled. The nucleation barrier is seen to decrease with increasing supercooling. Therefore, it becomes increasingly difficult to supercool a liquid without nucleating a solid "seed" with effective radius greater than r_0 . When such a nucleus is formed, the nucleation barrier is exceeded and the supercooled liquid rapidly solidifies and accesses a global minimum in the free energy, corresponding to the entire liquid being transformed to a solid. The existence of impurities in the liquid or rough walls in the container in which the liquid resides provides nucleation sites for solidification. The critical radius is found by minimizing the free energy Γ with respect to r :

$$r_0 = \frac{2T_m\gamma_{sl}}{L\Delta T} \quad (5.1.2)$$

A plot of r_0 versus supercooling is shown in Fig. 36 for the parameters of Pb.

The symmetric argument, applied to melting would imply that superheating is equally probable. However, the thin, disordered surface layer that forms on most materials below T_m provides a vast two-dimensional site for melting into the bulk as T_m is approached. Therefore, for surfaces that exhibit surface melting, or materials that consist of such surfaces, there does not exist a nucleation barrier for melting and this precludes substantial superheating. This accounts for the difficulty in superheating metals.

As a result of surface-initiated melting, the superheating of metals is not commonly observed. However, superheating of solids can be observed under some special conditions. Quartz and other solids which have highly viscous melts can be readily superheated.² This can be understood by considering the speed of propagation,

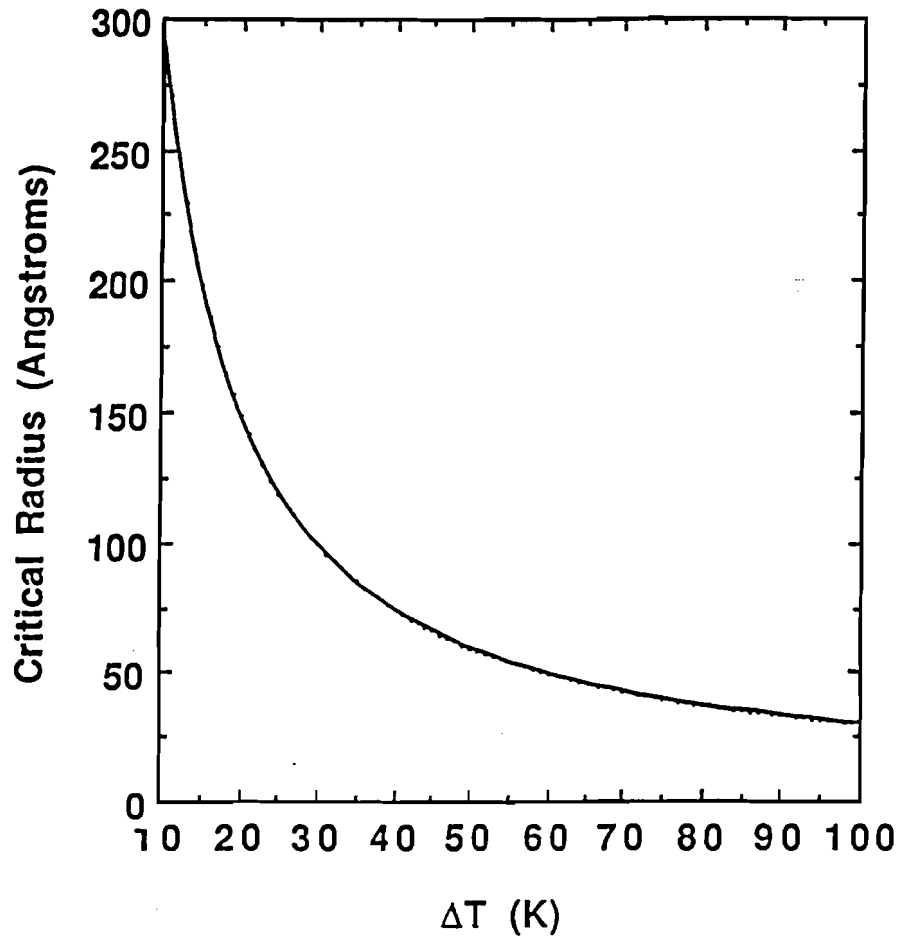


Figure 36. Critical radius for homogeneous nucleation of the supercooled liquid into a solid. The critical radius decreases with increasing supercooling.

v , of the solid-liquid interface.³ In this treatment, v is proportional to D , the coefficient of self-diffusion in the liquid. According to the Stokes-Einstein relation,

$$D = \frac{k_B T}{3\pi\lambda\eta} \quad (5.1.3)$$

Where k_B is Boltzmann's constant, T is temperature, λ is the atomic separation in the liquid, and η is the viscosity. Since v is proportional to D , it follows that v is inversely proportional to the viscosity, η . Therefore, solids that melt into highly viscous liquids are associated with extremely slow motion of the solid-liquid interface, which allows the interior of the solid to be substantially superheated.²

Typically, melts of metals have viscosities many orders of magnitude lower than that of the previously mentioned solids. Therefore, once the surface melts, the solid-liquid interface can propagate into the bulk with velocities approaching the speed of sound in the metal.⁴ However, by bypassing the melting effects of the surface, modest superheating of metals has been achieved. Single-crystal rods of Sn were internally heated by passing a current through them, while the surface was preferentially cooled to prevent melting.⁵ Superheating of approximately 2 K was observed. A further experiment involved coating one solid within another of higher T_m to eliminate the solid-vapor interface.⁶ In this experiment, 100 μm spheres of Ag were coated with a thin (10 μm) layer of Au. The lattice mismatch of Ag and Au is very small, leading to a relatively unstrained interface. The melting point of Au (1337 K) exceeds that of Ag (1234 K). The coated spheres were raised to temperatures above the melting point of Ag but below that of Au. The ensemble of spheres was examined with scanning electron microscopy and it was determined that a subset of the spheres was superheated to $\sim T_m + 25$ K. In analogous experiments, metal precipitates were

embedded in a host metal of higher T_m .⁷ Superheating temperatures of up to $T_m + 100$ K have been observed in these experiments. In addition, superheating of free-standing Al thin films was observed using time-resolved transmission electron diffraction.⁸ An ultrafast laser pulse was used as the transient heating source.

An outstanding question has been whether a surface which does not experience surface melting can be superheated. Experiments performed on *free* surfaces showed that superheating of several degrees could be observed on small metal platelets with extensive close-packed, nonmelting surfaces.⁹⁻¹¹ In these experiments, small platelets of Pb and Bi containing extensive {111} and {0001} surfaces, respectively, were fabricated. These surfaces have the property that they do not exhibit disordering below T_m . The structure of the platelets at temperatures close to and exceeding T_m was examined using electron microscopy. It was observed that the number of solid platelets decreased with time although the actual melting of an individual platelet occurred too rapidly to resolve in time. A subset of the ensemble of platelets experienced a significantly large time delay in melting at temperatures *above* T_m which allowed them to be transiently superheated. In these experiments, the Pb and Bi platelets were superheated by 2 K and 7 K, respectively.^{9,11}

5.2 SUPERHEATING OF Pb(111)¹²

In this set of experiments, we studied the close-packed, nonmelting Pb(111) surface to determine if the surface could be superheated to a larger degree using fast laser heating. As with Pb(110), we first measured the RHEED streak intensity versus temperature. The angle of incidence of the 18.2 keV electron beam was $\sim 2^\circ$ leading to a probed depth of 2 monolayers. The electron beam was incident along the $\langle 01\bar{1} \rangle$ azimuth. Photographs of the RHEED pattern were taken as a function of temperature in analogy to those taken of Pb(110). Photographs of the diffraction pattern from

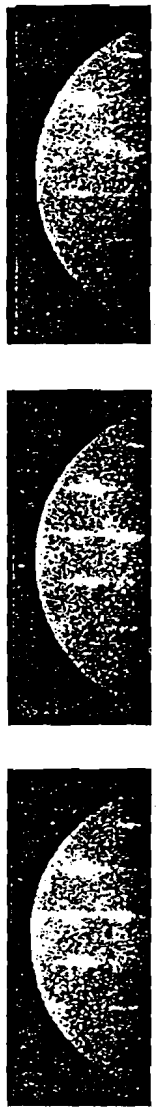
Pb(111) at various temperatures are given in Fig. 37. In contrast to Pb(110), the diffraction pattern from Pb(111) remains clearly visible up to the highest temperature attained on the heating stage, $T_m - 15$ K. Therefore, we conclude that Pb(111) remains ordered up to this temperature.

Results of a quantitative measurement of the RHEED streak intensity with the linear array camera are shown in Fig. 38 where the streak intensity is normalized to that at 407 K and the inset is plotted on a semilogarithmic scale. It is apparent that the behavior of Pb(111) is qualitatively different from that of Pb(110) shown in Fig. 32, where deviation from Debye-Waller behavior occurred at $\sim T_m - 80$ K. With Pb(111), the RHEED streak intensity is seen to decay exponentially in the considered temperature range which extends to $T_m - 15$ K. This is consistent with the Debye-Waller effect and agrees qualitatively with the results from medium-energy ion scattering where Pb(111) was shown to remain ordered up to $T_m - 0.5$ K.¹³

In the next set of experiments, Pb(111) was subjected to laser pulses with $I_p \sim 3.3 \times 10^7$ W/cm² while the sample bias temperature, T_{bias} , was raised from 495 K to 575 K. The RHEED streak intensity, normalized to that at T_{bias} is shown in Fig. 39a for the time corresponding to the minimum of the diffraction intensity, t_0 . The diffraction intensity is observed to decrease linearly with T_{bias} . No sudden decrease in diffraction intensity is observed that would indicate melting on the surface. The diffraction intensity is converted to a temperature jump, ΔT , by utilizing the static RHEED measurement of Fig. 38. The result of this conversion is shown in Fig. 39b, where we see that for $T_{bias} \geq 530$ K, the peak surface temperature, $T_{bias} + \Delta T$, exceeds T_m and the surface is superheated. It is observed that ΔT increases linearly with T_{bias} . This reflects the changing optical and thermal properties of the sample in



307 K 334 K 375 K 425 K



478 K 519 K 586 K

Figure 37. Photographs of the RHEED pattern of Pb(111), a surface which does not exhibit surface melting. The RHEED pattern is clearly visible up to $T_m - 15$ K.

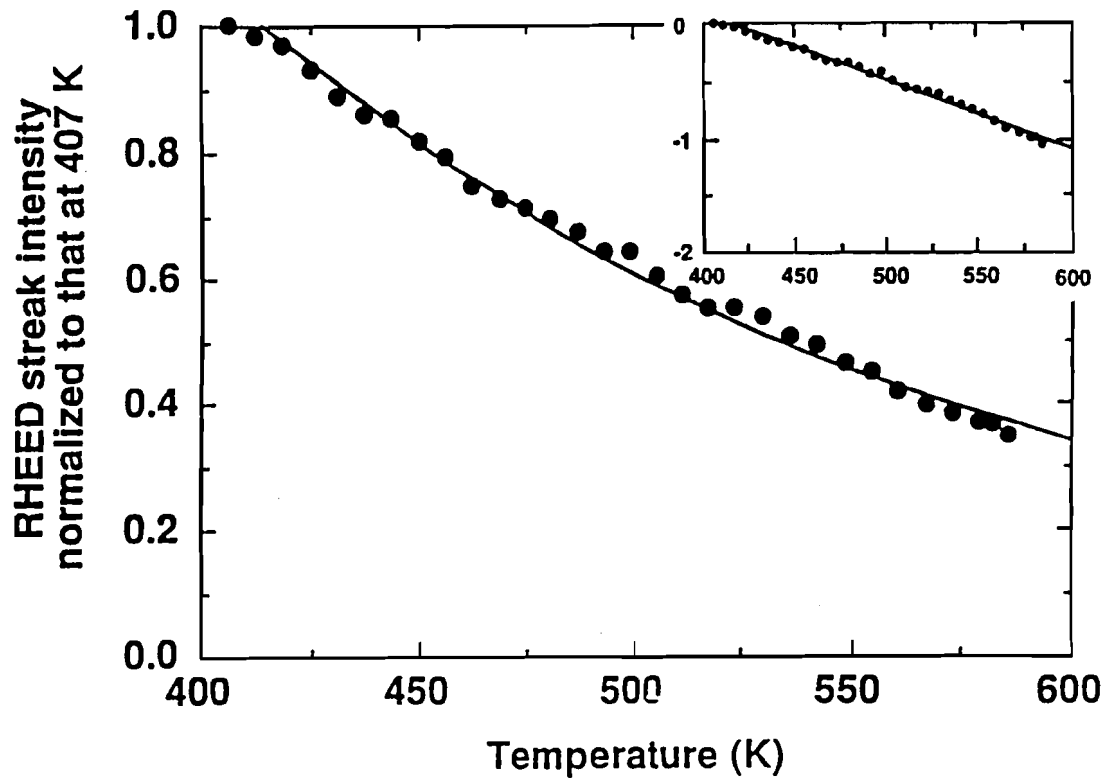


Figure 38. RHEED streak intensity of Pb(111), normalized to that at 407 K, versus sample temperature. An exponential curve fit has been made to the data. Inset: The data plotted on a semilogarithmic scale showing Debye-Waller behavior up to $T_m - 15$ K.

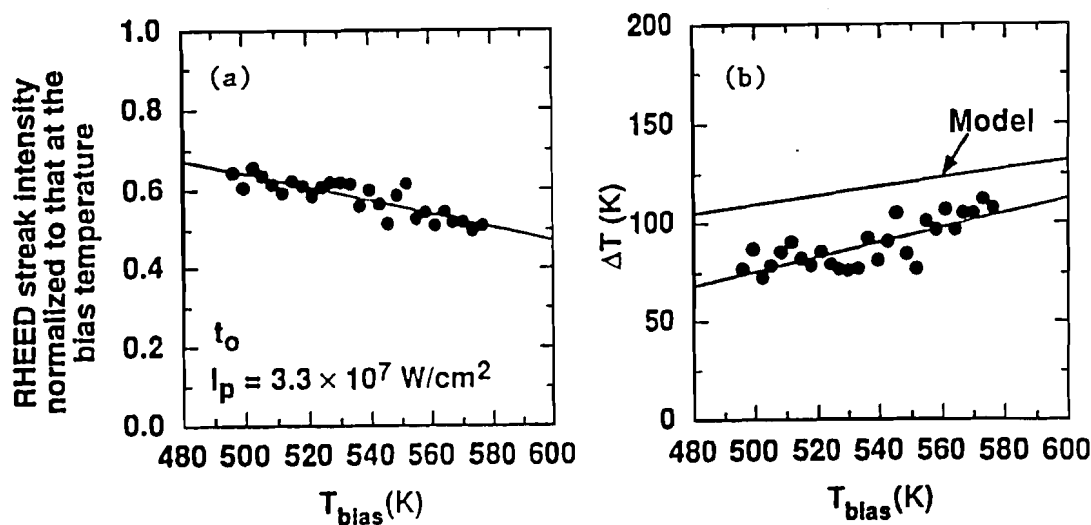


Figure 39. (a) Modulation of the normalized RHEED streak intensity for $I_p = 3.3 \times 10^7 \text{ W/cm}^2$ and varying sample bias temperatures, T_{bias} , performed at the time t_0 . (b) The streak intensity of (a) is converted to a peak surface-temperature rise, ΔT , using the data of Fig. 38. In addition, results from the heat diffusion model are plotted. The higher ΔT predicted by the model is most likely due to convolution effects which are most prominent at t_0 . For $T_{\text{bias}} \geq 530 \text{ K}$, the peak surface temperature exceeds T_m .

the considered temperature range. The change in surface reflectivity, R , with temperature is a significant factor in the increase of ΔT with T_{bias} , since the absorption of laser energy at the surface is proportional to $1 - R$. The reflectivity of the surface at the heating laser wavelength was measured directly and found to decrease from 0.78 to 0.74 in the temperature range of Fig. 39. The results from a solution of the heat diffusion model are shown in Fig. 39b as well. The larger ΔT predicted by the model is due to the previously mentioned convolution effects, which result in a somewhat lower experimentally-measured surface-temperature rise. In addition, the increase in ΔT with increasing T_{bias} was observed at delay times subsequent to t_0 and these results are given in Fig. 40. For a given T_{bias} we observe a decrease in ΔT with increasing delay time. This reflects the cooling of the surface after the arrival of the heating laser pulse.

Further experiments were performed to determine the magnitude of superheating that could be sustained on Pb(111). The sample was biased at $T_{bias} = 586$ K ($T_m - 15$ K) and transiently heated with varying peak laser intensities, I_p . The RHEED streak intensity normalized to that at T_{bias} , was obtained at given times throughout the laser heating process. Such a set is shown in Fig. 41. This set was performed at the temporal minimum of the RHEED streak intensity, t_0 , near the peak of the surface-temperature rise. The times of minimum RHEED streak intensity and maximum surface temperature do not coincide due to the effects of the convolution of the electron probe pulse with the temporal temperature profile of the surface. In the inset of Fig. 41, the data is plotted on a semilogarithmic scale. Two regimes are evident: the first, where $I_p < 3.5 \times 10^7$ W/cm², shows an exponential decay of the diffraction intensity with I_p , consistent with Debye-Waller behavior; in the second

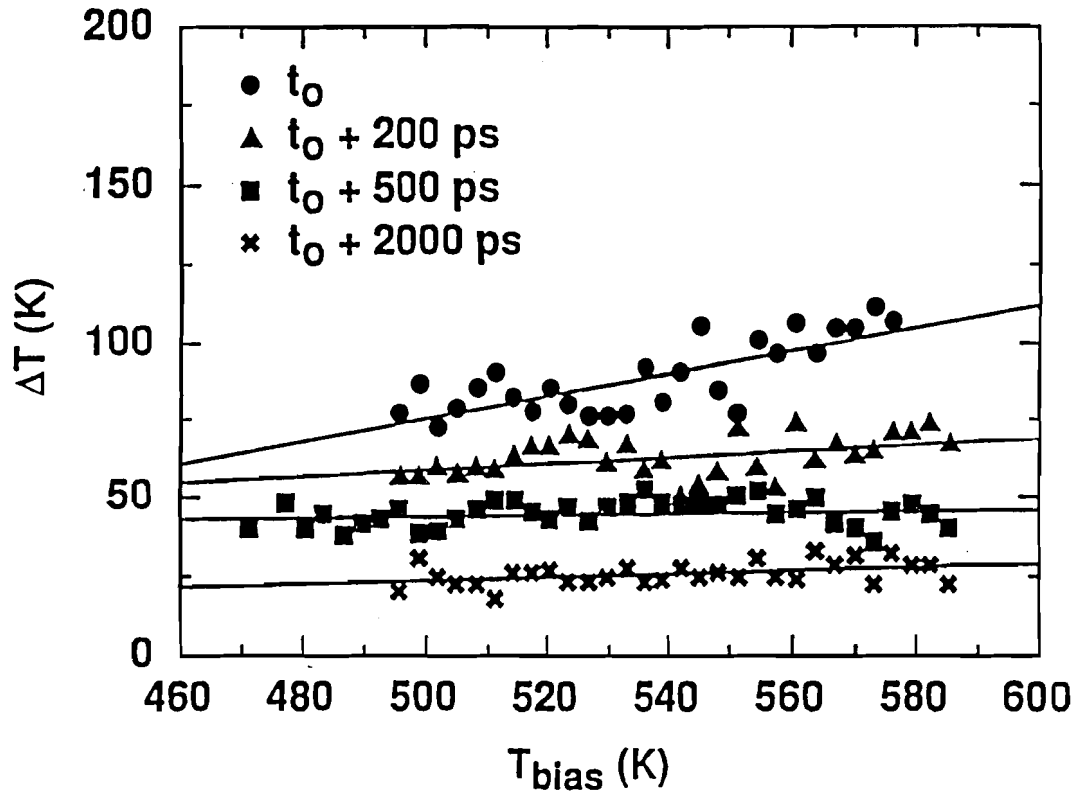


Figure 40. Surface-temperature rise versus T_{bias} for $I_p \sim 3.3 \times 10^7 \text{ W/cm}^2$ performed at t_0 and subsequent delay times. The general trend of increasing ΔT with T_{bias} is attributed to the change in optical and thermal properties of the sample in the considered temperature range.

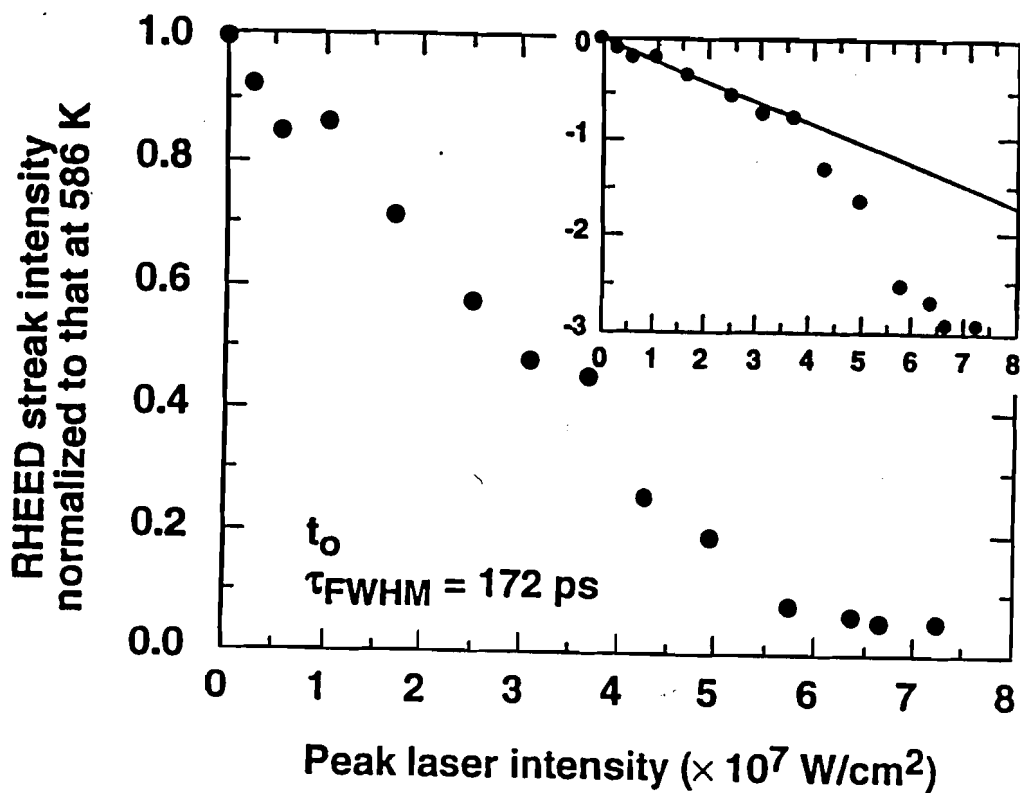


Figure 41. RHEED streak intensity normalized to that at 586 K versus peak laser intensity, I_p . This data set was obtained at the time corresponding to the temporal minimum of the normalized streak intensity, t_0 . Inset: A plot of the data on a semilogarithmic scale showing deviation from Debye-Waller behavior at $I_p \sim 3.5 \times 10^7 \text{ W/cm}^2$. The corresponding peak surface temperature is $\sim T_m + 120 \text{ K}$.

regime, where $I_p \geq 3.5 \times 10^7 \text{ W/cm}^2$, we observe a marked deviation from Debye-Waller behavior indicating that melting is occurring on the surface.

We next estimated the temperature at which deviation from exponential, Debye-Waller behavior occurs and identify this as the peak observed superheating temperature. To accomplish this, diffraction intensity modulations were considered for small I_p such that the corresponding temperature jumps, ΔT , lead to peak temperatures below T_m . In the Debye-Waller region, $\Delta T \propto I_p$; therefore the lower values of I_p can be used to make a correspondence between I_p and peak surface temperature. When this is done, we observe deviation from Debye-Waller behavior to occur at a temperature of $T \sim 720 \text{ K}$ ($\sim T_m + 120 \text{ K}$). Furthermore, the time-resolved diffraction data has a slope when plotted on a semilogarithmic scale that is equivalent to the slope from the static RHEED measurement of Fig. 38, within experimental error. This error can result from the fact that the experiment of Fig. 41 was performed at the time t_0 where convolution effects can be prominent. The exponential dependence of the normalized RHEED streak intensity up to $T_m + 120 \text{ K}$ indicates that the surface retains order above T_m and behaves according to the Debye-Waller effect with mean-square vibrational amplitudes in excess of that at T_m .

The time-resolved measurements of the diffraction intensity versus I_p were carried out at other times relative to the time t_0 . Fig. 42 shows measurements performed at $t_0 + 500 \text{ ps}$ and $t_0 + 4000 \text{ ps}$. The insets are plotted on a semilogarithmic scale. In both cases, for $I_p < 3.5 \times 10^7 \text{ W/cm}^2$, an exponential decrease in diffraction intensity with increasing I_p was observed. This is evident from the linear behavior in the insets. A distinct break from exponential behavior occurs at $I_p \geq 3.5 \times 10^7 \text{ W/cm}^2$, consistent with the value that was obtained at the time t_0 . This deviation from Debye-Waller behavior is due to melting taking place on the surface. The deviation, at peak

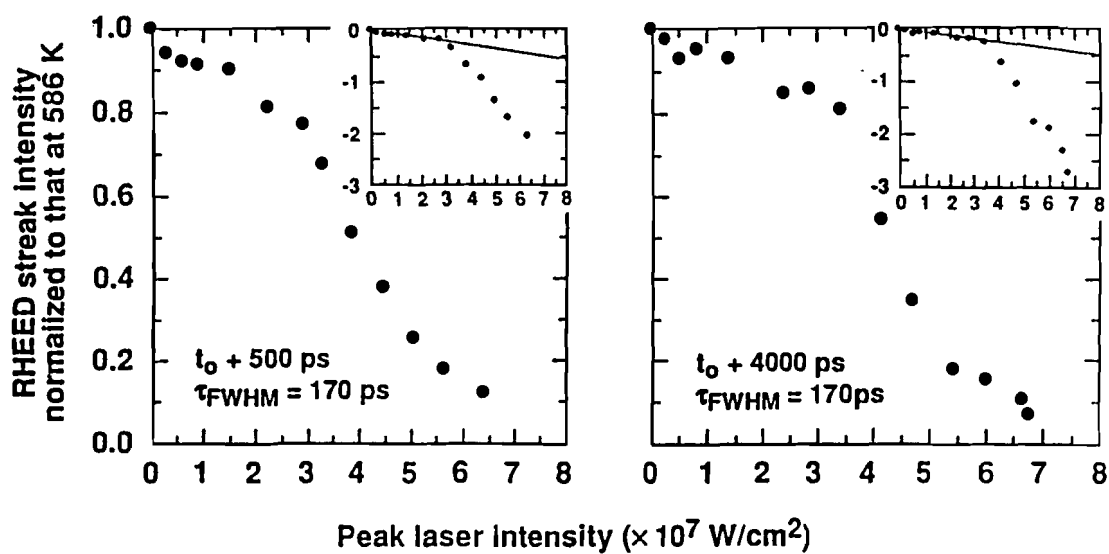


Figure 42. RHEED streak intensity normalized to that at 586 K versus peak laser intensity, I_p . These sets were performed at times of $t_0 + 500$ ps and $t_0 + 4000$ ps. The insets are plotted on a semilogarithmic scale and show the break from Debye-Waller behavior at $I_p \sim 3\text{-}4 \times 10^7$ W/cm 2 , consistent with what was observed at the time t_0 .

laser intensities $\geq 3.5 \times 10^7$ W/cm², is most likely not attributed to anharmonic vibrations due to the observed deviation from exponential behavior at $t_0 + 4000$ ps, an amount of time after t_0 where such vibrations should not be present due to the rapid decrease of the surface-temperature rise.

Similar measurements were performed with the electron beam incident at an angle of $\sim 1^\circ$ with respect to the surface. This led to a probed depth of less than a monolayer. Semilogarithmic plots of the RHEED streak intensity normalized to that at 586 K are shown in Fig. 43 for the times t_0 and $t_0 + 4000$ ps. A break from exponential Debye-Waller behavior is seen to occur at I_p between 3 and 4×10^7 W/cm², consistent with what was observed for the previous data with an angle of incidence of $\sim 2^\circ$.

Time-resolved experiments examining the RHEED streak intensity throughout the heating process were carried out with $T_{bias} = 586$ K. The RHEED streak intensity, normalized to that at 586 K, was obtained at various delay times. Results for varying I_p are shown in Fig. 44. Fig. 44a exhibits the qualities of classical heat diffusion: a rapid decrease in the normalized streak intensity followed by an increase as the heat is conducted to the bulk of the sample. The data set of Fig. 44a was normalized to sets taken at lower T_{bias} which corresponded to peak temperatures below T_m . This comparison showed good agreement indicating that the data of Fig. 44a is consistent with classical heat diffusion. Since the time-resolved RHEED streak intensity at $T_{bias} = 586$ K exhibited Debye-Waller behavior up to $I_p \sim 3.5 \times 10^7$ W/cm², the static RHEED calibration of Fig. 38 can be used to determine the peak ΔT of Fig. 44a. When this is done, a peak surface temperature of $T_m + 110$ K is deduced.

In Figs. 44b-d, the surface was subjected to $I_p > 3.5 \times 10^7$ W/cm², the threshold for Debye-Waller behavior. We observe a clear deviation from classical heat

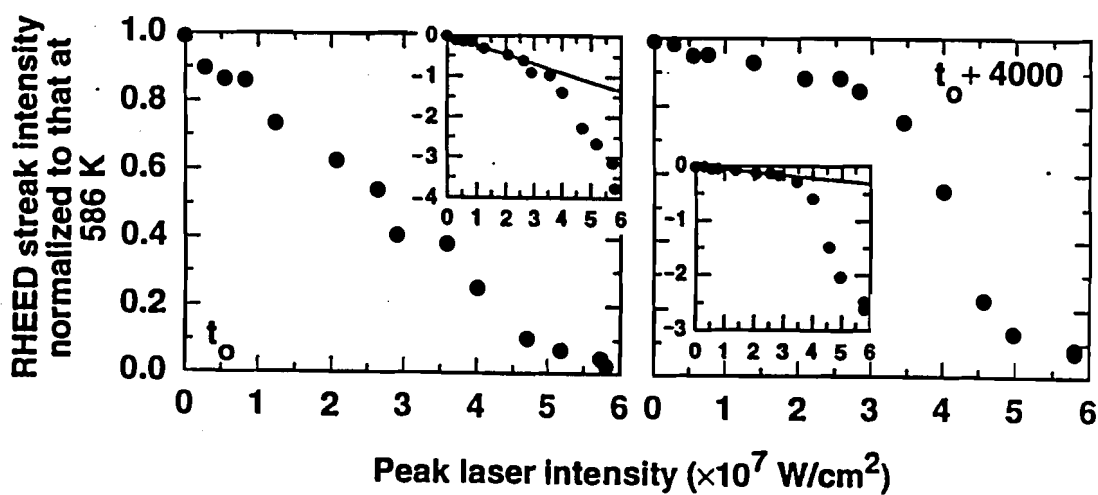


Figure 43. RHEED streak intensity normalized to that at 586 K versus peak laser intensity, I_p , for an electron beam angle of incidence of $\sim 1^\circ$ at the times t_0 and $t_0 + 4000$ ps. Insets show the departure from Debye-Waller behavior at $I_p \sim 3-4 \times 10^7$ W/cm².

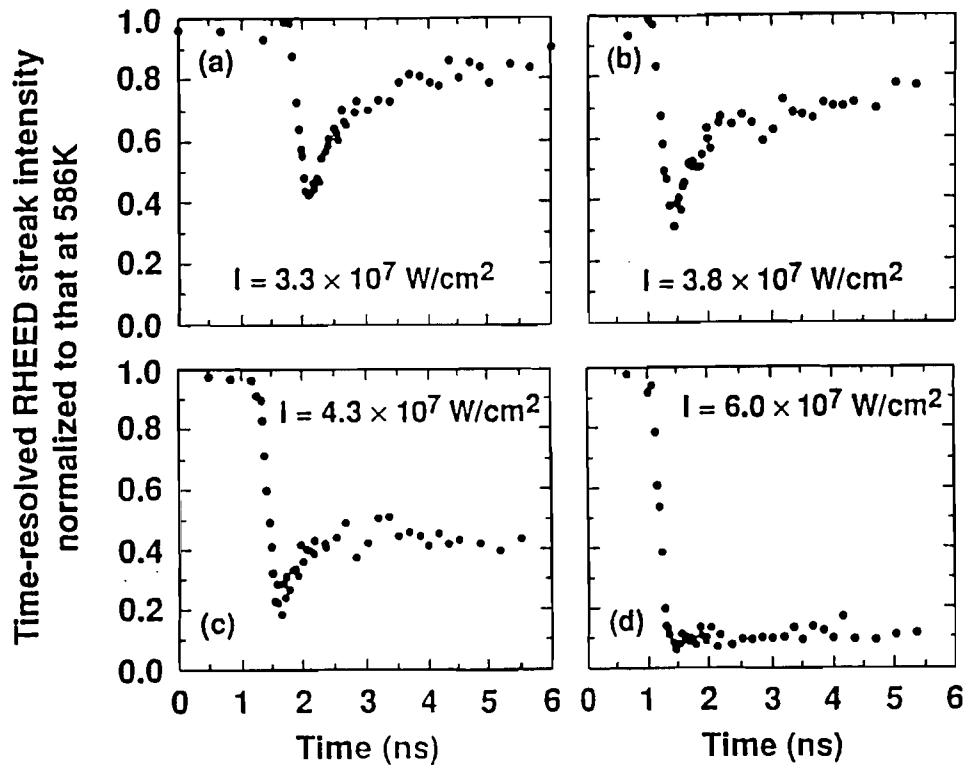


Figure 44. Time-resolved normalized RHEED streak intensity of Pb(111) irradiated with laser pulses of varying peak intensity. Set (a) is consistent with classical heat diffusion and corresponds to a peak surface temperature of $T_m + 110 \text{ K}$. In sets (b)-(d), where $I_p \geq 3.5 \times 10^7 \text{ W/cm}^2$, the surface begins to melt as is evident in the pronounced deviation from classical heat diffusion.

diffusion in the tail after ~ 1.5 ns. The streak intensity, subsequent to an initial fast rise at t_0 , fails to recover to what is expected from heat diffusion. The behavior at times after t_0 is also reflected in the data of Fig. 42. We attribute this to melting on part of the surface. In Figs. 44b-d, the value of the normalized streak intensity at times after t_0 depends on the ratio of the portion of the probed surface area that is molten to that which remains solid. This, in turn, is influenced by the spatial intensity profile of the laser pulse on the sample surface. In these experiments, the laser nonuniformity was measured to be $\pm 18\%$ across the width of the sample. This was accomplished by measuring the laser intensity passing through a small pinhole that was scanned through the beam. However, this measurement does not preclude the existence of laser nonuniformities on a micron scale. Laser intensity variations on this scale could influence the dynamics of the melting process.

The time τ is defined to be the time interval between t_0 and the time at which the time-resolved diffraction intensity deviates from behavior consistent with classical heat diffusion. To determine τ , the sets that show evidence for melting were compared with those exhibiting behavior consistent with classical heat diffusion. A nonmelting superheated set was normalized to a given melting set and subtracted from it. The difference that resulted was fitted with a polynomial which was differentiated to observe the break from nonmelting behavior. A plot of τ versus peak laser intensity is given in Fig. 45 for data sets biased at 586 K. The time τ is observed to decrease from 1200 ps to < 300 ps for $I_p \sim 3.8 \times 10^7$ W/cm² to $I_p \sim 6.0 \times 10^7$ W/cm², respectively.

From the experiments on Pb(111), we conclude that this surface, which was shown not to exhibit surface melting, sustains superheating to $\sim T_m + 120$ K. This is evident from the exponential Debye-Waller behavior of the RHEED streak intensity in this temperature range. Melting, which occurs for $T > T_m + 120$ K, is most likely

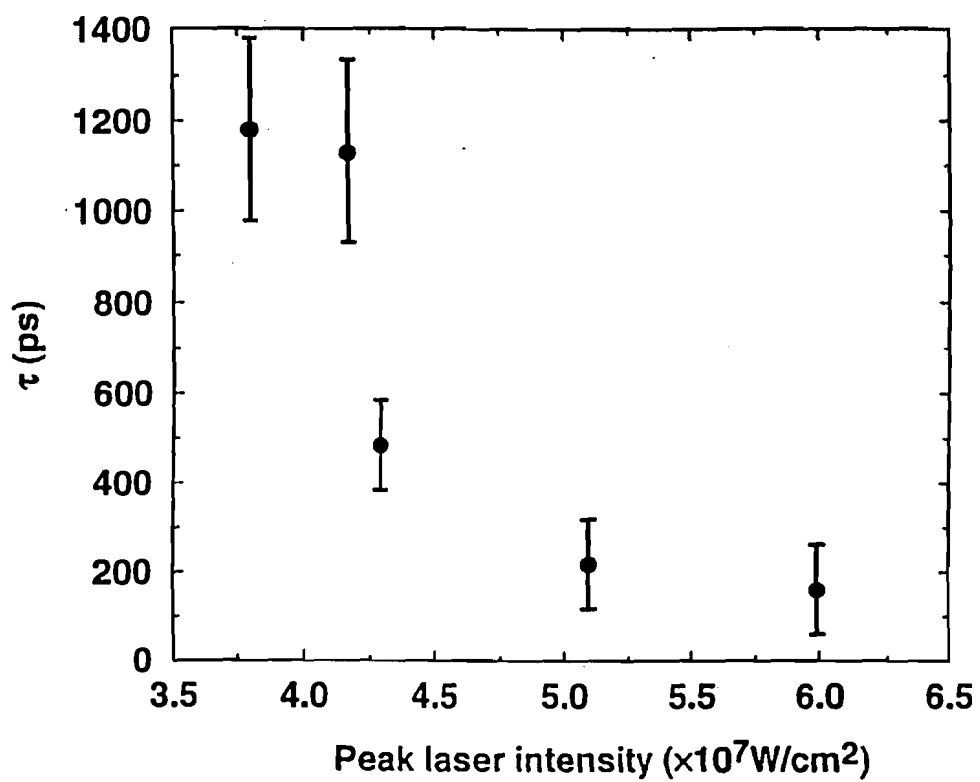


Figure 45. The time interval, τ , from t_0 to the time at which deviation from classical heat diffusion occurs, is extracted from data sets as in Figs. 44b-c. The time τ is seen to decrease with increasing peak laser intensity.

initiated by local spatial nonuniformities in the heating laser beam. In the superheating regime, the excess surface temperature is manifested as lattice mean-square vibrational amplitudes exceeding that at T_m . Melting is apparently bypassed by the 10^{11} K/s heating and cooling rates that are available with pulsed laser heating. At incident peak laser intensities greater than $\sim 3.5 \times 10^7$ W/cm², the surface melts as is evident from the pronounced deviation from Debye-Waller behavior. The larger heating rates available with lasers of shorter pulse width could conceivably lead to a larger degree of superheating.

As an interesting postscript to this work, recent molecular dynamics simulations were performed by Hakkinen and Landman examining the dynamics of melting and superheating of Cu surfaces.¹⁴ Motivated by the time-resolved laser heating experiments, they constructed a model that incorporated energy transfer from the electronic system to the lattice. The subsequent lattice dynamics were modeled with the many-body embedded-atom potential. They observed rapid and reversible disordering of the Cu(110) surface in analogy to Pb(110). In contrast to this, Cu(111) was shown to sustain superheating of 40 K. A systematic study of the magnitude of superheating is currently being undertaken.¹⁵ Further simulations focused on the effects of defects in the superheating process.¹⁴ Defects such as steps and vacancies are expected to be present on any metal surface in experimental situations. The simulations showed that even highly defected Cu(111) surfaces, with up to a 10% initial surface vacancy concentration, sustained substantial superheating. A non-diffusional settling mechanism involving adatoms was observed in the annealing process that acted to fill existing vacancies and restore crystalline order. Processes such as this may be involved in the time-resolved experiments on Pb(111), where a large degree of superheating was sustained on a surface that most likely contained a significant concentration of defects.

REFERENCES

1. D. P. Woodruff, *The Solid-Liquid Interface* (Cambridge University Press, Cambridge, 1973).
2. N. G. Ainslie, J. D. MacKenzie, and D. Turnbull, *J. Phys. Chem.* **65**, 1718 (1961); R. L. Cormia, J. D. MacKenzie, and D. Turnbull, *J. Appl. Phys.* **34**, 2239 (1963); D. R. Uhlmann, *J. Non-Cryst. Solids* **41**, 347 (1980).
3. D. Turnbull and M. H. Cohen, *Modern Aspects of the Vitreous State*, Vol 1, edited by J. D. MacKenzie (Butterworth, London, 1960).
4. C. A. MacDonald, A. M. Malvezzi, and F. Spaepen, *J. Appl. Phys.* **65**, 129 (1989).
5. S. E. Kaykin and N. P. Bene, *C. R. Acad. Sci. USSR* **23**, 31 (1939).
6. J. Daeges, H. Gleiter, and J. H. Perepezko, *Phys. Lett. A* **119**, 79 (1986).
7. L. Grabaek, J. Bohr, E. Johnson, A. Johansen, L. Sarholt-Kristensen, and H. H. Andersen, *Phys. Rev. Lett.* **64**, 934 (1990).
8. S. Williamson, G. Mourou, and J. C. M. Li, *Phys. Rev. Lett.* **52**, 2364 (1984).
9. G. D. T. Spiller, *Philos. Mag. A* **46**, 535 (1982).
10. J. J. Metois and J. C. Heyraud, *J. Phys. (Paris)* **50**, 3175 (1989).
11. S. J. Peppiatt, *Proc. R. Soc. London A* **345**, 401 (1975).
12. J. W. Herman and H. E. Elsayed-Ali, *Phys. Rev. Lett.* **69**, 1228 (1992).
13. B. Pluis, A. W. Denier van der Gon, J. F. van der Veen, and A. J. Riëmersma, *Surf. Sci.* **239**, 265 (1990).
14. H. Hakkinen and U. Landman, *Phys. Rev. Lett.* **71**, 1023 (1993).
15. U. Landman (private communication).

CHAPTER 6 TIME-RESOLVED STRUCTURAL STUDY OF Pb(100)*

The final surface studied was Pb(100), which has been shown to experience incomplete surface melting where the surface forms a nondiverging disordered layer of discrete thickness.¹ (The layer thickness is a multiple of $2\pi/k_1$, where k_1 is the magnitude of the wavevector corresponding to the first maximum in the structure factor of the bulk liquid.) Using MEIS, it was observed that the disordered layer that forms on the surface does not nucleate further melting up to a temperature of $T_m - 0.05$ K.² The aim of the time-resolved experiments on Pb(100) was to determine if the disordered layer that forms on the surface is stable at temperatures above T_m .

The first experiment on Pb(100) measured the temperature dependence of the RHEED streak intensity. The 15 keV electron beam was incident along the $\langle 001 \rangle$ azimuth at an angle of 3° , resulting in a probed depth of ~ 5 Å. This corresponds to approximately 3 monolayers. A plot of the RHEED streak intensity versus temperature, normalized to that at 377 K, is shown in Fig. 46. The inset is a plot of the data on a semilogarithmic scale. A nonexponential decrease in diffraction intensity with temperature was observed starting at a temperature of ~ 475 K. The data are qualitatively similar to that obtained on Pb(100) by Yang and coworkers using high-resolution LEED.³ The deviation from Debye-Waller behavior may initially be related to the surface expansion that they observed to occur between 300 and 470 K. In this temperature range, the surface undergoes an expansion exceeding that of the bulk by a factor of 7. The surface expansion is directly related to the anharmonic nature of the surface interatomic potential. In addition, deviation from Debye-Waller behavior can be attributed to the abrupt increase in vacancy concentration that they observed beginning at 510 K.³

* J. W. Herman, H. E. Elsayed-Ali, and E. A. Murphy, Phys. Rev. Lett. 71, 400 (1993).

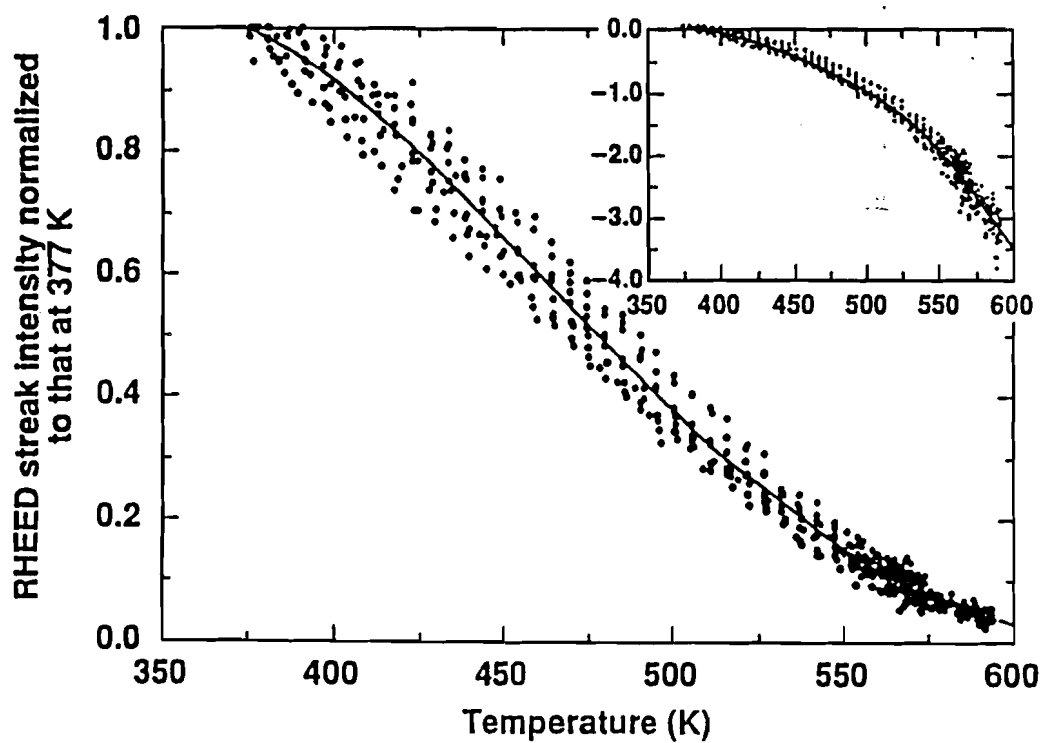


Figure 46. RHEED streak intensity from Pb(100) normalized to that at 377 K versus temperature. The inset shows the data plotted on a semilogarithmic scale. The solid lines are polynomial fits to the data. The streak intensity is observed to deviate from Debye-Waller behavior for $T \geq 450$ K.

To determine the peak temperature rise induced on the Pb(100) surface by the heating laser pulse, time-resolved measurements were performed at the time t_0 . For these experiments, the sample was biased at temperatures of 450 K and 533 K. The RHEED streak intensity, normalized to that at 450 K is shown in Fig. 47 for various peak laser intensities, I_p . The normalized streak intensity is converted to a temperature rise, ΔT , using the calibration of Fig. 46. The result of this conversion is shown in the inset of Fig. 47, where ΔT is plotted versus I_p . The temperature rise is observed to be directly proportional to I_p , which is consistent with classical heat diffusion. The maximum peak temperature in all of these sets is below T_m . These data do not account for the effect of convolution.

In the next set of experiments the RHEED streak intensity, normalized to that at a given T_{bias} is obtained for various peak laser intensities. In these experiments, which were performed at t_0 , T_{bias} is raised closer to T_m . Results are shown in Fig. 48, where the set in Fig. 48d is biased just 11 K below T_m . At sufficiently high I_p , the normalized streak intensity is observed to vanish, indicating that order has been lost in the probed surface layer. The value of I_p necessary to disorder the probed surface layer decreases from $\sim 4.3 \times 10^7$ W/cm² for $T_{bias} = 533$ K to $\sim 1.8 \times 10^7$ W/cm² for $T_{bias} = 590$ K. The data of Fig. 47 are used to determine the peak surface temperature at which the normalized RHEED streak intensity vanishes. In each of the sets of Fig. 48, the lowest I_p leading to a vanishing RHEED streak intensity is converted to a temperature rise using Fig. 47. From this conversion, we see that the peak surface temperature, $T_{bias} + \Delta T$, when order is lost in the probed surface layer is $\sim 615 \pm 20$ K. The error accounts for (i) the spread of the static RHEED data, (ii) the spread of the temperature rise data of Fig. 47, and (iii) the nonuniformity of laser heating, which is measured to be $\pm 25\%$ over the entire width of the sample. Factors that are not accounted for in this peak temperature include convolution effects and the changes in the thermal and optical

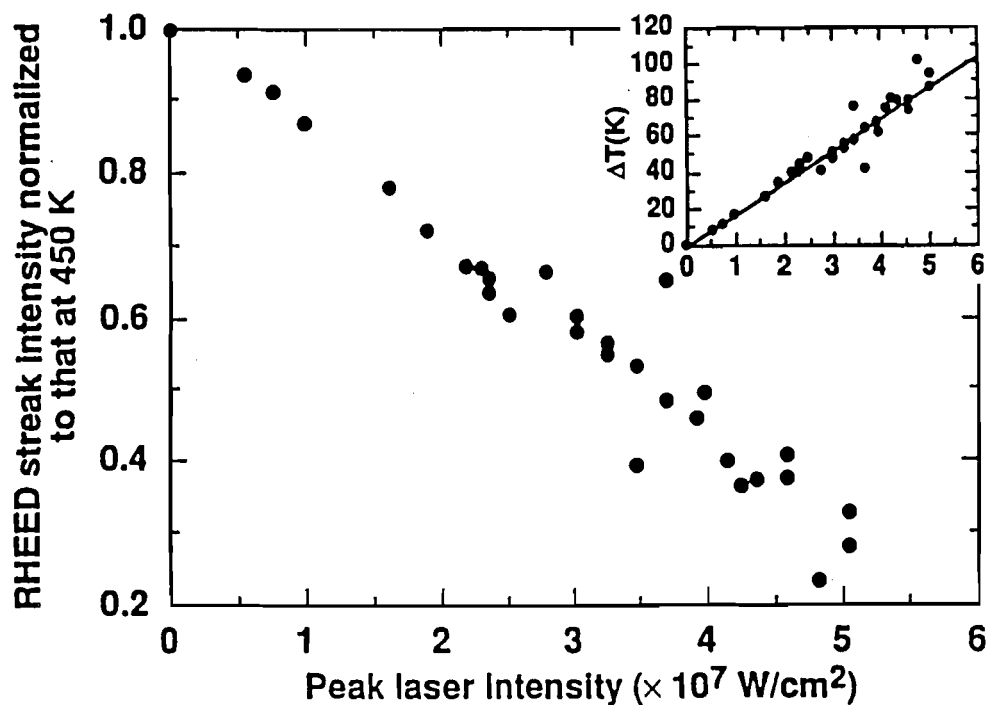


Figure 47. RHEED streak intensity versus peak laser intensity, I_p , on Pb(100) at the time t_0 . The sample was biased at 450 K. Inset: Peak surface-temperature rise, ΔT , versus I_p . The inset is a result of the conversion of the streak intensity modulation to a ΔT using the data of Fig. 46. This data is used to determine ΔT for data sets where T_{bias} is closer to T_m .

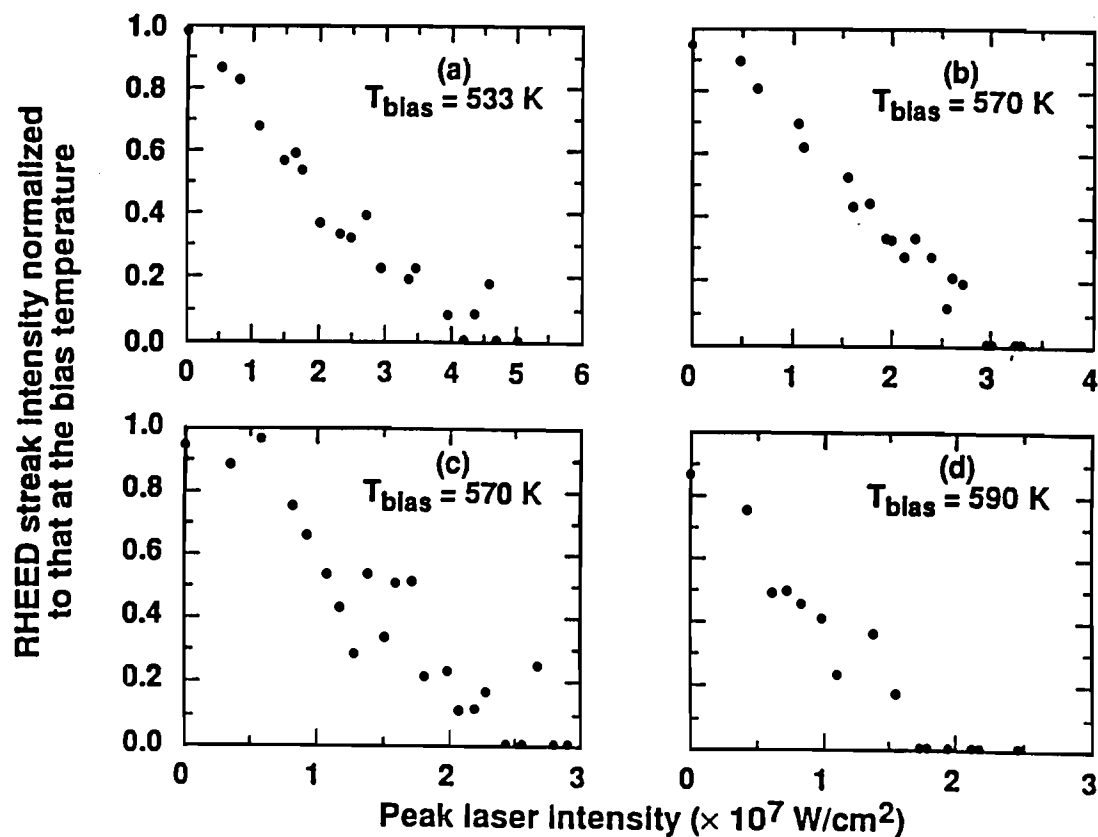


Figure 48. Normalized RHEED streak intensity versus peak laser intensity for bias temperatures successively closer to T_m . The streak intensity vanishes for I_p above a certain threshold which depends on T_{bias} . This threshold is used along with the data of Fig. 47 to determine the temperature at which order is lost in the probed layer.

properties of the sample that occur over the considered temperature range. These effects lead to a somewhat greater peak surface temperature than what is experimentally observed.

The temporal behavior of the heating and disordering process on Pb(100) was examined using time-resolved RHEED. The normalized RHEED streak intensities were obtained at various times between the arrival of the laser heating pulse and the electron probe pulse at the surface of the sample. In Fig. 49, results are given for varying sample bias temperatures and incident peak laser intensities. In Figs. 49a and 49b, the incident peak laser intensity was not sufficient to cause disorder in the probed layer. This is evident by the nonvanishing diffraction intensity in these sets. In Fig. 49c, sufficient laser intensity was provided to disorder the probed surface layer. This is evident from the vanishing streak intensity at time ~ 1 ns. Subsequent to disordering, the surface recrystallizes and cools as is seen from the increasing streak intensity at later times. Finally, in Fig. 49d, the streak intensity fails to recover for times ≥ 4 ns after the initial disordering, which is an indication of melting on the surface.

From our experiments on Pb(100) we conclude that residual order is present on Pb(100) at a peak surface temperature of 615 ± 20 K. Considering the previously mentioned convolution effects, it is likely that residual order is present above T_m . At this temperature the surface is most likely proliferated with defects such as vacancies.³ The degree of superheating would most likely be lowered by the presence of vacancies since vacancies are expected to act as nucleation sites for melting. Indeed, compared with the close-packed Pb(111) surface, where superheating to ~ 720 K was observed,⁴ the results on Pb(100) show evidence of residual order at a much lower surface temperature. Furthermore, the experiments on Pb(100) show that the disordered layer that forms near T_m is stable in a narrow temperature range above T_m . Evidently, in this

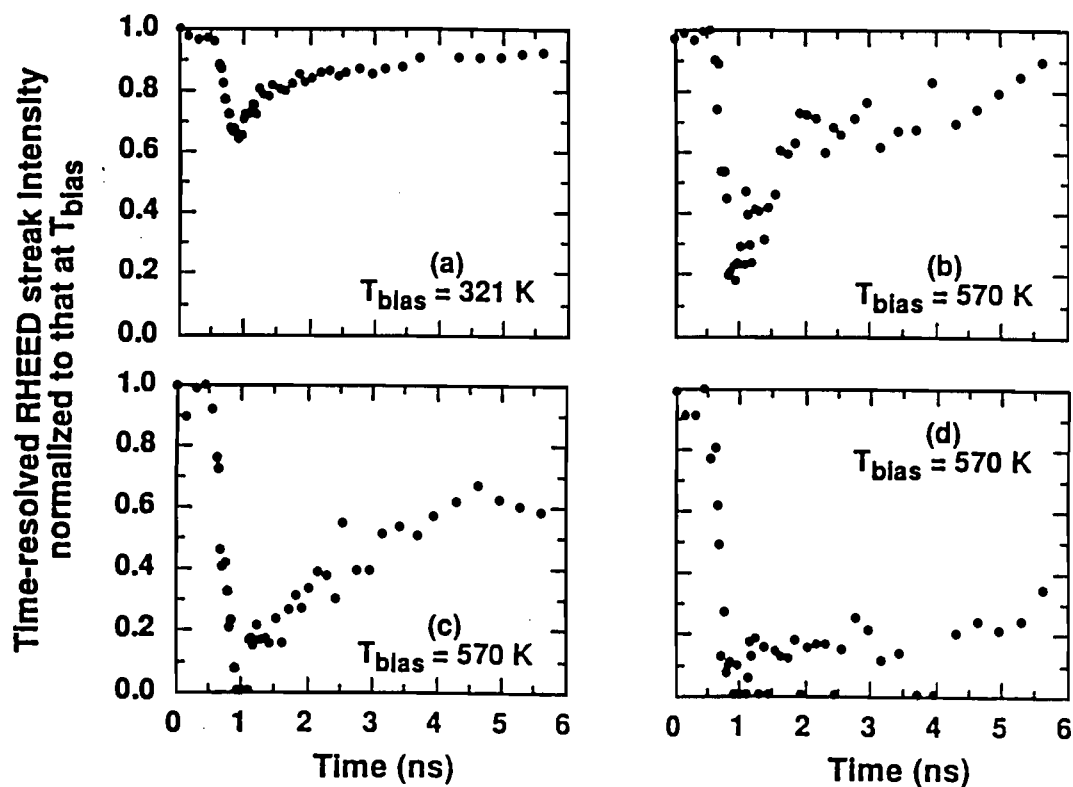


Figure 49. Time-resolved normalized RHEED streak intensity on Pb(100) at different bias temperatures, T_{bias} , subjected to varying peak laser intensities, I_p . (a) $T_{\text{bias}} = 321 \text{ K}$, $I_p = 4.4 \times 10^7 \text{ W/cm}^2$. (b) $T_{\text{bias}} = 570 \text{ K}$, $I_p = 2.3 \times 10^7 \text{ W/cm}^2$. (c) $T_{\text{bias}} = 570 \text{ K}$, $I_p = 3.4 \times 10^7 \text{ W/cm}^2$. (d) $T_{\text{bias}} = 570 \text{ K}$, $I_p = 5.1 \times 10^7 \text{ W/cm}^2$.

temperature range a second layering transition is not energetically favorable. Above the observed peak surface temperature, further disordering occurs and the residual order in the probed layer vanishes. Above this temperature, a second layering transition may take place increasing the disordered layer thickness to $4\pi/k_1 \sim 5.7 \text{ \AA}$, exceeding the 5 \AA probed by the electron beam.

REFERENCES

1. A. A. Chernov and L. V. Mikheev, *Phys. Rev. Lett.* **60**, 2488 (1988); *Physica A* **157**, 1042 (1989).
2. H. M. van Pinxteren and J. W. M. Frenken, *Surf. Sci.* **275**, 383 (1992).
3. H. -N. Yang, K. Fang, G. -C. Wang, and T. -M. Lu, *Phys. Rev. B* **44**, 1306 (1991).
4. J. W. Herman and H. E. Elsayed-Ali, *Phys. Rev. Lett.* **69**, 1228 (1992).

SUMMARY

From the time-resolved experiments on the low-index faces of Pb, it is evident that the dynamic surface structural behavior has a pronounced orientation dependence. The open Pb(110) surface was observed to disorder rapidly and reversibly with the 10^{11} K/s heating and cooling rates available from pulsed laser heating. It is likely that higher index planes, which were shown by medium-energy ion scattering experiments to exhibit pronounced surface melting in the case of Pb, would exhibit rapid disordering analogous to that observed on Pb(110). In contrast, the close-packed Pb(111) surface, which was shown not to experience surface melting, exhibited Debye-Waller behavior upon laser heating up to $\sim T_m + 120$ K. Greater superheating may be possible with larger heating rates. It is likely that any surface that does not exhibit surface melting could sustain significant transient superheating in analogy to Pb(111). The last surface studied was Pb(100), a surface which exhibits incomplete surface melting. Pb(100) showed residual order up to $\sim 615 \pm 20$ K, a result that differs from that obtained on Pb(111) in two respects. First, the diffraction intensity from Pb(100) deviated from Debye-Waller behavior at $T \sim 475$ K unlike Pb(111), which upon laser heating showed Debye-Waller behavior up to $T \sim 720$ K. It is likely that Pb(100) develops a high concentration of surface defects at temperatures above 500 K. Second, the temperature at which order is completely lost on Pb(100) is much lower than that observed on Pb(111). The disordered layer that forms on Pb(100) at elevated temperatures precludes substantial excursions above T_m . However, the time-resolved experiments show that residual order on Pb(100) is preserved for *small* excursions above T_m . This implies that there is an energetic barrier for the growth of the disordered layer thickness on Pb(100) at temperatures above T_m .

APPENDIX A: DETERMINATION OF THE SURFACE DEBYE TEMPERATURE USING RHEED

It has been clear for many years that the surface of a metal does not behave as a simple termination of the bulk. Qualitatively, this is due to the breaking of the three-dimensional symmetry of the crystal lattice. This asymmetry greatly affects the properties of surface atoms. For example, a surface atom of an fcc crystal has 7, 8, or 9 nearest-neighbors on the (110), (100), and (111) faces, respectively. This is compared with the 12 nearest-neighbors of an atom in the bulk of an fcc crystal. The decreased number of nearest-neighbor atoms on a metal surface influences the near-surface electronic density. This, in turn, influences the vibrational properties of the near-surface atoms. As a consequence, surface atoms experience an enhanced vibrational amplitude relative to atoms in the bulk of the crystal.

The observation of the enhanced vibrational amplitude of surface atoms has been accomplished using low-energy electron diffraction (LEED).¹ In these studies, the Debye-Waller attenuation of the intensity of the specular (00) beam was measured. These measurements yielded the Debye-Waller factor which can be related to the mean-square atomic vibrational amplitude, and hence the surface Debye temperature, Φ_D . This technique was first demonstrated in 1962 by MacRae and Germer, where they determined the surface Debye temperature of Ni(110).² Many of the LEED studies observed an increase in the measured Debye temperature of the surface with increasing primary electron beam energy. These observations are explained by the fact that the higher primary beam energies lead to a greater sampled depth which exhibits increasingly bulk-like characteristics.

RHEED represents another technique to measure surface Debye temperatures. RHEED has a sensitivity comparable to LEED and the probed depth of the electrons can be altered by simply varying the angle of incidence of the electron beam on the sample

surface, rather than changing the primary beam energy as in LEED. The surfaces considered were the low-index faces of Pb, which were prepared using the techniques outlined in Chapter 3. To determine Φ_D for the considered surfaces of Pb, the RHEED streak intensity was measured with a linear array camera as the sample temperature was varied. The experimental parameters for the three faces that were studied are given in Table 4.

The sensitivity of the diffraction intensity to temperature is a result of the Debye-Waller effect³ which predicts an exponential attenuation of the elastic diffraction intensity according to the following relation:

$$I(T) = I_0 \exp(-WT) \quad (\text{A.1})$$

Here, $I(T)$ is the elastic diffraction intensity at a temperature T and I_0 is the diffraction intensity from the crystal at $T = 0$ K. The term $-WT$ is known as the Debye-Waller factor and is given by

$$-WT = -|\Delta\bar{k}_n|^2 \langle u^2(T) \rangle \quad (\text{A.2})$$

The momentum transfer of the elastically diffracted electrons is dependent upon the corresponding order of the diffraction streak, n :

$$\Delta\bar{k}_n = \bar{k}'_n - \bar{k}_0 \quad (\text{A.3})$$

Here, \bar{k}'_n and \bar{k}_0 are the wavevectors corresponding to the n^{th} order RHEED streak and the undeflected electron beam, respectively. (A schematic diagram showing the geometry of the momentum transfer to a first-order RHEED streak is given in Fig. 50.)

Table 4. Parameters for the RHEED surface Debye temperature measurements

Face	E (keV)	θ (°)	d (Å)	Ref.
(110)	18.2	2.8	4.6	4
(111)	18.2	2.4	3.9	5
(100)	15.0	3.2	4.8	6

E = energy of the incident electrons

θ = angle of incidence of the electron beam on the sample

d = depth probed by the electron beam

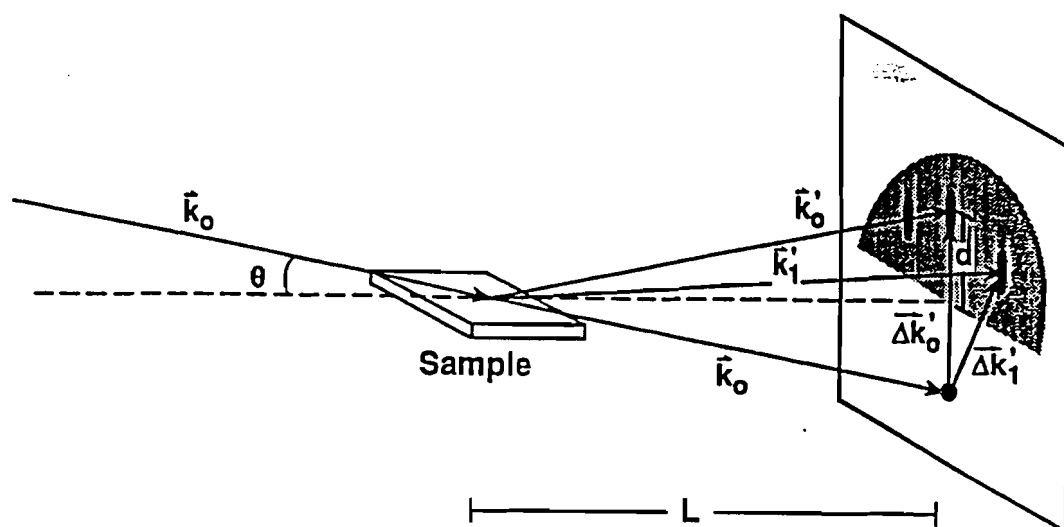


Figure 50. Scattering geometry in the RHEED intensity measurements. The wavevector \bar{k}_0 corresponds to the incident electron beam, while \bar{k}'_0 and \bar{k}'_1 correspond to the specular and first-order peaks, respectively. $\Delta\bar{k}'_0$ and $\Delta\bar{k}'_1$ represent the momentum transfers to the specular and first-order diffraction peaks, respectively. (Courtesy of E. A. Murphy)

$\langle u^2(T) \rangle$ corresponds to the mean-square displacement of an atom from equilibrium. In this treatment, the mean-square displacement is taken to be isotropic. The term W can be expressed as

$$W = \frac{|\Delta \bar{k}_s|^2}{|\Delta \bar{k}_0|^2} \left(\frac{4\pi \sin \theta}{\lambda} \right)^2 \left(\frac{3\hbar^2}{mk_B \Phi_D^2} \right) \quad (\text{A.4})$$

In this expression, θ is the angle of incidence of the electron beam, λ is the electron de Broglie wavelength, \hbar is Planck's constant, m is the ionic mass, k_B is Boltzmann's constant, and Φ_D is the effective Debye temperature. The momentum-transfer ratio is determined from a photograph of the RHEED pattern as shown in Fig. 50.

An example of a RHEED streak intensity measurement is given in Fig. 51 where the Pb(111) surface was examined.⁵ The data are plotted on a semilogarithmic scale and show an exponential, Debye-Waller decrease of the normalized streak intensity with temperature in the entire studied temperature range extending up to $T_m - 15$ K. This observation is consistent with other experiments that show Pb(111) to be a nonmelting face. For comparison, the Debye-Waller reduction in diffraction intensity assuming a bulk Debye temperature of 88 K is plotted on the same graph. The larger slope of the RHEED data as compared with the slope predicted assuming a bulk Debye temperature implies that the surface atoms experience an increased vibrational amplitude relative to the bulk atoms. The (110) and (100) surfaces displayed Debye-Waller behavior up to 520 K and 475 K, respectively.^{4,6} At higher temperatures, deviation from Debye-Waller behavior occurred indicating the beginnings of surface disorder through pronounced anharmonic surface vibrations.

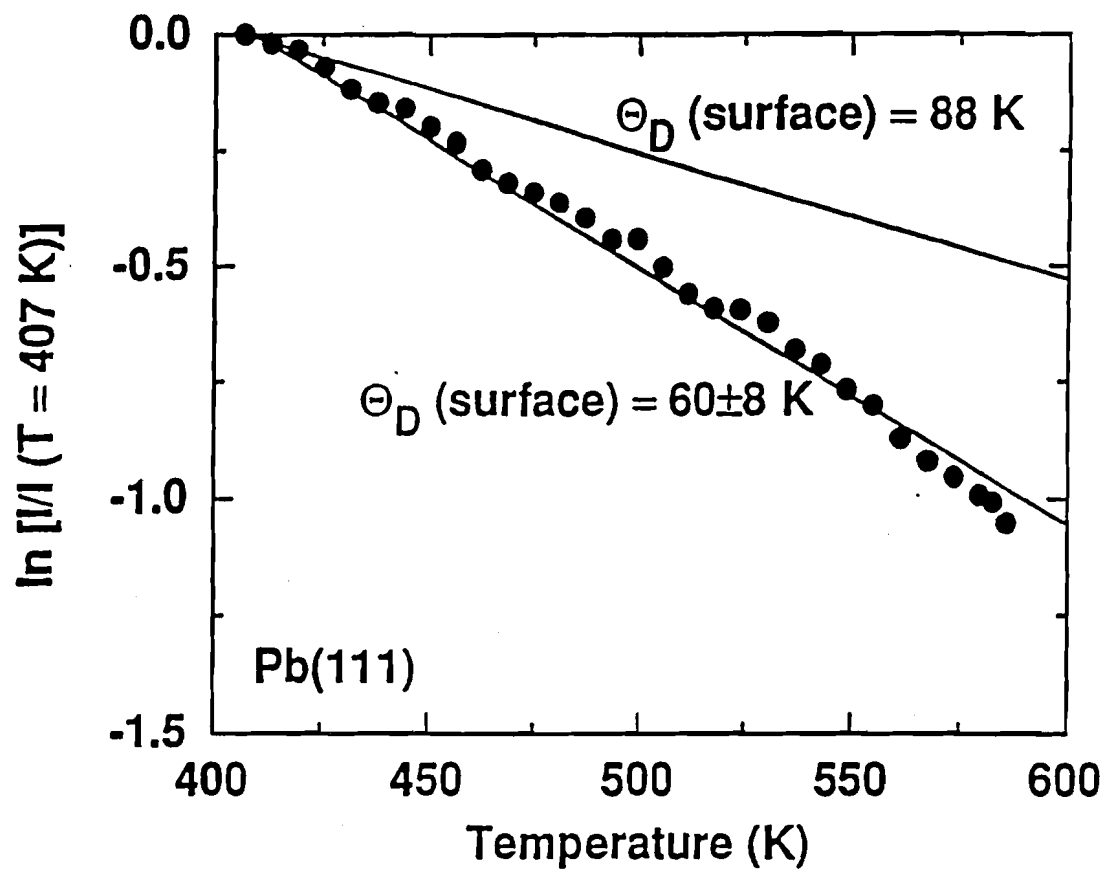


Figure 51. Logarithm of the normalized intensity of the (10) streak of Pb(111). The diffraction intensity decays according to the Debye-Waller effect. Also displayed in the plot is the predicted behavior of the streak intensity, assuming that the surface has a Debye temperature identical to that of the bulk.

Analysis of the exponential region of the data yielded the effective surface Debye temperatures for these faces. From Eq. A.1, the slope of the $\ln[I(T)/I_0]$ graph corresponds to the term W above. Thus the slope of the $\ln[I(T)/I_0]$ graph can be related to the surface Debye temperature. The effective surface Debye temperature is obtained by isolating Φ_D from Eq. A.2:

$$\Phi_D = \frac{|\Delta\bar{k}_n|}{|\Delta\bar{k}_0|} \left(\frac{4\pi \sin\theta}{\lambda} \right) \sqrt{\frac{3\hbar^2}{mk_B W}}. \quad (\text{A.5})$$

Values of Φ_D for the three low-index faces of Pb are given in Table 5 along with values obtained from LEED. The errors in the RHEED measurements are due to the spread in the slopes of the semilogarithmic plots and the uncertainty in the angle of incidence and momentum transfers as measured from photographs of the RHEED pattern. These experiments have demonstrated that RHEED is a viable method to determine the Debye temperature of surfaces yielding results that are compatible with previous LEED measurements.

Table 5. The Debye temperature for the low-index faces of Pb

Technique	Pb(110)	Pb(111)	Pb(100)	Ref.
LEED	37±10 K	55±10 K 49±10 K	-----	7,8
RHEED	30±5 K	60±8 K	64±8 K	present work

REFERENCES

1. See D. P. Jackson, *Surf. Sci.* **43**, 431 (1974) and references therein.
2. A. U. MacRae and L. H. Germer, *Phy. Rev. Lett.* **8**, 489 (1962).
3. P. Debye, *Ann. Phys.* **43**, 49 (1913); I. Waller, *Z. Phys.* **17**, 398 (1923); *Ann. Phys.* **79**, 261 (1926).
4. J. W. Herman and H. E. Elsayed-Ali, *Phys. Rev. Lett.* **68**, 2952 (1992).
5. J. W. Herman and H. E. Elsayed-Ali, *Phys. Rev. Lett.* **69**, 1228 (1992).
6. J. W. Herman, H. E. Elsayed-Ali, and E. A. Murphy, *Phys. Rev. Lett.* **71**, 400 (1993).
7. R. M. Goodman, H. H. Farrell and G. A. Somorjai, *J. Chem. Phys.* **48**, 1046 (1968).
8. R. M. Goodman and G. A. Somorjai, *J. Chem. Phys.* **52**, 6325 (1970).

APPENDIX B: AUGER ELECTRON SPECTROSCOPY (AES)

When an x-ray or energetic electron or ion strikes a solid, a back-scattered spectrum of electrons results. For the purpose of this discussion it is assumed that an electron beam constitutes the mode of excitation. The resulting secondary electron spectrum yields a great deal of information about the composition of the surface of the solid. An example of a secondary electron spectrum is given in Fig. 52. The spectrum $N(E)$ consists of four primary components:^{1,2}

- (i) "True" secondary electrons: These secondary electrons result from a cascade process initiated by collisions of the primary exciting electrons within the solid. The number of secondary electrons is limited only by the influence of the work function of the material which an electron must overcome to escape from the surface.
- (ii) Elastically scattered electrons: Electrons scattered with no loss of energy.
- (iii) Loss peaks: These peaks, typically located several tens of electron volts below the elastic peak, are associated with primary electrons that have lost discrete amounts of energy through electron or plasmon scattering. The position of these peaks varies directly with the position of the elastic peak.
- (iv) Auger peaks: These peaks are associated with the Auger emission process and are characteristic of the chemical composition of the surface. The energies of the Auger peaks are independent of the primary exciting beam energy, in contrast to the loss peaks.

The process of Auger emission is shown schematically in Fig. 53.^{2,3} An incident energetic electron ionizes a core energy level W . The corresponding hole is filled with an electron from a shallow energy level. The amount of energy released, given by $E_W - E_X$, can result in the production of an x-ray or an Auger electron. The

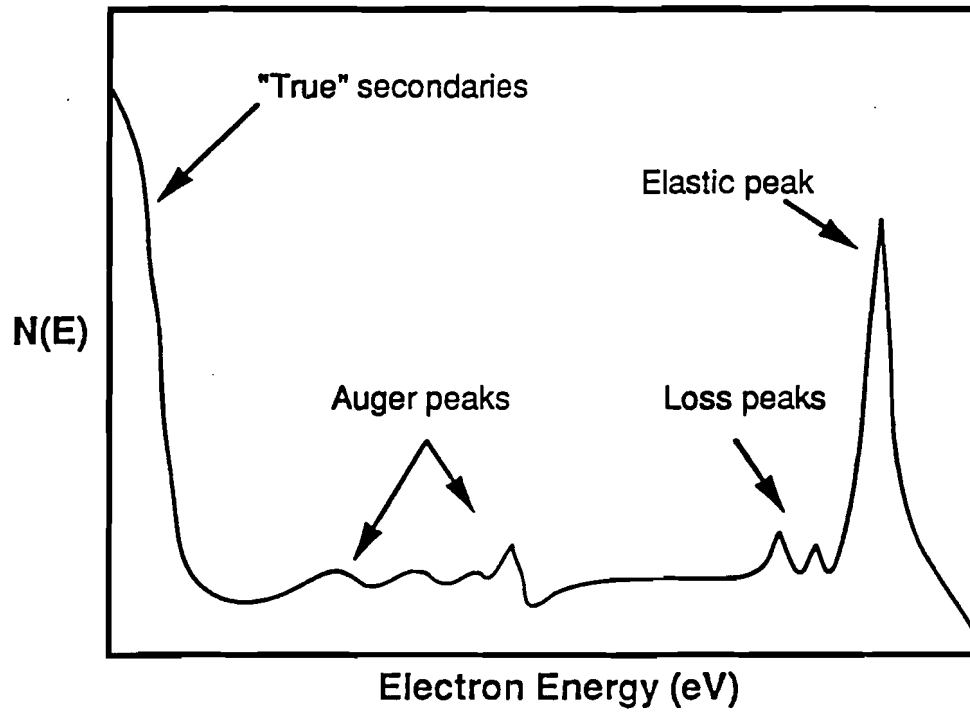


Figure 52. Secondary electron spectrum.

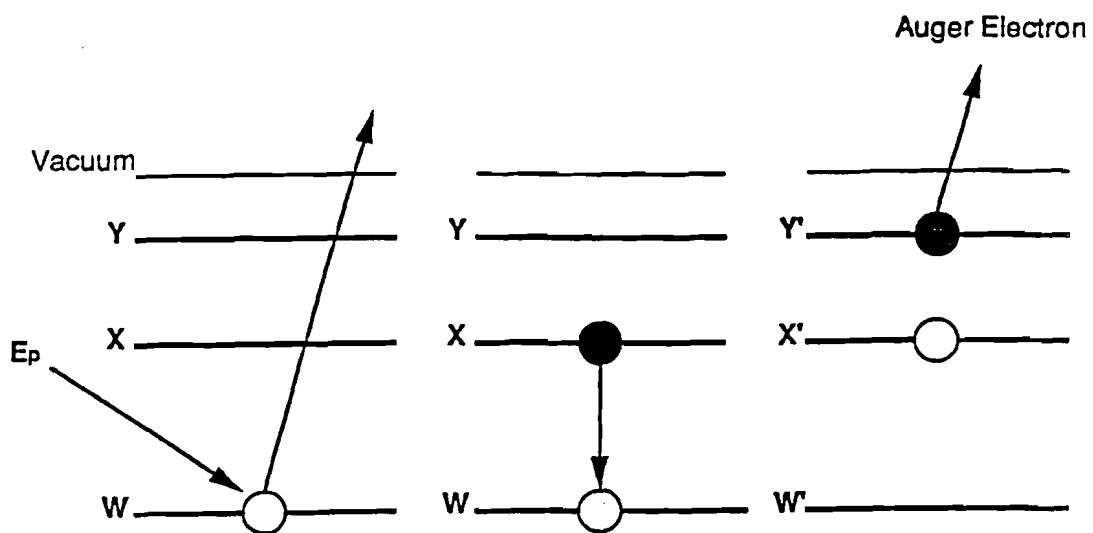
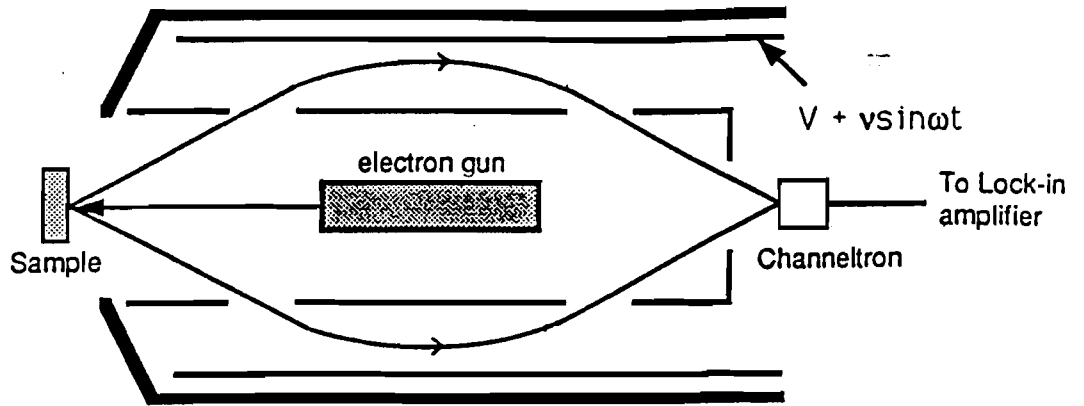


Figure 53. The Auger effect.

emission of an Auger electron is much more probable than an x-ray when the core level energy is < 10 keV. The emitted Auger electrons are characteristic of the core level that was ionized and therefore yield information about the local chemical environment. If an Auger electron has sufficient energy it will escape from the surface. The escape depth of the Auger electron is limited by the work function of the surface and the energy-dependent electron mean-free path. Auger electrons have energies in the 10-1000 eV range, corresponding to escape depths of < 30 Å, making AES a surface sensitive chemical probe.

The peaks in the secondary electron spectrum that correspond to Auger electrons tend to be difficult to discern over the noise of the other secondary electrons. Indeed, the electron current due to Auger processes is typically a factor of 10^5 smaller than the primary exciting current. It was shown that the Auger peaks could be clearly observed if the derivative of the secondary electron spectrum was obtained.⁴ A number of devices have been developed to accomplish this including the retarding field analyzer (RFA) and the cylindrical mirror analyzer (CMA).²

Our system utilizes a CMA for the high efficiency detection of Auger spectra. A cross-sectional view of the CMA is shown in Fig. 54. The CMA consists of two concentric cylinders and a coaxial electron gun which provides an electron beam of approximately 50 μ A and 3-5 keV energy. The beam strikes the sample creating secondary electrons which enter the interior of the grounded inner cylinder and pass through a grid into the region between the cylinders. The outer cylinder has a negative potential applied to it which serves to deflect the secondary electrons in a given band of energy through a second grid to a channeltron electron detector. In this mode of operation, the spectrum $N(E)$ is obtained. To observe the subtle Auger peaks, the derivative of the electron spectrum with respect to energy, $N'(E)$, is obtained. Since the secondary electron current I_s is proportional to $N(E)$, I_s' corresponds to $N'(E)$. To



CYLINDRICAL MIRROR ANALYZER

Figure 54. Cross-sectional view of the cylindrical mirror analyzer.

obtain I_s' , a small sinusoidally modulated voltage is applied to the outer cylinder so that the resulting voltage is given by

$$V(t) = V + v \sin \omega t \quad (\text{B.1})$$

The detected current is a function of $V(t)$ and can be expanded in a Taylor's series:

$$\begin{aligned} I(V + v \sin \omega t) = & I(V) + I'(V)v \sin \omega t + \frac{1}{2} I''(V)v^2 \sin^2 \omega t + \dots \\ & + \frac{1}{n!} I^{(n)}(V)v^n \sin^n \omega t \end{aligned} \quad (\text{B.2})$$

$I'(V)$, and hence $N'(E)$, is proportional to $\sin \omega t$. Detection of $N'(E)$ therefore consists of observing the in-phase component of the channeltron output with a lock-in amplifier, which provides the voltage modulation to the outer cylinder. The complete set-up of the CMA system is shown in Fig. 55.

A typical Auger spectrum is shown in Fig. 56. This spectrum was taken with a primary energy of 3 keV and corresponds to a contaminated Pb surface. Carbon and oxygen peaks are clearly seen and identified by comparing the corresponding energies to standard Auger spectra of the pure elements.⁵ Peak shifts of several eV from the values of the standard are common and reflect slightly differing surface chemical environments. For example, surface contamination, which alters the work function, can account for slight energy shifts in Auger peaks.

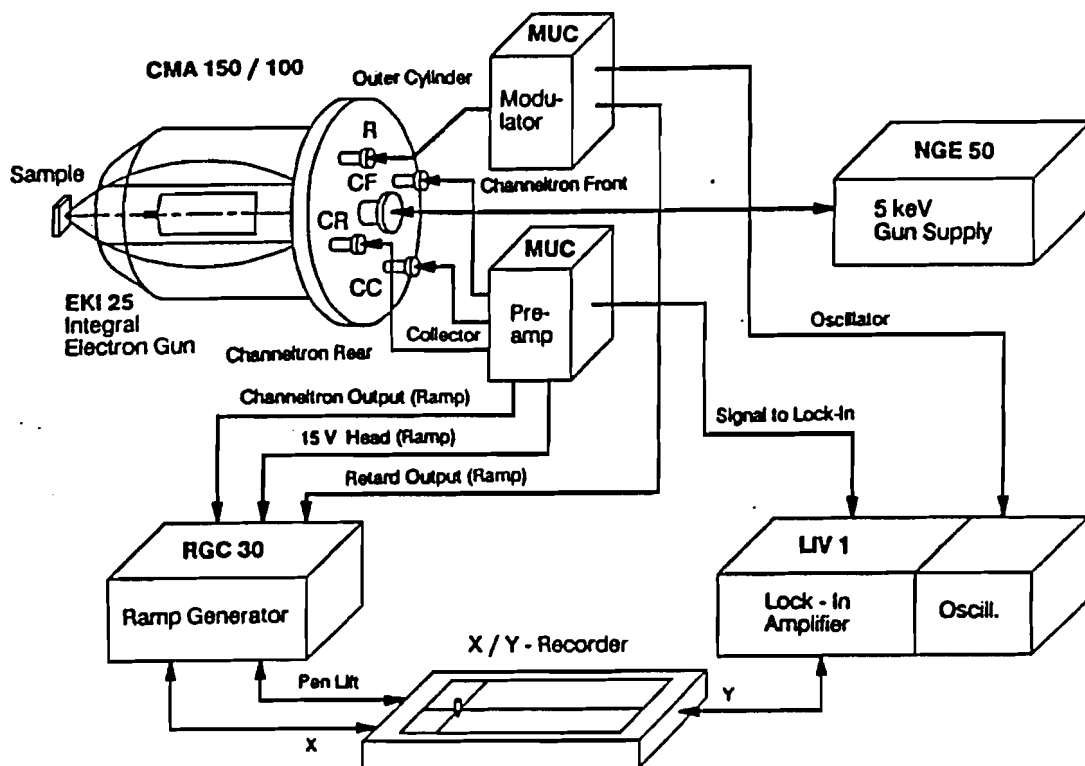


Figure 55. Experimental configuration of the cylindrical mirror analyzer system.
 (From Omicron Vakuumphysik, Instruction manual for the CMA150.)

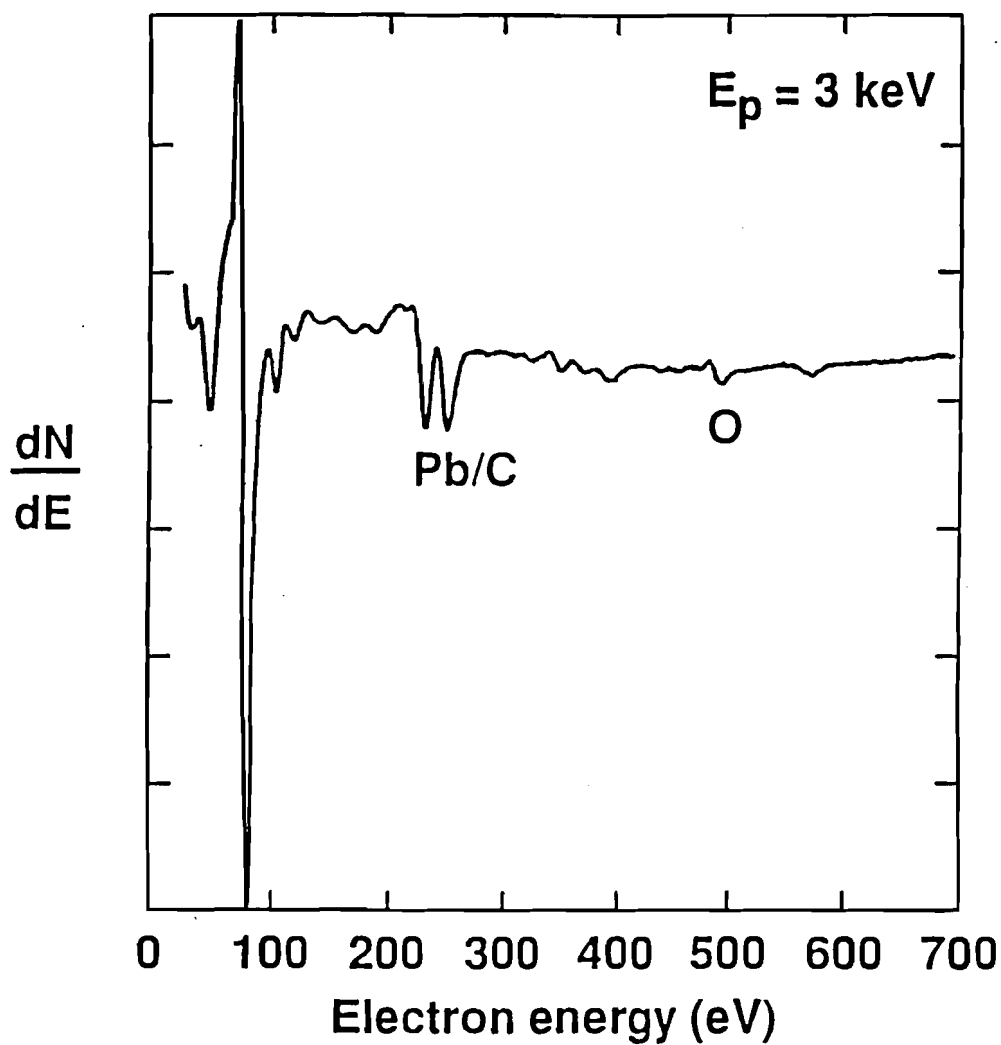


Figure 56. Auger spectrum of a contaminated Pb surface taken with a primary beam energy of 3 keV. Carbon and oxygen Auger peaks are clearly visible.

REFERENCES

1. C. B. Duke and R. L. Park, *Physics Today* **25**, 23 (1972).
2. C. C. Chang, *Surf. Sci.* **25**, 53 (1971).
3. J. C. Riviere, *Contemp. Phys.* **14**, 513 (1973).
4. L. A. Harris, *J. Appl. Phys.* **39**, 1419 (1968).
5. L. E. Davis *et al.*, *Handbook of Auger Electron Spectroscopy*, Second Edition
(Physical Electronics Industries, Eden Prairie, MN, 1976).

APPENDIX C: REGENERATIVE AMPLIFIER LASER SYSTEM

The laser system used in the picosecond RHEED experiments is a continuously-pumped Nd:YAG regenerative amplifier that is seeded by a Nd:YAG oscillator. A diagram of the system is shown in Fig. 57. The oscillator is mode-locked with an acousto-optic modulator and provides a 100 MHz train of pulses with temporal width in the 150-300 ps range and a pulse energy of ~ 15 nJ. A Pockels cell selects a pulse from the oscillator pulse train for injection in the regenerative amplifier cavity. The selected pulse strikes a glass wedge and is partially reflected into the amplifier cavity through a polarizer. The glass wedge prevents the regenerative amplifier output from propagating back to the oscillator, which would adversely affect the mode-locking. For injection into the amplifier cavity, a fast high-voltage step is applied to the lithium niobate intercavity Pockels cell, achieving quarter-wave rotation. In conjunction with the intercavity quarter-wave plate, the quarter-wave rotation of the Pockels cell results in no net polarization rotation, corresponding to minimal cavity loss. This results in the injected pulse being confined to the amplifier cavity. The energy of the injected pulse increases with each pass through the gain medium. After ~ 40 round trips in the cavity, the pulse energy increases to the maximum value and the pulse is ejected from the cavity by the application of a second high-voltage step to the intercavity Pockels cell. The second high-voltage step results in half-wave rotation. The corresponding net polarization rotation results in the pulse being reflected out of the cavity by the intercavity polarizer. The pulse build-up and the cavity dump are illustrated in Fig. 58, where the leakage through a cavity mirror was observed using a photodiode. The amplified pulse has a typical energy of ~ 0.3 mJ. The ratio of the energy of the principle pulse to secondary pulses is limited by the quality of the intercavity polarizer and is at best 300:1. This ratio can be less favorable due to the acousto-optical

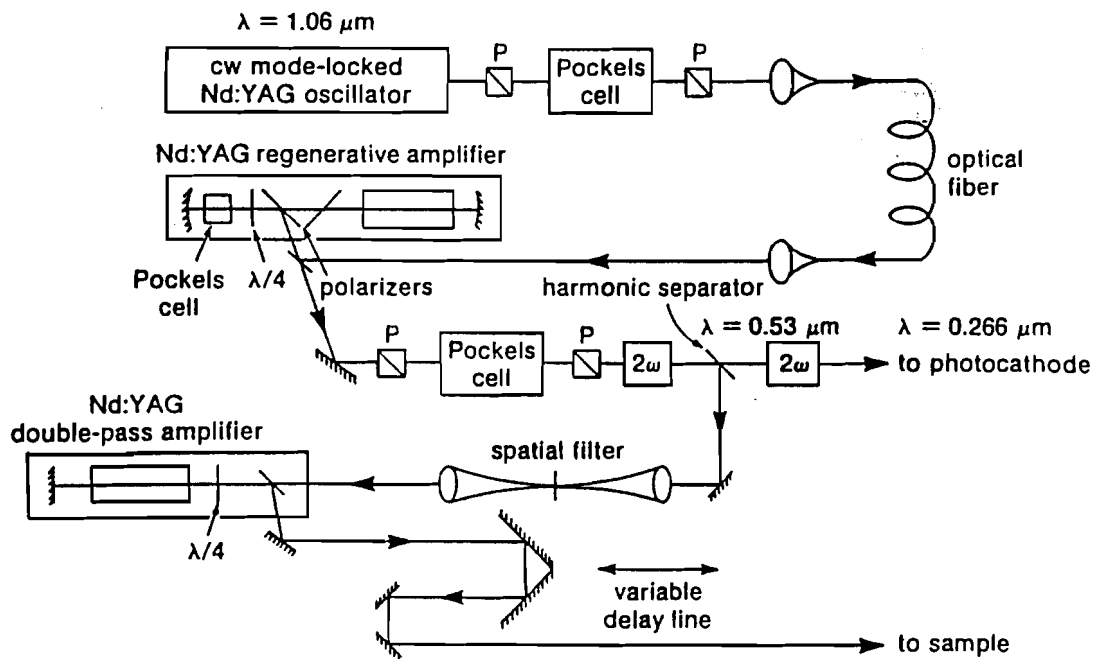
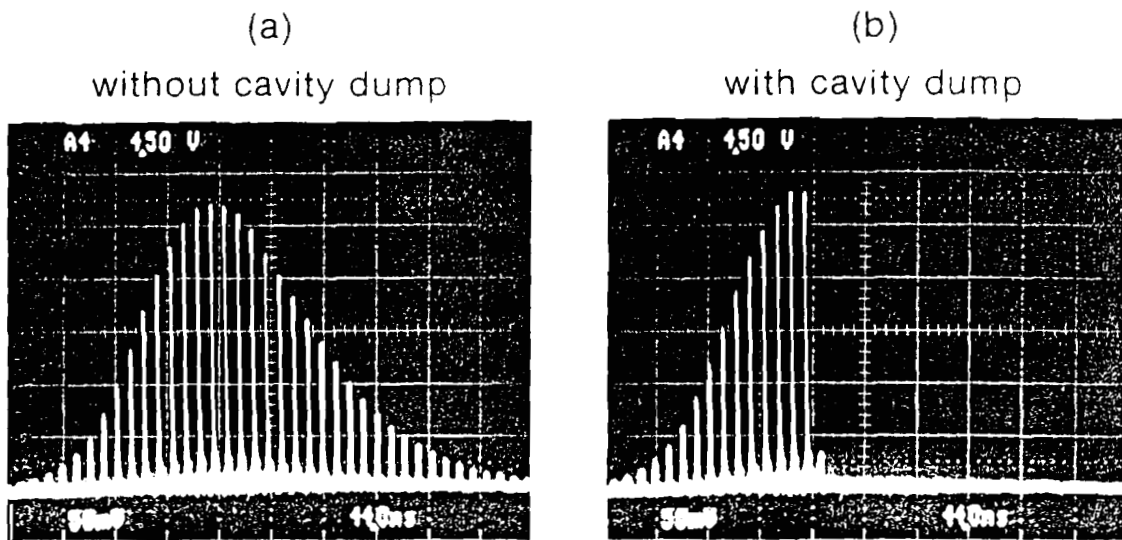


Figure 57. Schematic diagram of the regenerative amplifier laser system.



Z697

Figure 58. Build-up of the energy of the injected pulse in the regenerative amplifier cavity. The pulse is ejected from the cavity when the peak energy is reached.

properties of the intercavity Pockels cell. In order to obtain a clean output pulse, the pulse from the amplifier cavity is passed through an external Pockels cell which acts as a temporal window, blocking pre- and post-pulses. The regenerative amplifier system can be operated at repetition rates up to 1.5 kHz with a pulse-to-pulse stability of ~ 10%. In the time-resolved RHEED system, the majority of the final pulse is amplified and used for sample heating while the remainder is frequency-quadrupled for photoelectric production of electrons in the photoactivated electron gun.

Further amplification of the laser pulse is achieved in a double-pass Nd:YAG amplifier. Initial work utilized an 8 Hz amplifier. The system was subsequently upgraded to include a 15 Hz amplifier. The latter amplifier has a double-pass gain of up to 100, leading to amplified pulse energies of 20 mJ, sufficient for the time-resolved experiments where uniform heating of samples of area ~ 1 cm² was necessary.